COPERNICUS SPACE COMPONENT SENTINEL OPTICAL IMAGING

MISSION PERFORMANCE CLUSTER SERVICE

Data Quality Report

Sentinel-3 OLCI

January 2022

Ref.: OMPC.ACR.DQR.03.01-2022
Issue: 1.0
Date: 09/02/2022
Contract: 4000136252/21/I-BG

Customer: ESA		**Document Ref.:**	OMPC.ACR.DQR.03.01-2022
Contract No.: 4000136252/21/I-BG		**Date:**	09/02/2022
		Issue:	1.0

Project:	COPERNICUS SPACE COMPONENT SENTINEL OPTICAL IMAGING MISSION PERFORMANCE CLUSTER SERVICE		
Title:	Data Quality Report - OLCI		
Author(s):	OLCI ESL team		
Approved by:	L. Bourg, OPT-MPC OLCI ESL Coordinator	**Authorized by**	C. Hénocq, OPT-MPC S3 Technical Manager
Distribution:	ESA, EUMETSAT, published in Sentinel Online		
Accepted by ESA	S. Dransfeld, ESA TO		
Filename	OMPC.ACR.DQR.03.01-2022 - i1r0 - OLCI DQR January 2022.docx		

Changes Log

Version	Date	Changes
1.0	09/02/2021	First version

List of Changes

Version	Section	Answers to RID	Changes

Table of content

List of Figures

List of Tables

1 Processing Baseline Version

1.1 Sentinel3-A

IPF	IPF / Processing Baseline version	Date of deployment
OL1	06.12 / 3.01 (OL__L1_.002.21.00)	NRT: 18/11/2021 11:34 UTC NTC: 28/04/2021 07:15 UTC
OL2 LAND	06.14 / 2.66	NRT: 23/06/2020 08:00 UTC NTC: 23/06/2020 08:00 UTC
OL2 MAR	07.00 / 2.72M	NRT: 16/02/2021 08:35 UTC NTC: 15/02/2021 05:46 UTC
SY2	06.21 / 2.77	NTC: 14/06/2021 08:21 UTC
SY2_VGS	06.09 / 2.77	NTC: 14/06/2021 08:21 UTC

1.2 Sentinel3-B

IPF	IPF / Processing Baseline version	Date of deployment
OL1	06.12 / 3.01 (OL__L1_.002.21.00)	NRT: 29/07/2021 08:30 UTC NTC: 29/07/2021 08:30 UTC
OL2 LAND	06.14 / 1.40	NRT: 23/06/2020 08:00 UTC NTC: 23/06/2020 08:00 UTC
OL2 MAR	07.00 / 2.72M	NRT: 16/02/2021 07:56 UTC NTC: 15/02/2021 06:47 UTC
SY2	06.21 / 1.55	NTC: 14/06/2021 08:21 UTC
SY2_VGS	06.09 / 1.55	NTC: 14/06/2021 08:21 UTC

2 Instrument monitoring

2.1 CCD temperatures

2.1.1 OLCI-A

The monitoring of the CCD temperatures is based on MPMF data extractions not yet operational. In the meantime, we monitor the CCD temperatures on the long-term using Radiometric Calibration Annotations (see Figure 1). Variations are very small (0.09 C peak-to-peak) and no trend can be identified. Data from current cycle (rightmost data points) do not show any specificity.

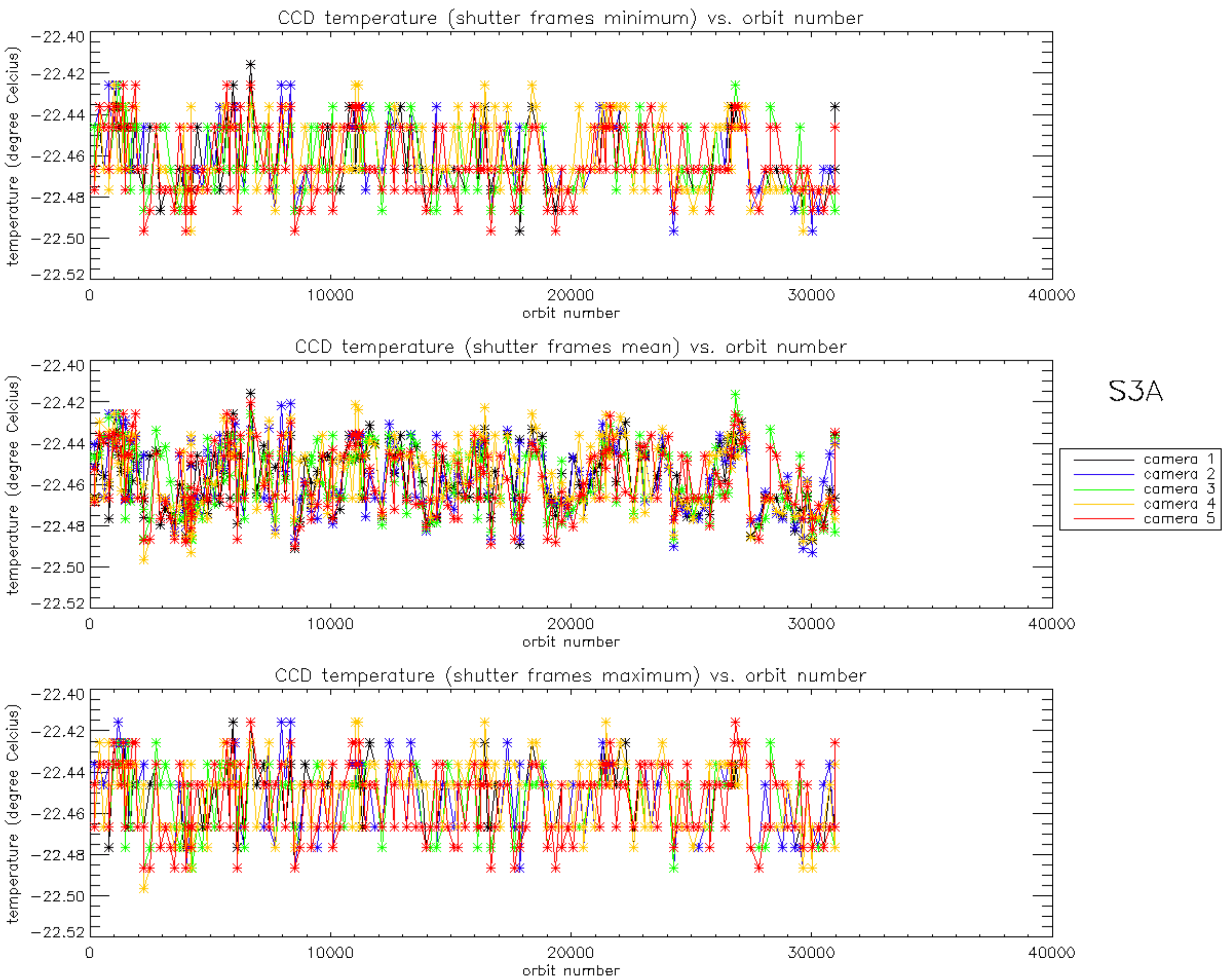

Figure 1: long term monitoring of OLCI-A CCD temperatures using minimum value (top), time averaged values (middle), and maximum value (bottom) provided in the annotations of the Radiometric Calibration Level 1 products, for the shutter frames, all radiometric calibrations so far except the first one (absolute orbit 183) for which the instrument was not yet thermally stable.

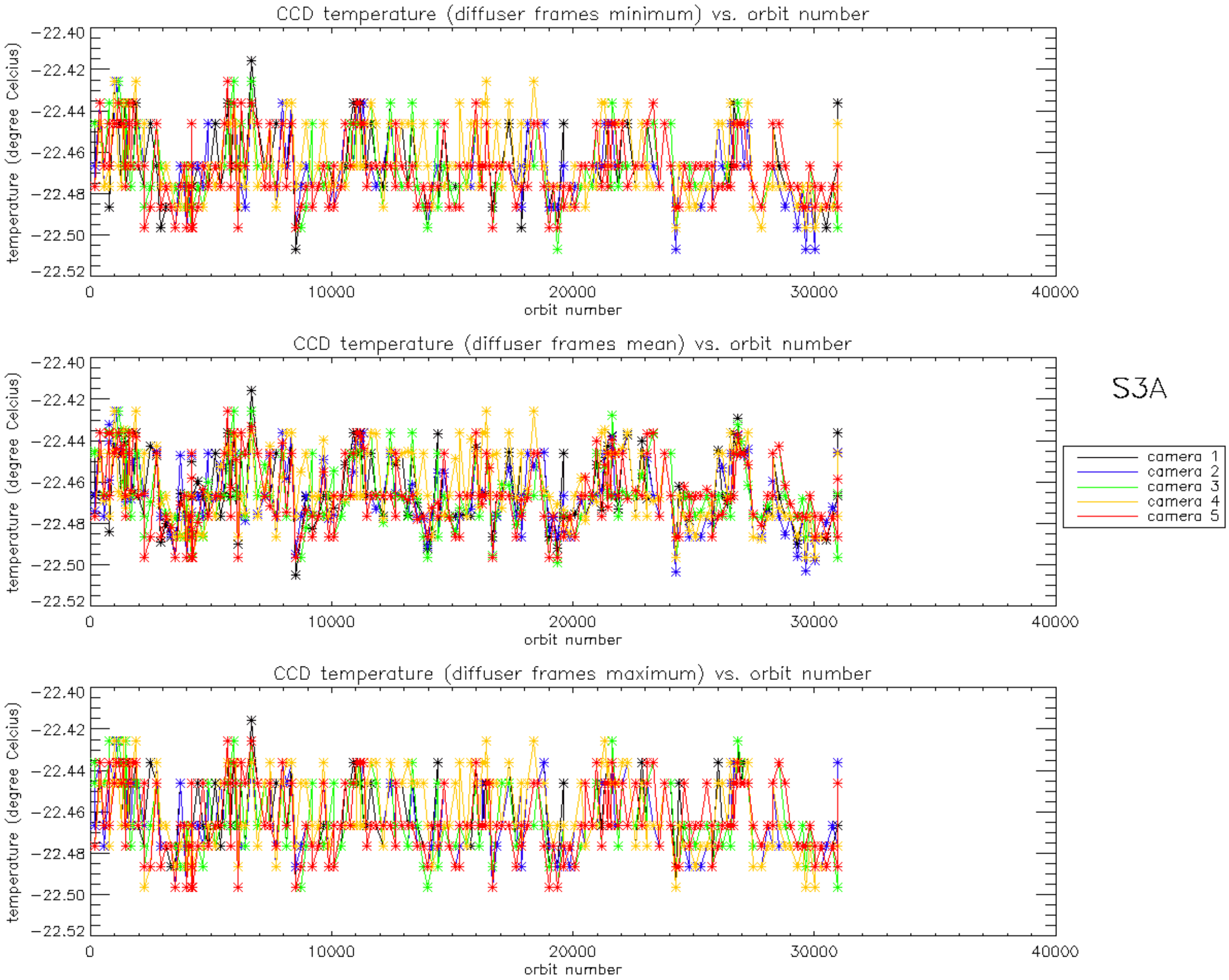

Figure 2: Same as Figure 1 for diffuser frames.

2.1.2 OLCI-B

As for OLCI-A, the variations of CCD temperature are very small (0.08 C peak-to-peak) and no trend can be identified. Data from current cycle (rightmost data points) do not show any specificity.

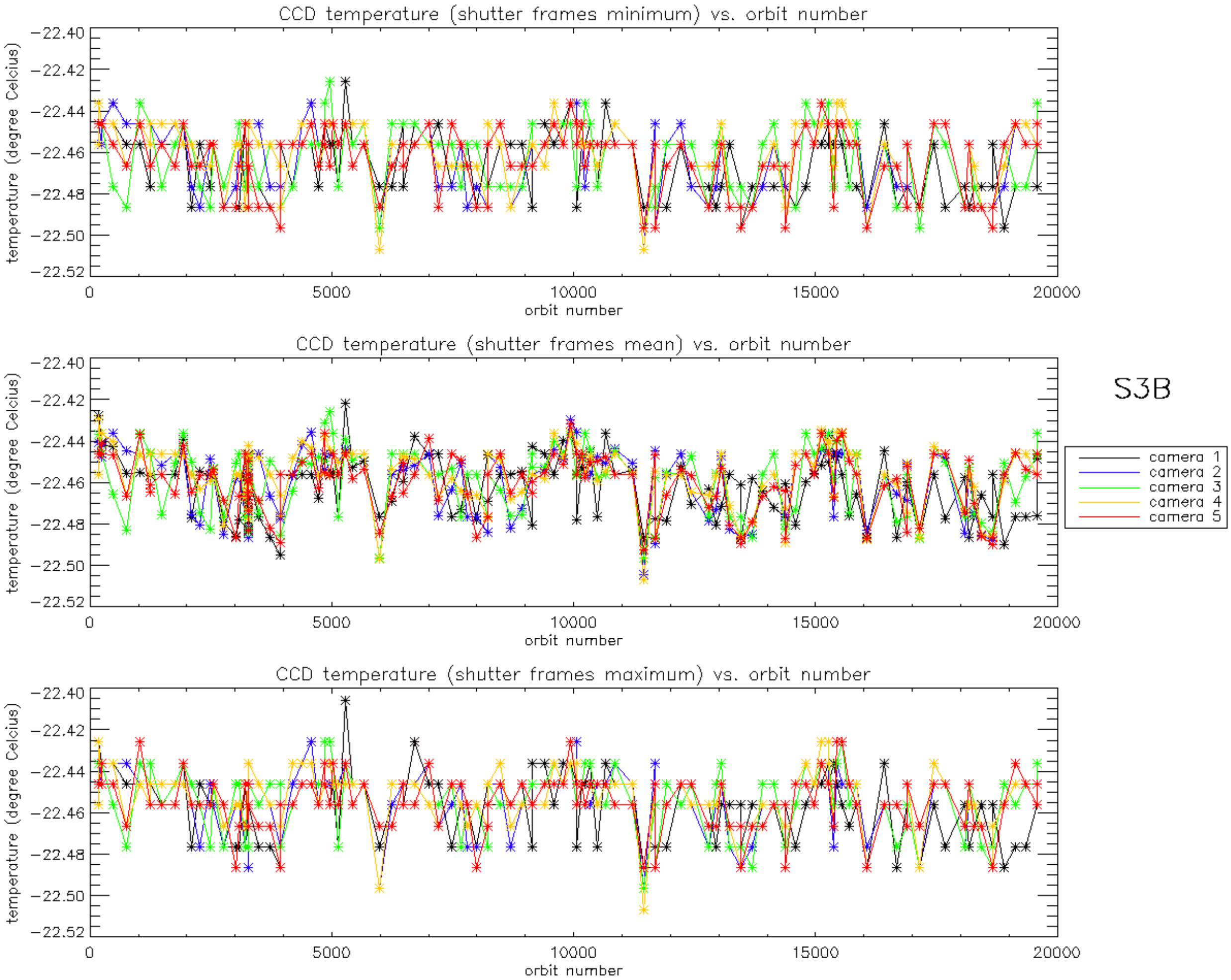

Figure 3: long term monitoring of OLCI-B CCD temperatures using minimum value (top), time averaged values (middle), and maximum value (bottom) provided in the annotations of the Radiometric Calibration Level 1 products, for the Shutter frames, all radiometric calibrations so far except the first one (absolute orbit 167) for which the instrument was not yet thermally stable.

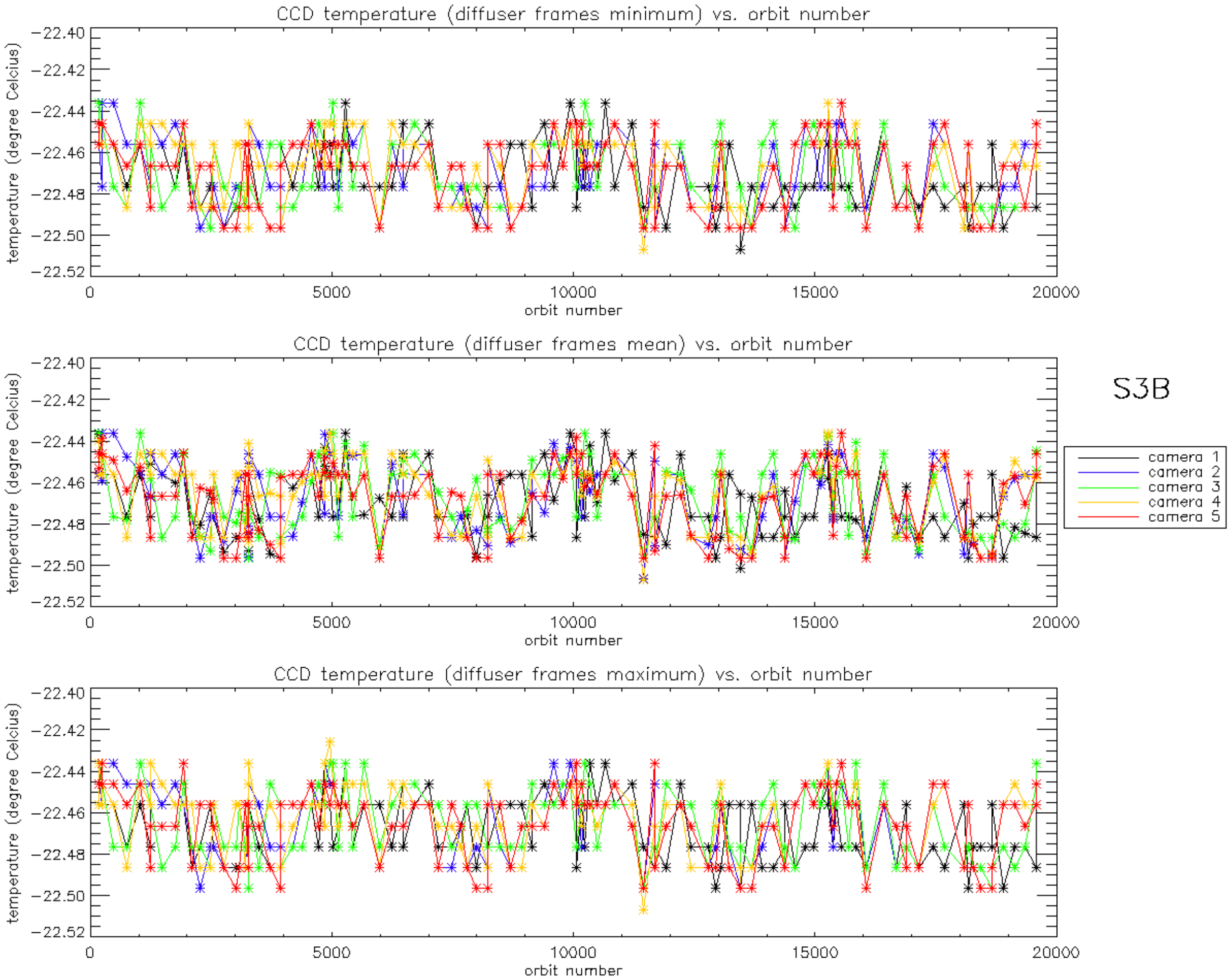

Figure 4: same as Figure 3 for diffuser frames.

2.2 Radiometric Calibration

For OLCI-A, three Radiometric Calibration sequences have been acquired during the reported period:

- S01 sequence (diffuser 1) on 11/01/2022 12:22 to 12:24 (absolute orbit 30739)
- S01 sequence (diffuser 1) on 27/01/2022 00:19 to 00:21 (absolute orbit 30960)
- S05 sequence (diffuser 2) on 27/01/2022 02:00 to 02:02 (absolute orbit 30961)

For OLCI-B, three Radiometric Calibration sequences have been acquired during the reported period:

- S01 sequence (diffuser 1) on 12/01/2022 07:54 to 07:56 (absolute orbit 18908)
- S01 sequence (diffuser 1) on 28/01/2022 11:00 to 11:08 (absolute orbit 19587)
- S05 sequence (diffuser 2) on 28/01/2022 12:41 to 12:43 (absolute orbit 19588)

As there was no Cyclic Performance Report delivered since Cyclic Performance Report #78/#59 (OLCI-A/OLCI-B), we report hereafter the Radiometric calibration sequences that have been acquired between the release of the last CPR and the beginning of the current reporting period. These acquisitions are taken into account in the current Data Quality report:

For OLCI-A, four Radiometric Calibration sequences have been acquired since the last CPR:

- S01 sequence (diffuser 1) on 23/11/2021 06:48 to 06:50 (absolute orbit 30037)
- S05 sequence (diffuser 2) on 23/11/2021 08:29 to 08:31 (absolute orbit 30038)
- S01 sequence (diffuser 1) on 11/12/2021 00:39 to 00:41 (absolute orbit 30290)
- S01 sequence (diffuser 1) on 26/12/2021 04:12 to 04:14 (absolute orbit 30056)

For OLCI-B, two Radiometric Calibration sequences have been acquired since the last CPR:

- S01 sequence (diffuser 1) on 11/12/2021 20:11 to 20:13 (absolute orbit 18908)
- S01 sequence (diffuser 1) on 26/12/2021 22:04 to 22:06 (absolute orbit 19123)

The acquired Sun azimuth angles are presented on Figure 5 for OLCI-A and Figure 6 for OLCI-B, on top of the nominal values without Yaw Manoeuvre (i.e. with nominal Yaw Steering control of the satellite).

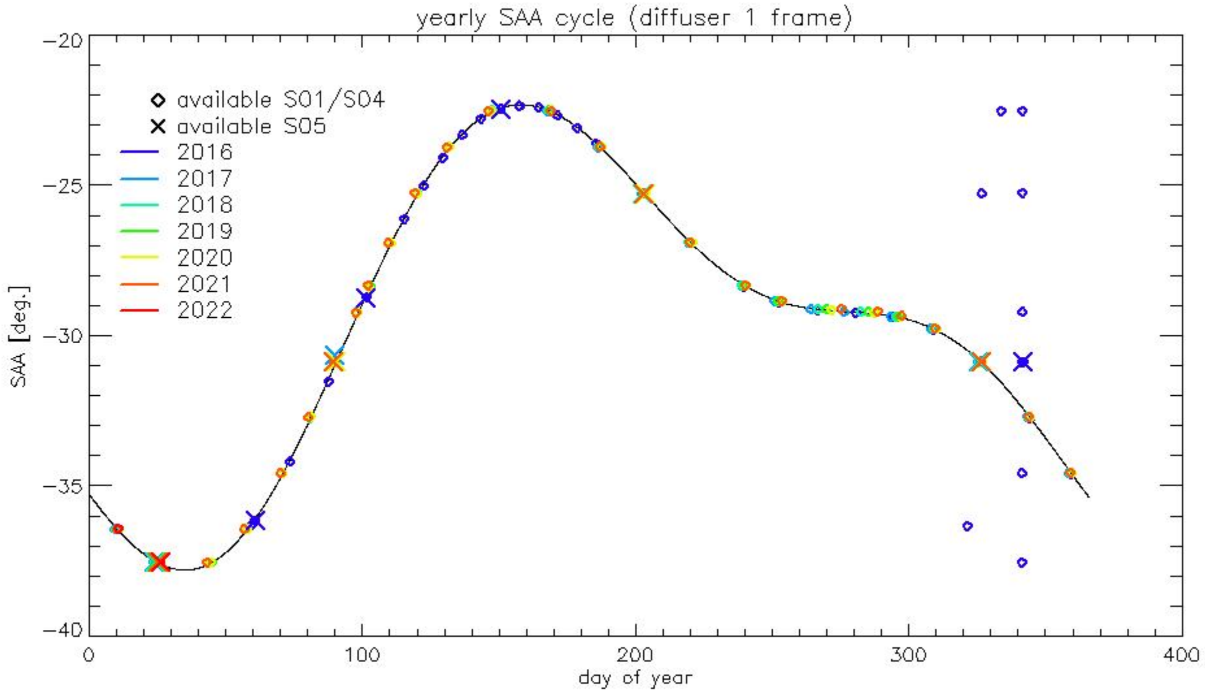

Figure 5: Sun azimuth angles during acquired OLCI-A Radiometric Calibrations (diffuser frame) on top of nominal yearly cycle (black curve). Diffuser 1 with diamonds, diffuser 2 with crosses. Different colours correspond to different years of acquisition (see the legend inside the figure).

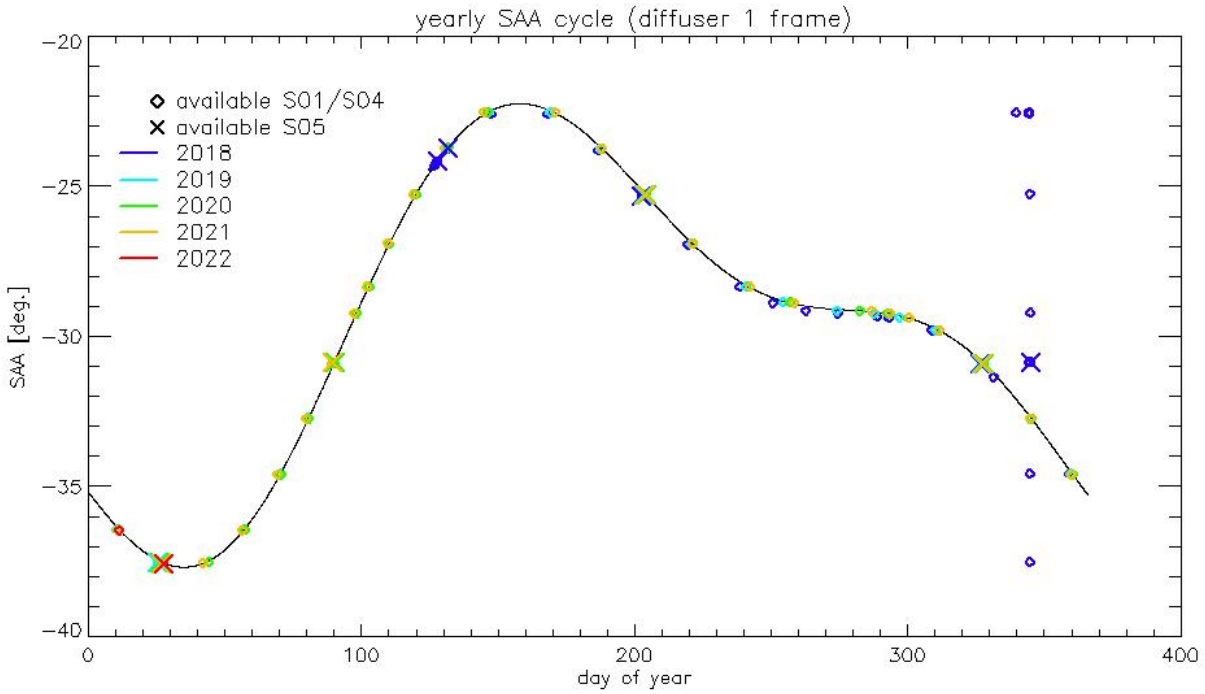

Figure 6: same as Figure 5 for OLCI-B.

Sun Zenith Angles as a function of Sun Azimuth Angles are presented in Figure 7 for OLCI-A and Figure 8 for OLCI-B.

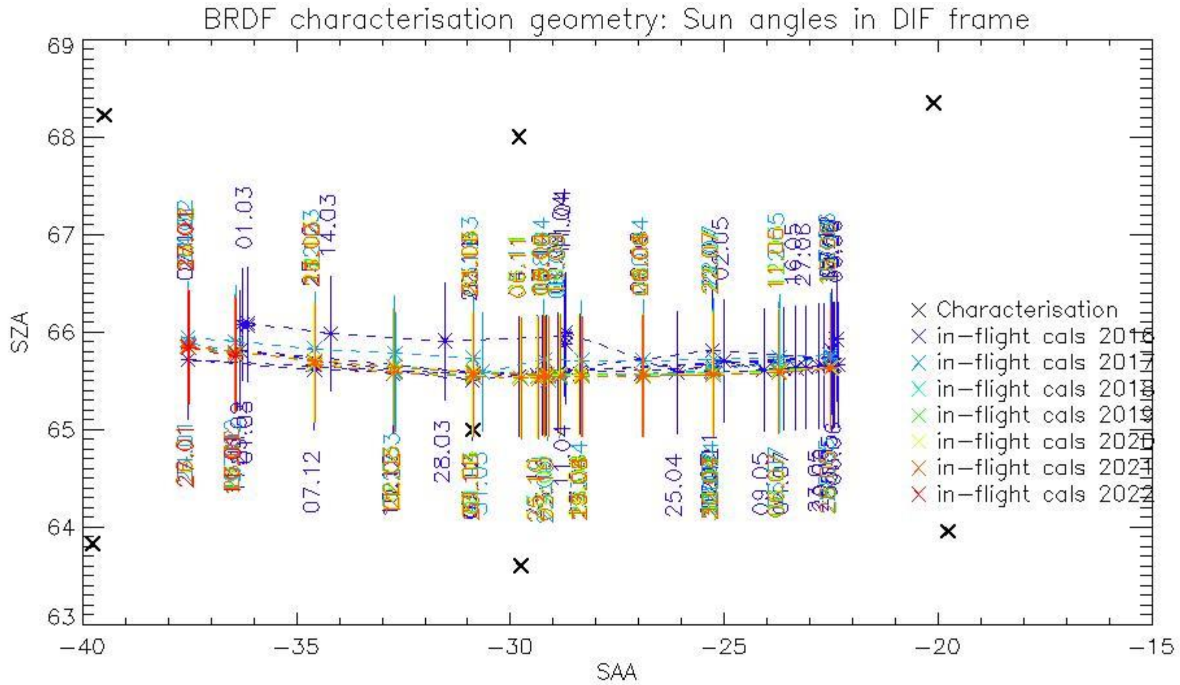

Figure 7: OLCI-A Sun geometry during radiometric Calibrations on top of characterization ones (diffuser frame)

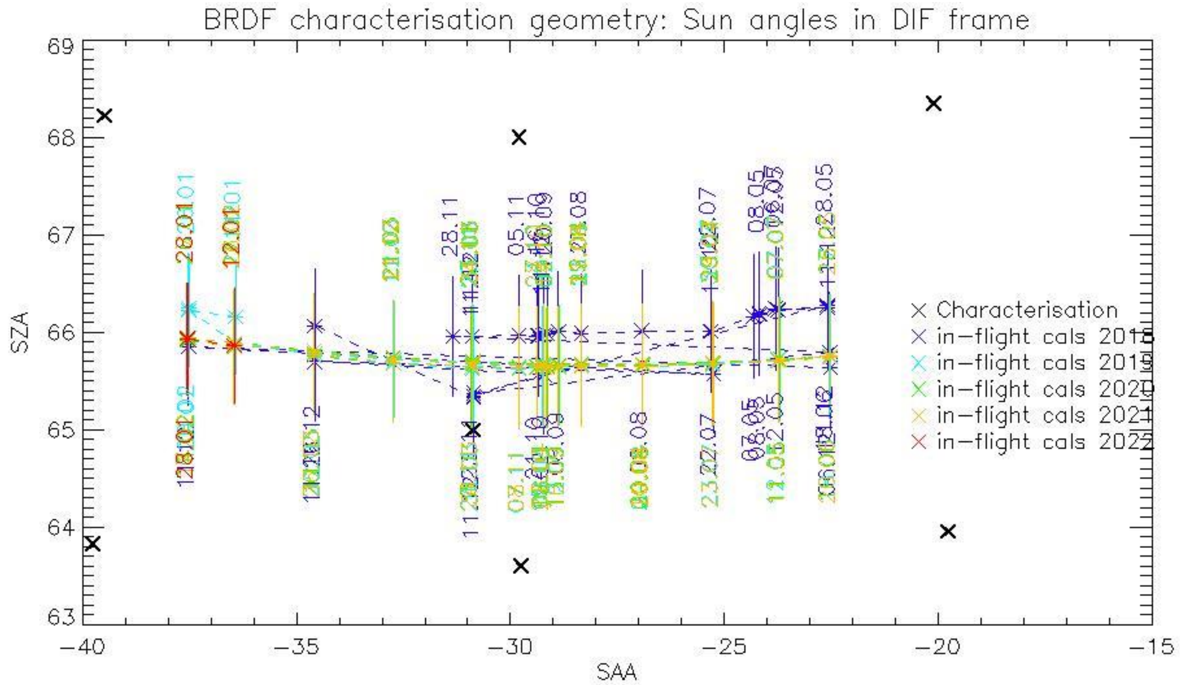

Figure 8: same as Figure 7 for OLCI-B

2.2.1 Dark Offsets [OLCI-L1B-CV-230]

Note about the High Energy Particles:

The filtering of High Energy Particle (HEP) events from radiometric calibration data has been implemented (for shutter frames only) in a post processor, allowing generating Dark Offset and Dark Current tables computed on filtered data. The post-processor starts from IPF intermediate data (corrected counts), applies the HEP detection and filtering and finally computes the Dark Offset and Dark Current tables the same way as IPF. An example of the impact of HEP filtering is given in Figure 9.

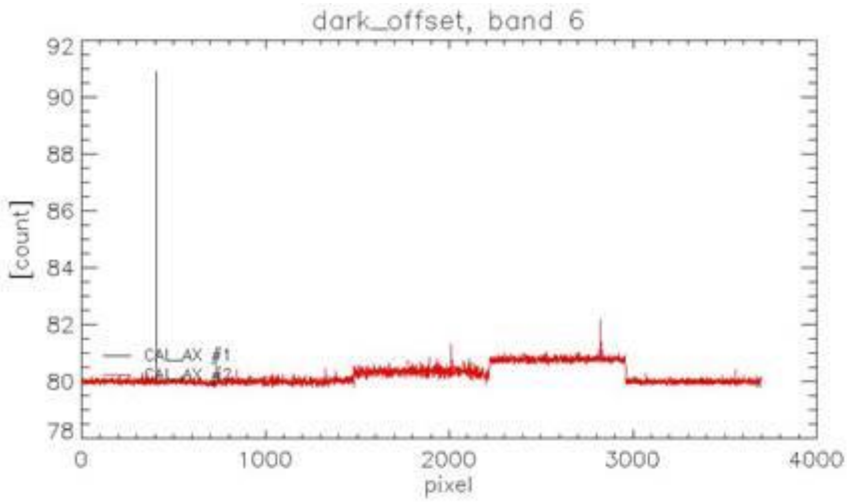

Figure 9: Dark Offset table for band Oa06 with (red) and without (black) HEP filtering (Radiometric Calibration of 22 July 2017). The strong HEP event near pixel 400 has been detected and removed by the HEP filtering.

All results presented below in this section have been obtained using the HEP filtered Dark Offset and Dark Current tables.

2.2.1.2 OLCI-A

Dark offsets

Dark offsets are continuously affected by the global offset induced by the Periodic Noise on the OCL convergence. Current Cycle calibrations are affected the same way as others. The amplitude of the shift varies with band and camera from virtually nothing (e.g. camera 2, band 0a1) to up to 5 counts (Oa21, camera 3). The Periodic Noise itself comes on top of the global shift with its known signature: high frequency oscillations with a rapid damp. This effect remains more or less stable with time in terms of amplitude, frequency and decay length, but its phase varies with time, introducing the global offset mentioned above.

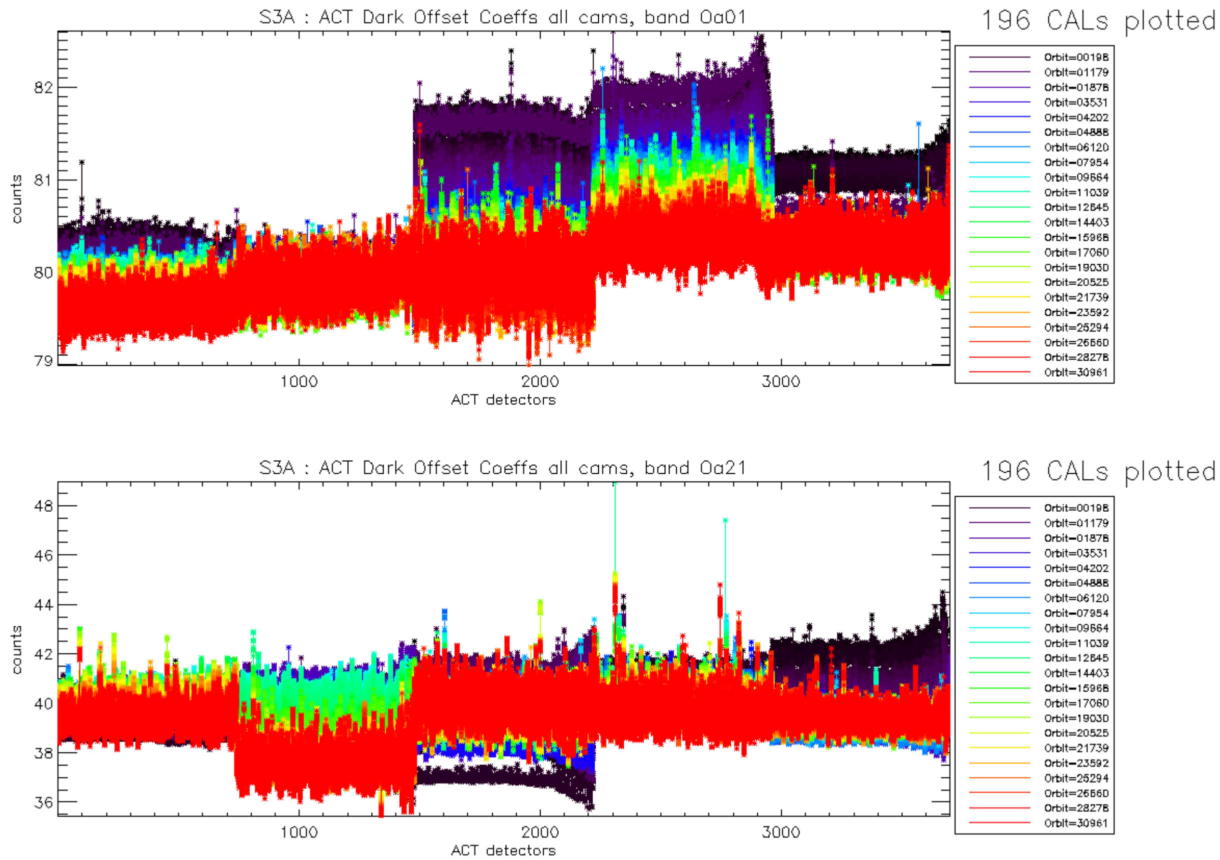

Figure 10: OLCI-A Dark Offset for band Oa1 (top) and Oa21 (bottom), all radiometric calibrations so far except the first one (orbit 183) for which the instrument was not thermally stable yet.

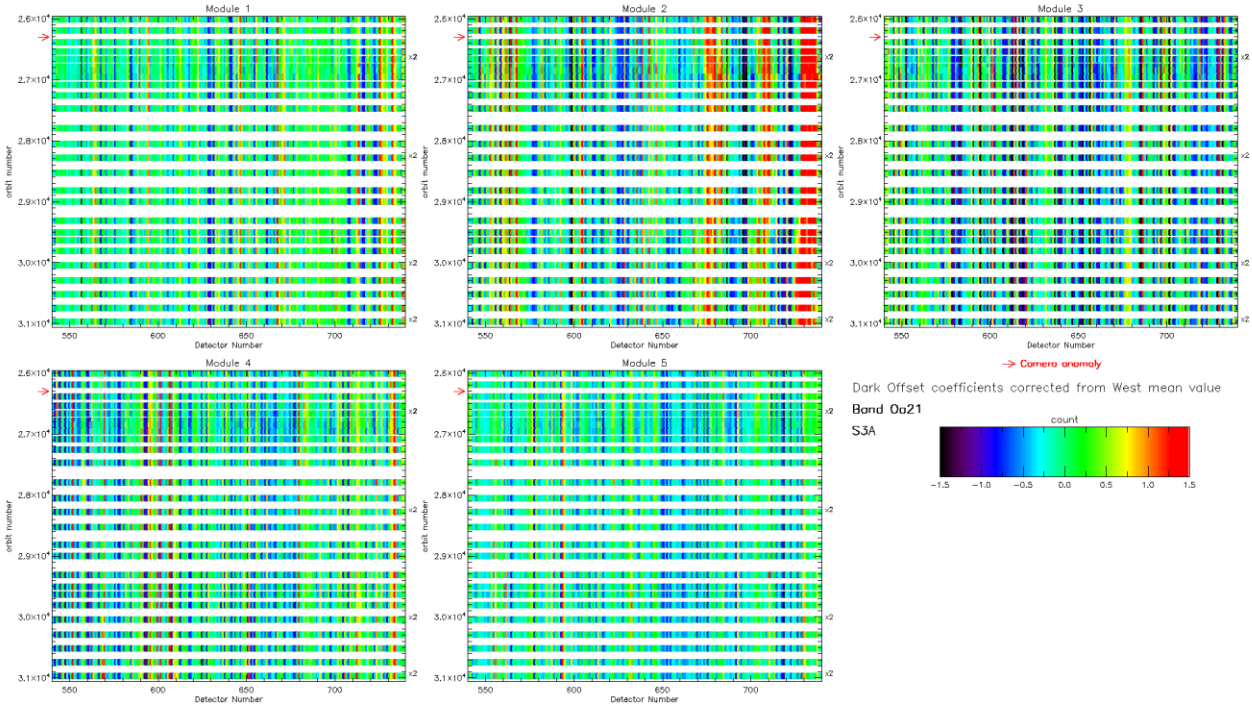

Figure 11: map of OLCI-A periodic noise for the 5 cameras, for band Oa21. X-axis is detector number (East part, from 540 to 740, where the periodic noise occurs), Y-axis is the orbit number. Y-axis range is focused on the most recent 5000 orbits. The counts have been corrected from the West detectors mean value (not affected by periodic noise) in order to remove mean level gaps and consequently to have a better visualisation of the long term evolution of the periodic noise structure. At the beginning of the mission the periodic noise for band Oa21 had strong amplitude in camera 2, 3 and 5 compared to camera 1 and 4. However PN evolved through the mission and these discrepancies between cameras have been reduced. At the time of this Cyclic Report Camera 2 still shows a slightly higher PN than other cameras.

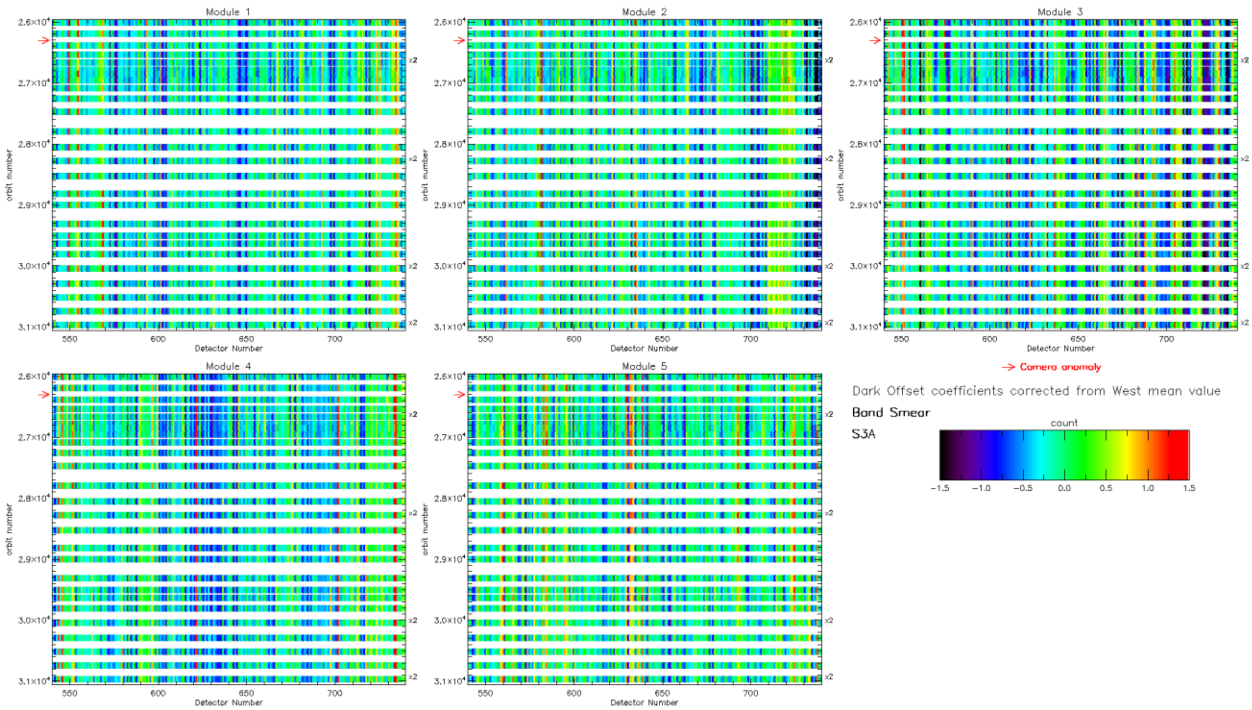

Figure 12: same as Figure 11 for smear band.

Figure 11 and Figure 12 show the so-called 'map of periodic noise' in the 5 cameras, for respectively band 21 and smear band. These maps have been computed from the dark offsets after removal of the mean level of the WEST detectors (not impacted by PN) in order to remove mean level gaps from one CAL to the other and consequently to highlight the shape of the PN. Maps are focused on the last 200 EAST detectors where PN occurs and on a time range covering only the last 5000 orbits in order to better visualize the CALs of the current cycle.

Figure 11 and Figure 12 show that at this stage of the mission the PN is very stable in all cameras. There is no special behaviour noticed during the reporting period.

Dark Currents

Dark Currents (Figure 13) are not affected by the global offset of the Dark Offsets, thanks to the clamping to the average blind pixels value. However, the oscillations of Periodic Noise remain visible. There is no significant evolution of this parameter during the current cycle except the small regular increase (almost linear), for all detectors, since the beginning of the mission (see Figure 14).

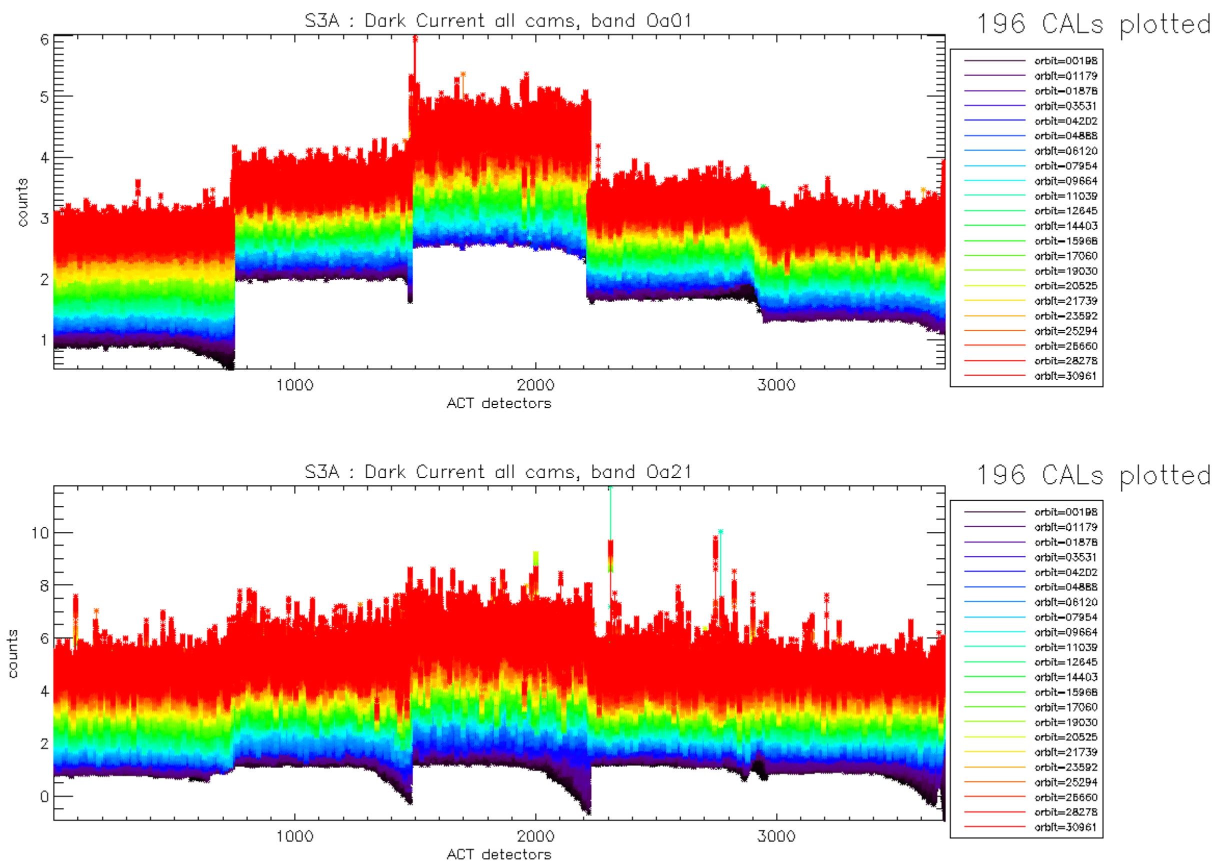

Figure 13: OLCI-A Dark Current for band Oa1 (top) and Oa21 (bottom), all radiometric calibrations so far except the first one (orbit 183) for which the instrument was not thermally stable yet.

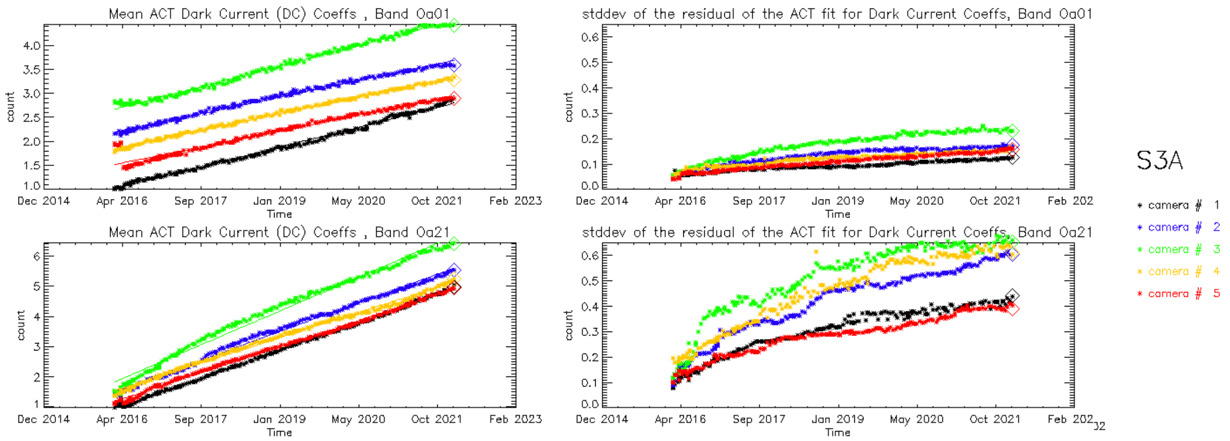

Figure 14: left column: ACT mean on 400 first detectors of OLCI-A Dark Current coefficients for spectral band Oa01 (top) and Oa21 (bottom). Right column: same as left column but for Standard deviation instead of mean. We see an increase of the DC level as a function of time especially for band Oa21.

A possible explanation of the regular increase of DC could be the increase of the number of hot pixels which is more important in Oa21 because this band is made of more CCD lines than band Oa01 and thus receives more cosmic rays impacts. It is known that cosmic rays degrade the structure of the CCD, generating more and more hot pixels at long term scales. Indeed, when computing the time slopes of the spatially averaged Dark Current as a function of band, i.e. the slopes of curves in left plots of Figure 14, one can see that Oa21 is by far the most affected, followed by the smear band (Figure 15, left); when plotting these slopes against total band width (in CCD rows, regardless of the number of micro-bands), the correlation between the slope values and the width becomes clear (Figure 15, right).

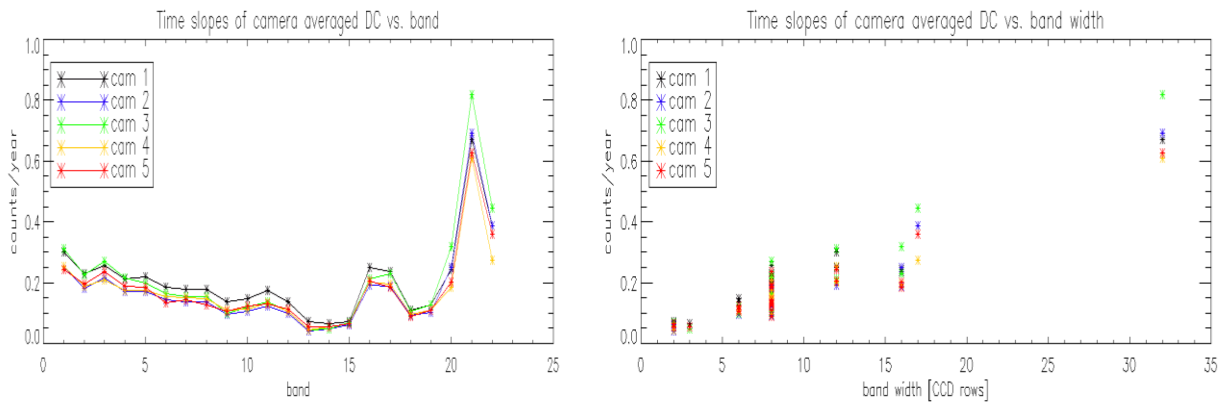

Figure 15: OLCI-A Dark current increase rates with time (in counts per year) vs. band (left) and vs. band width (right)

2.2.1.3 OLCI-B

Dark Offsets

Dark offsets for OLCI-B show a similar behaviour than for OLCI-A: mean level gaps between different orbits, induced by the presence of a pseudo periodic noise on the east edge of the cameras with a drifting phase.

Evolution of OLCI-B Dark Offset coefficients for band Oa01 and Oa21 are represented in Figure 16.

The periodic noise maps are shown for band Oa21 and smear band respectively in Figure 17 and Figure 18. As it happened for OLCI-A after a few thousands of orbits, the strong periodic noise phase and amplitude drift, present at the very beginning of the mission is now showing a clear stabilization.

Despite this overall stabilization, small evolutions are still noticeable in some bands/camera, like for example camera 1 in band Oa21 (upper left map in Figure 17) or in camera 1 band smear (upper left map in Figure 18).

Globally, OLCI-B PN is slightly less stabilized than OLCI-A PN.

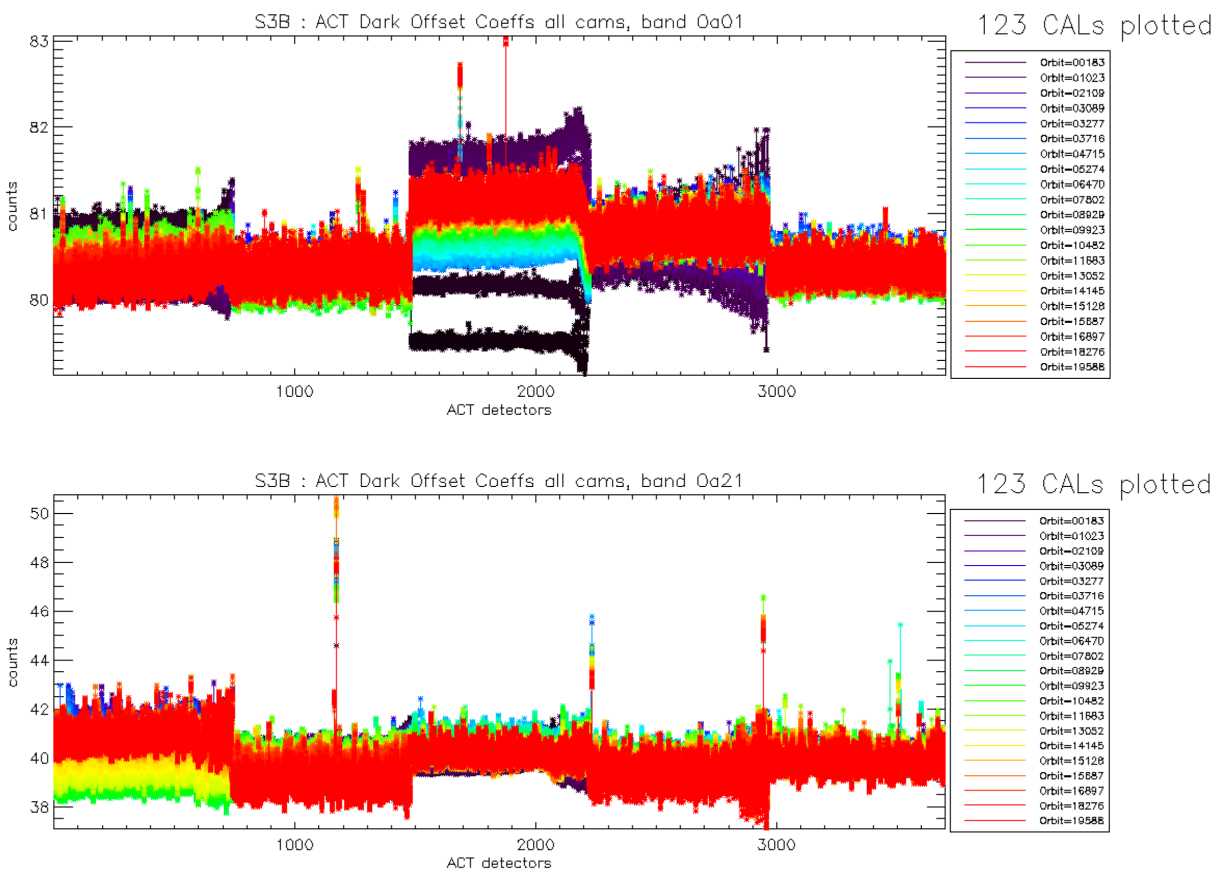

Figure 16: OLCI-B Dark Offset for band Oa1 (top) and Oa21 (bottom), all radiometric calibrations so far except the first one (orbit 167) for which the instrument was not thermally stable yet.

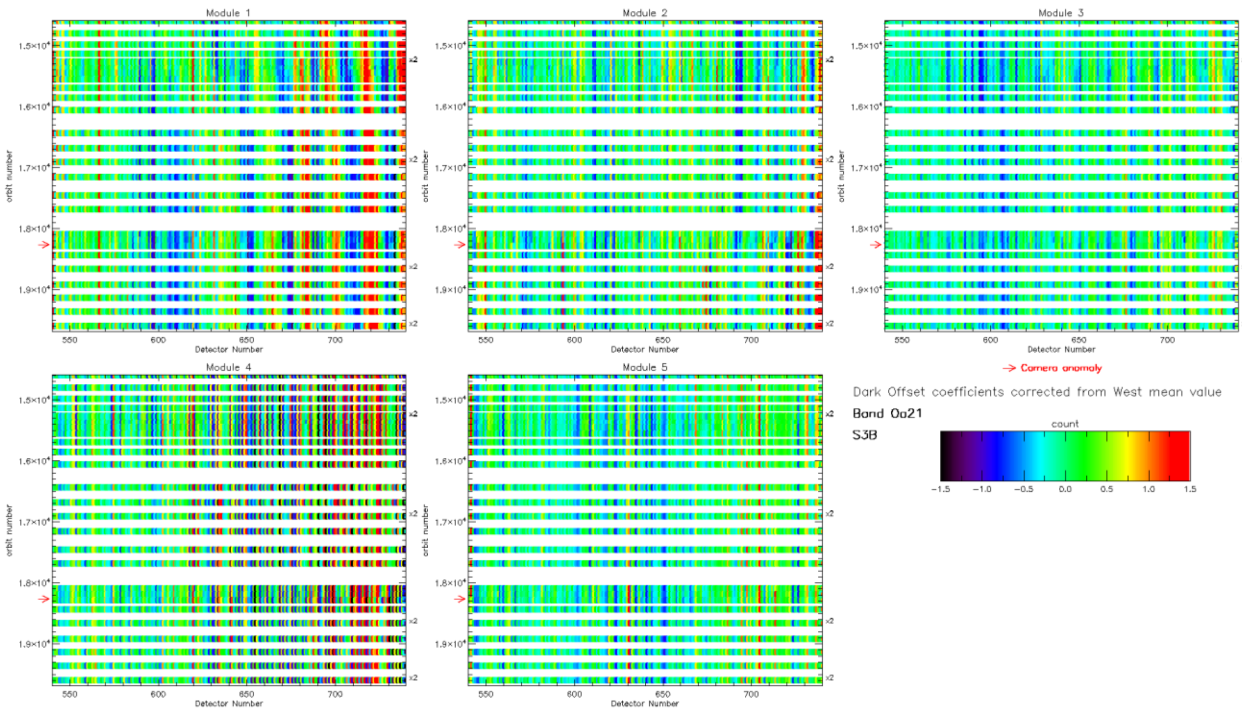

Figure 17: OLCI-B map of periodic noise for the 5 cameras, for band Oa21. X-axis is detector number (East part, from 540 to 740, where the periodic noise occurs), Y-axis is the orbit number. The counts have been corrected from the West detectors mean value (not affected by periodic noise) in order to remove mean level gaps and consequently to have a better visualisation of the long term evolution of the periodic noise structure.

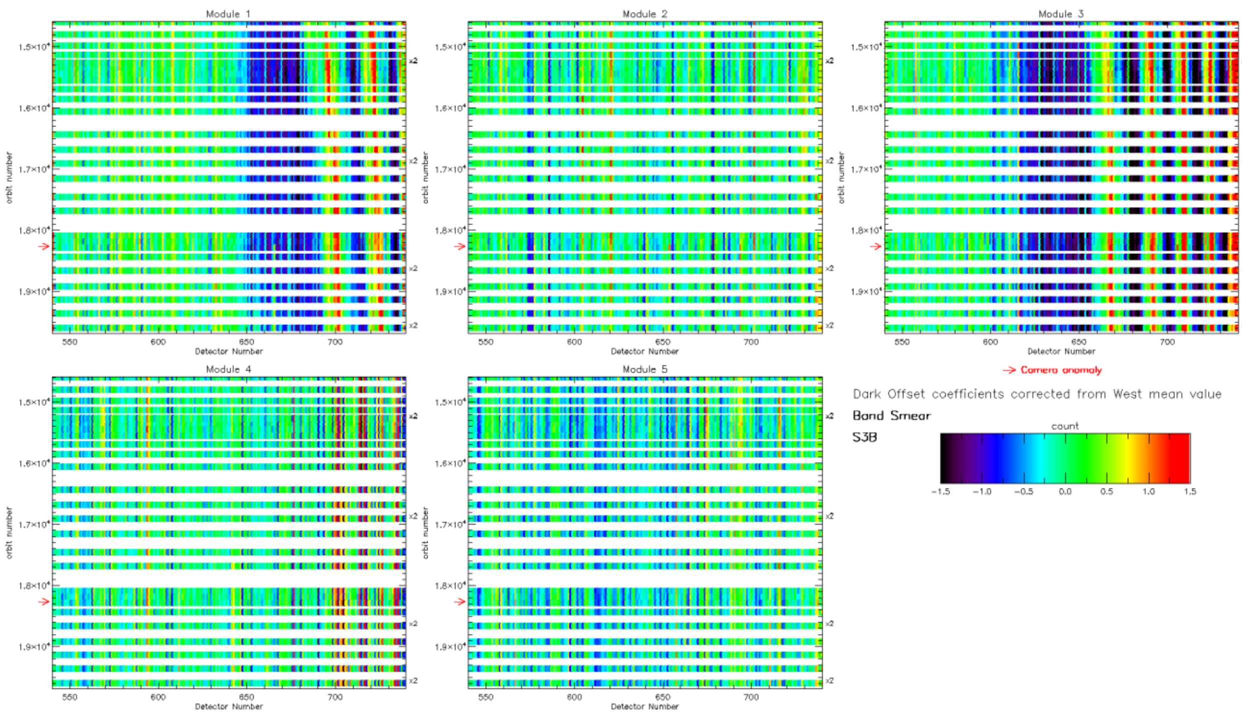

Figure 18: same as Figure 17 for smear band.

Dark Currents

As for OLCI-A there is no significant evolution of the Dark Current coefficients (Figure 19) during the current cycle except the small regular increase (almost linear), for all detectors, since the beginning of the mission (see Figure 20) probably due to an increase of hot pixels (see Figure 21).

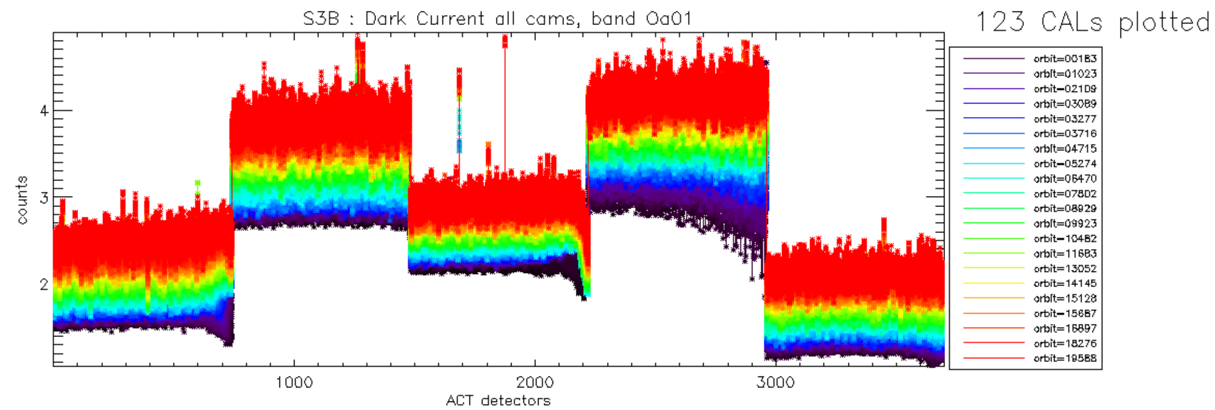

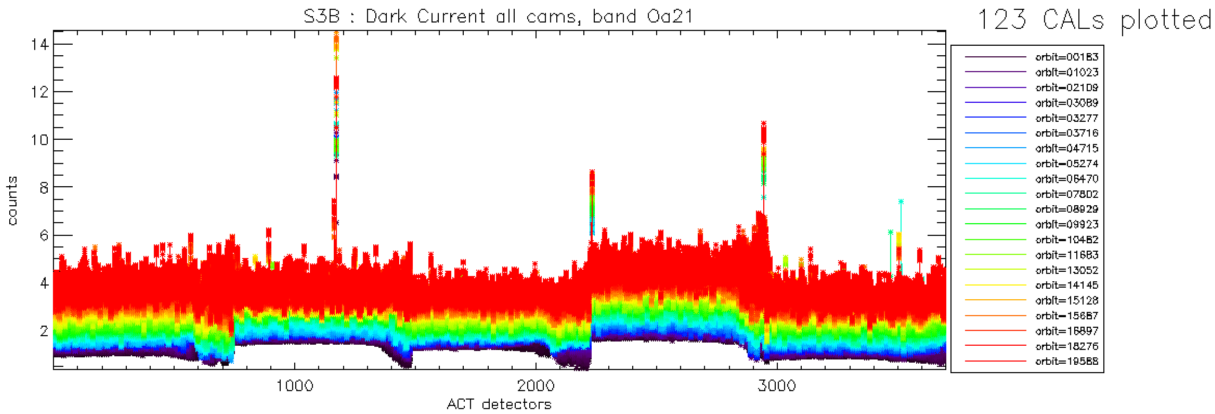

Figure 19: OLCI-B Dark Current for band Oa1 (top) and Oa21 (bottom), all radiometric calibrations so far except the first one (orbit 167) for which the instrument was not thermally stable yet.

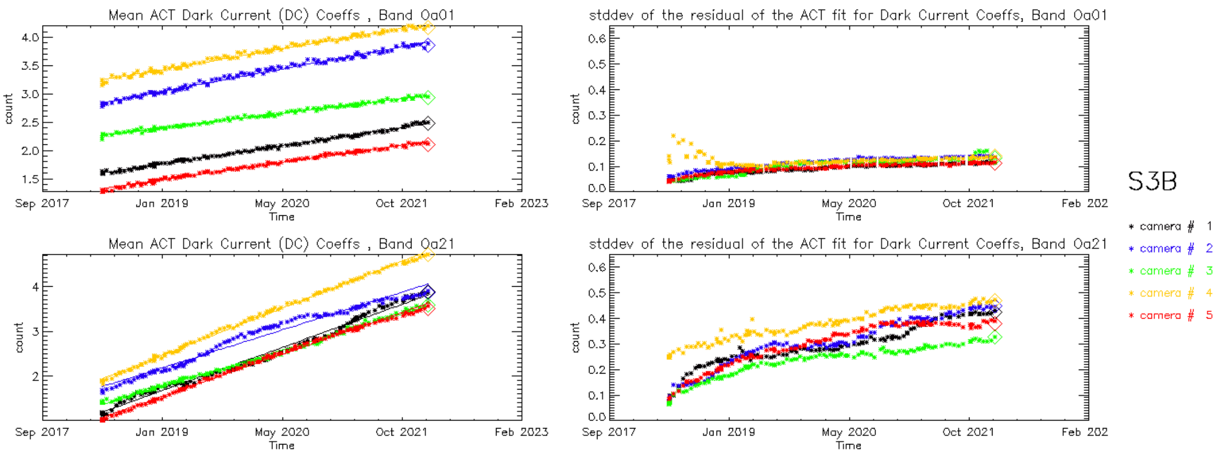

Figure 20: left column: ACT mean on 400 first detectors of OLCI-B Dark Current coefficients for spectral band Oa01 (top) and Oa21 (bottom). Right column: same as left column but for Standard deviation instead of mean. We see an increase of the DC level as a function of time especially for band Oa21.

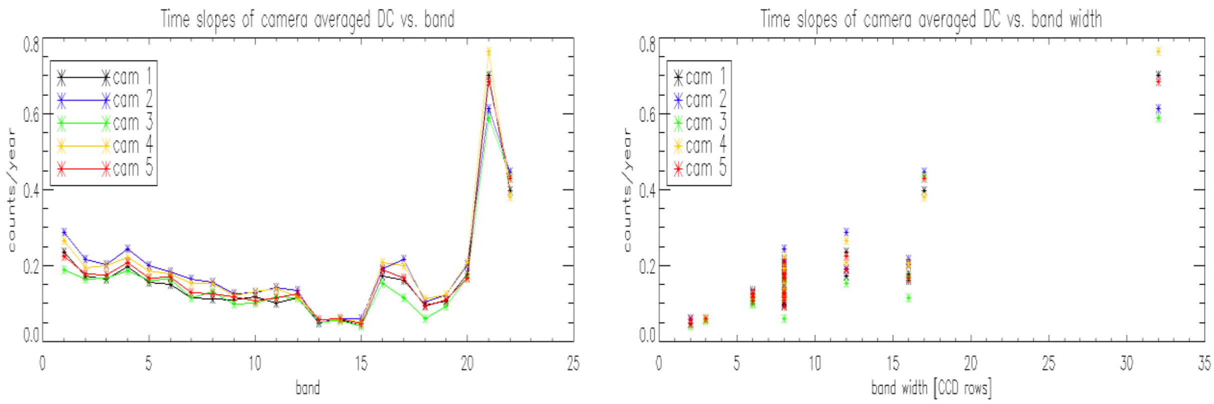

Figure 21: OLCI-B Dark Current increase rates with time (in counts per year) vs. band (left) and vs. band width (right)

2.2.2 Instrument response and degradation modelling [OLCI-L1B-CV-250]

2.2.2.1 Instrument response monitoring

2.2.2.1.1 OLCI-A

Figure 22 shows the gain coefficients of every pixel for two OLCI-A channels, Oa1 (400 nm) and Oa21 (1020 nm), highlighting the significant evolution of the instrument response since early mission.

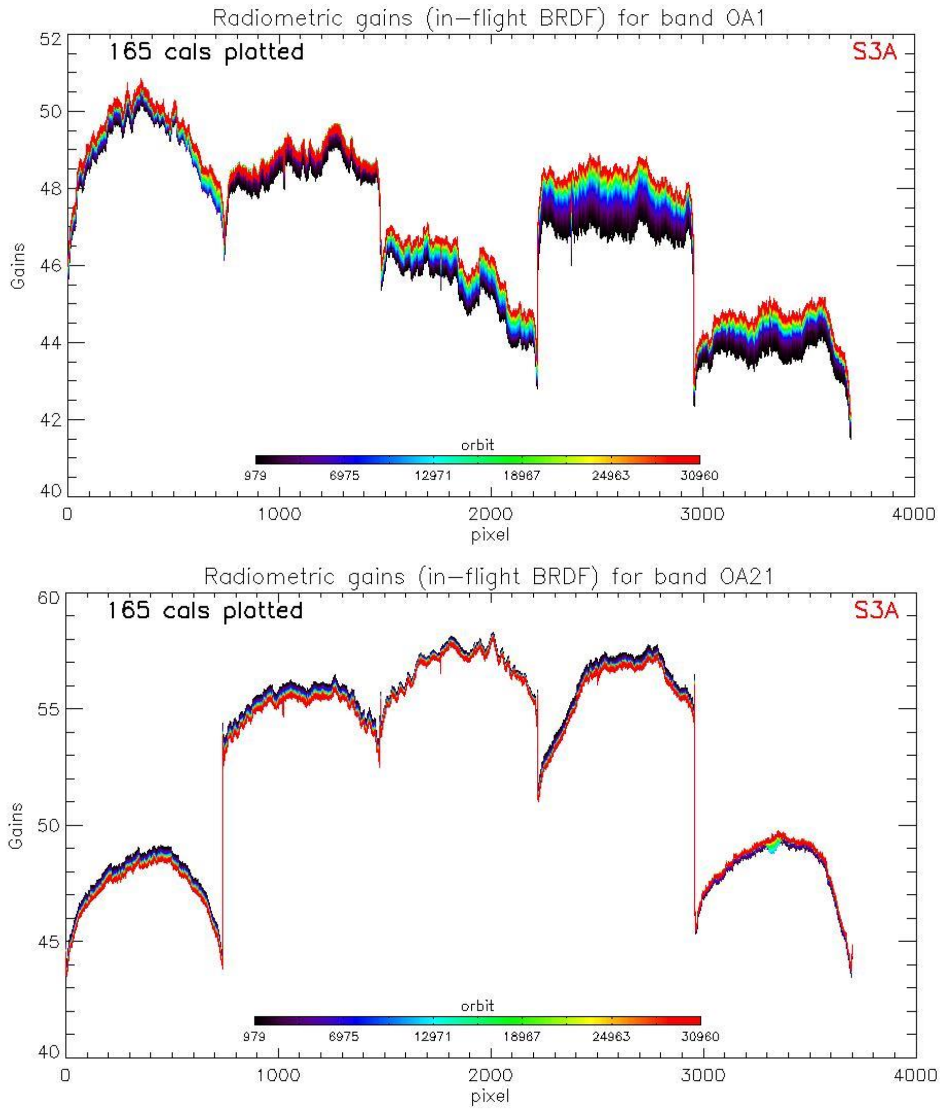

Figure 22: OLCI-A Gain Coefficients for band Oa1 (top) and Oa21 (bottom), derived using the in-flight BRDF model. The dataset is made of all diffuser 1 radiometric calibrations since orbit 979.

Figure 23 displays a summary of the time evolution of the cross-track average of the gains (in-flight BRDF, taking into account the diffuser ageing), for each module, relative to a given reference calibration (the 25/04/2016, change of OLCI channel settings). It shows that, if a significant evolution occurred during the early mission, the trends tend in general to stabilize, with some exceptions (e.g. band 1 of camera 1 and 4, bands 2 & 3 of camera 5).

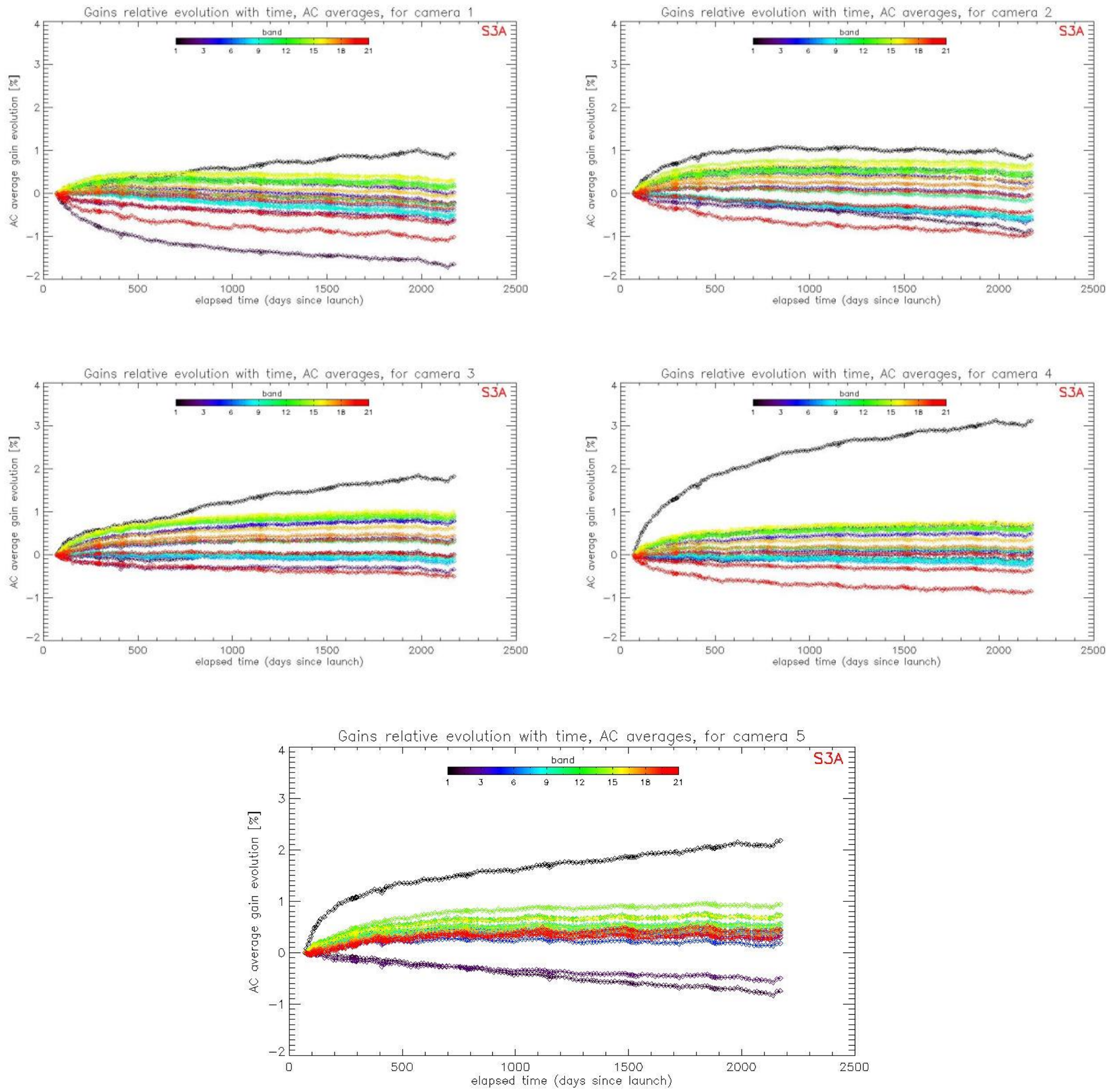

Figure 23: camera averaged gain relative evolution with respect to calibration of 25/04/2016 (change of OLCI channel settings), as a function of elapsed time since the beginning of the mission; one curve for each band (see colour code on plots), one plot for each module. The diffuser ageing has been taken into account.

2.2.2.1.2 OLCI-B

Figure 24 shows the gain coefficients of every pixel for two OLCI-B channels, Oa1 (400 nm) and Oa21 (1020 nm), highlighting the significant evolution of the instrument response since early mission.

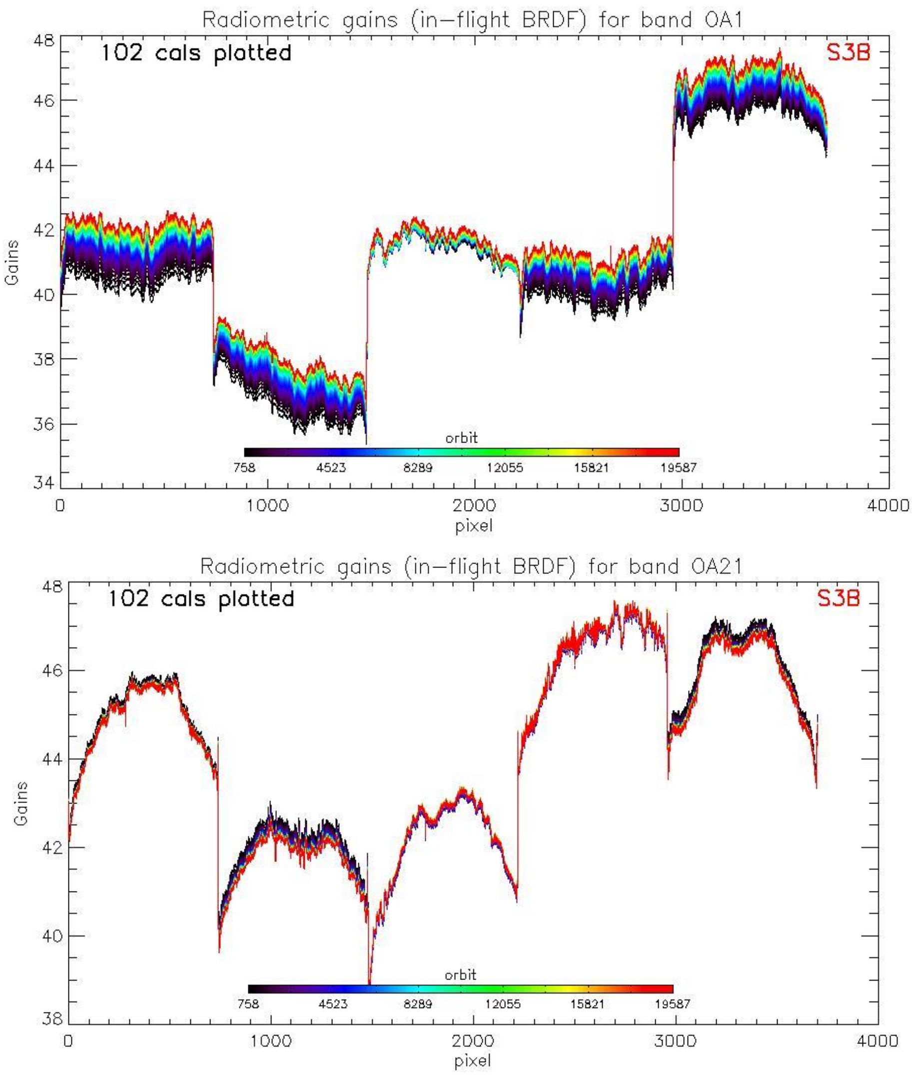

Figure 24: OLCI-B Gain Coefficients for band Oa1 (top) and Oa21 (bottom), derived using the in-flight BRDF model. The dataset is made of all diffuser 1 radiometric calibrations since orbit 758.

Figure 25 displays a summary of the time evolution of the cross-track average of the gains (in-flight BRDF, taking into account diffuser ageing), for each module, relative to a given reference calibration (first calibration after channel programming change: 18/06/2018). It shows that, if a significant evolution occurred during the early mission, the trends tend to stabilize. The large amount of points near elapsed time = 220 days is due to the yaw manoeuvre campaign. The slight discontinuity near "day 920 since launch" is due to the upgrade of the Ageing model.

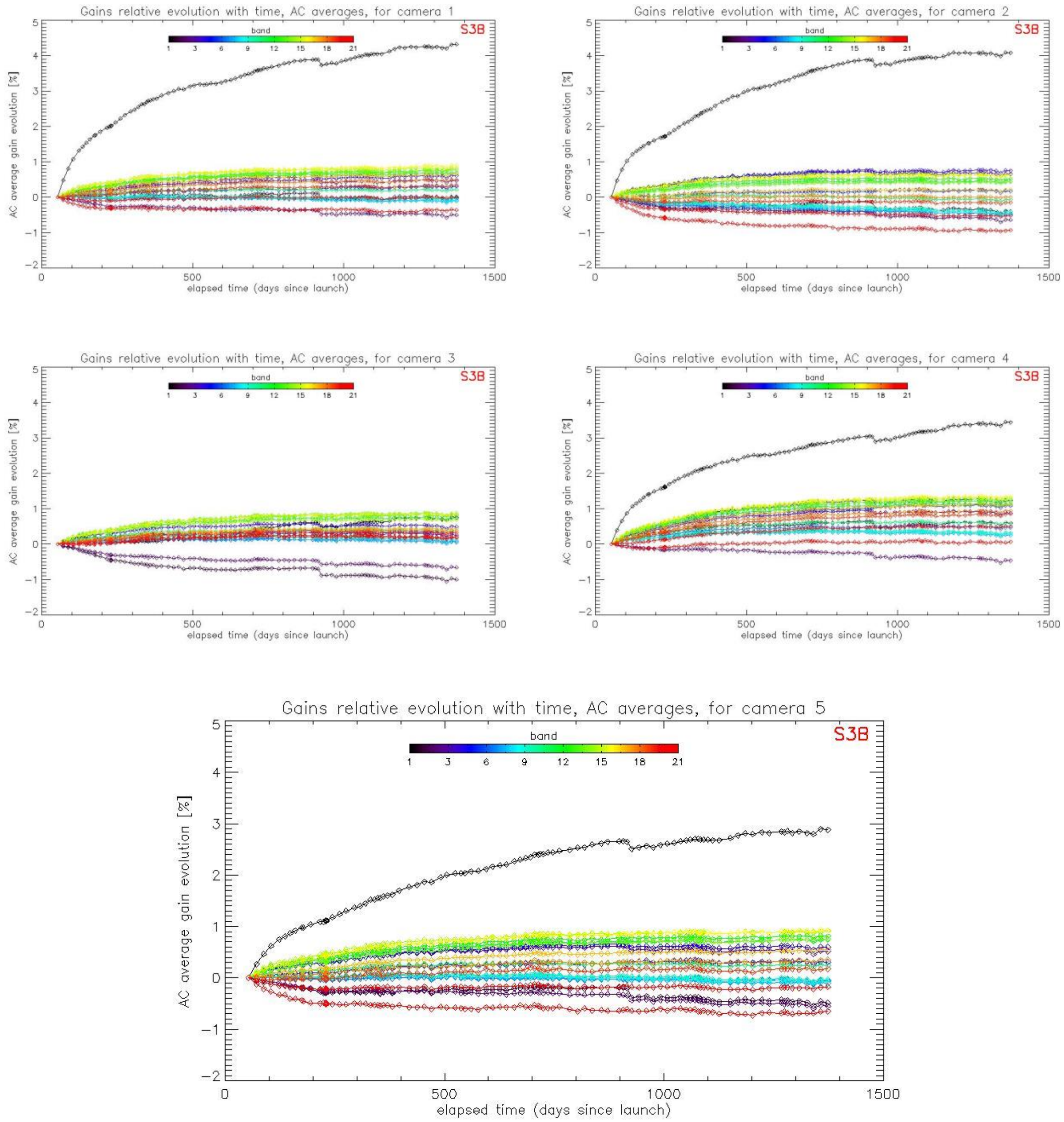

Figure 25: OLCI-B camera averaged gain relative evolution with respect to first calibration after channel programming change (18/06/2018), as a function of elapsed time since the beginning of the mission; one curve for each band (see colour code on plots), one plot for each module. The diffuser ageing has been taken into account.

2.2.2.2 Instrument evolution modelling

2.2.2.2.1 OLCI-A

The current OLCI-A Radiometric Model has been put in operations at PDGS the 18/11/2021 (Processing Baseline 3.01). This model has been derived on the basis of a more recent (compared to the previous model) Radiometric Calibration dataset, going from 25/01/2018 to 03/10/2021. It includes the correction of the diffuser ageing for the six bluest bands (Oa1 to Oa6) for which it is clearly measurable. The model performance over the complete dataset (including the 8 calibrations in extrapolation over about 4 months) remains better than about 0.09% for all bands at the exception of the presence of an isolated peak in the recent data near orbit 30500 where performance degrades for all bands, up to about 0.13% for band Oa01. This peak is present in Gain measurements, thus reflects in model performance. It is not yet understood and is under investigation. The same behaviour is seen on OLCI-B (see Figure 33). The previous model, trained on a Radiometric Dataset limited to 08/08/2020, shows clearly a more pronounced drift of the model with respect to most recent data (Figure 27). Comparison of the two figures shows the improvement brought by the updated Model over almost all the mission. Performance shown on Figure 26 adopts, as for OLCI-B, the multiple model approach, i.e. different models (three for OLCI-A since PB, three for OLCI-B since PB 1.57) are used to cover the whole mission (red dashed line on Figure 26), each model being fitted on a partial dataset (green dashed line on Figure 26) whose coverage is optimised to provide best performance.

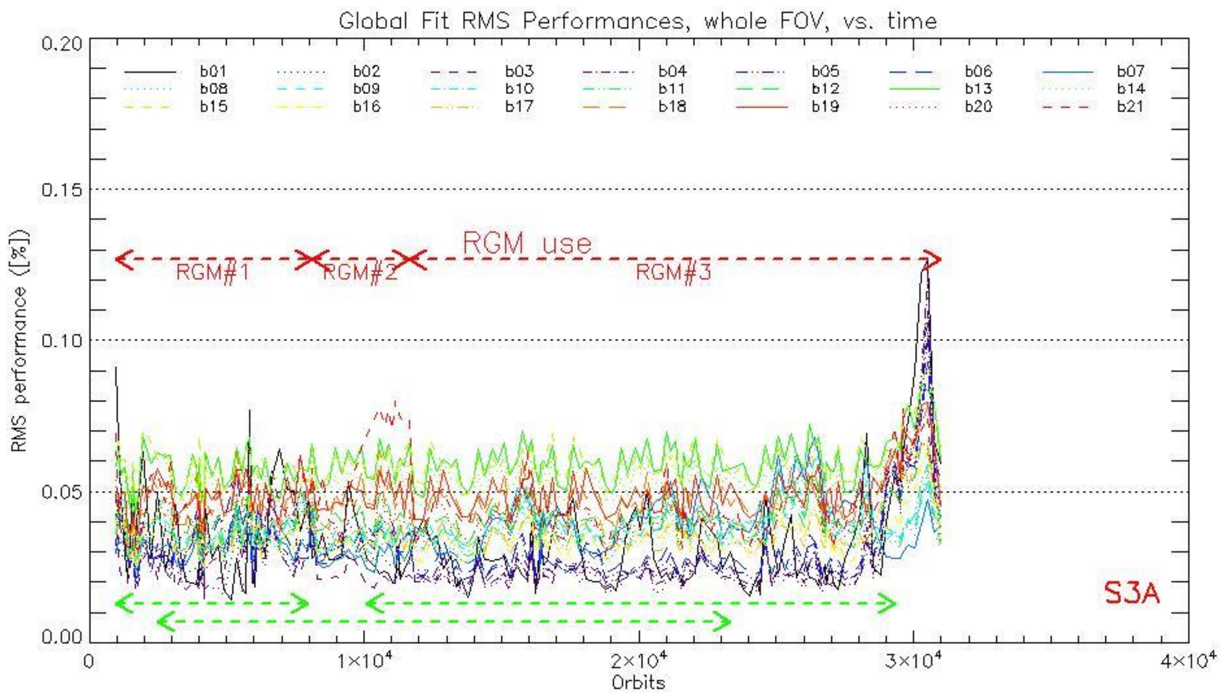

Figure 26: RMS performance of the OLCI-A Gain Model of the current processing baseline as a function of orbit.

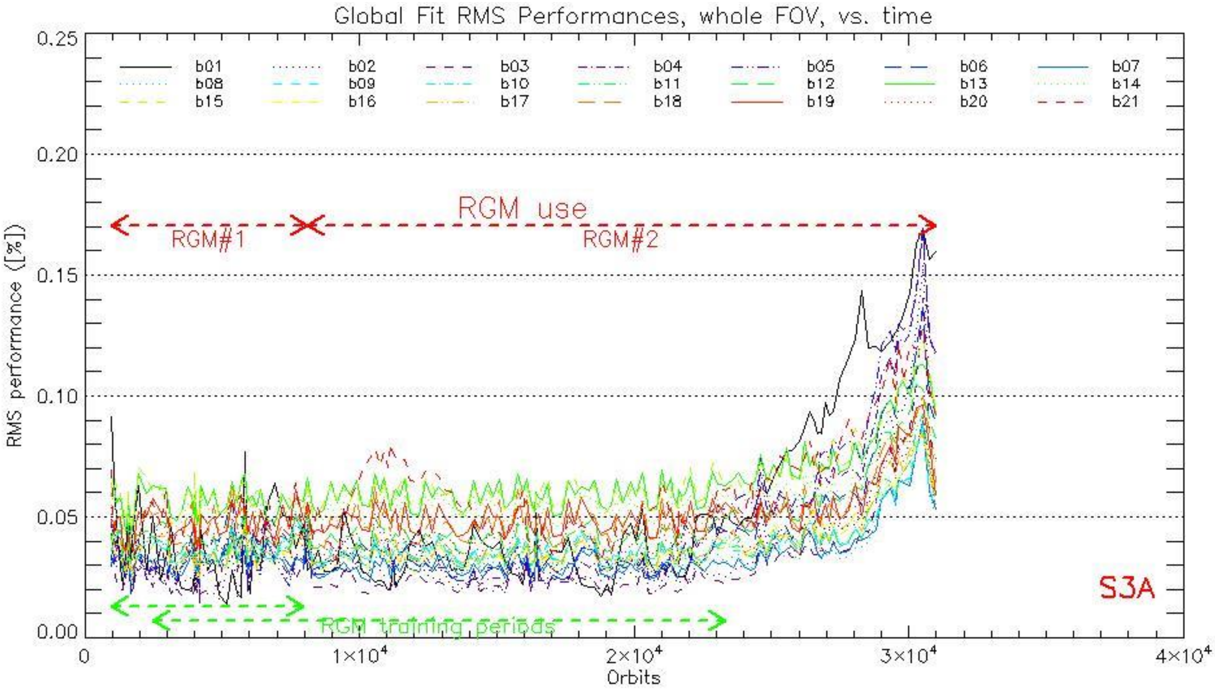

Figure 27: RMS performance of the OLCI-A Gain Model of the previous Processing Baseline as a function of orbit.

The overall instrument evolution since channel programming change (25/04/2016) is shown on Figure 28.

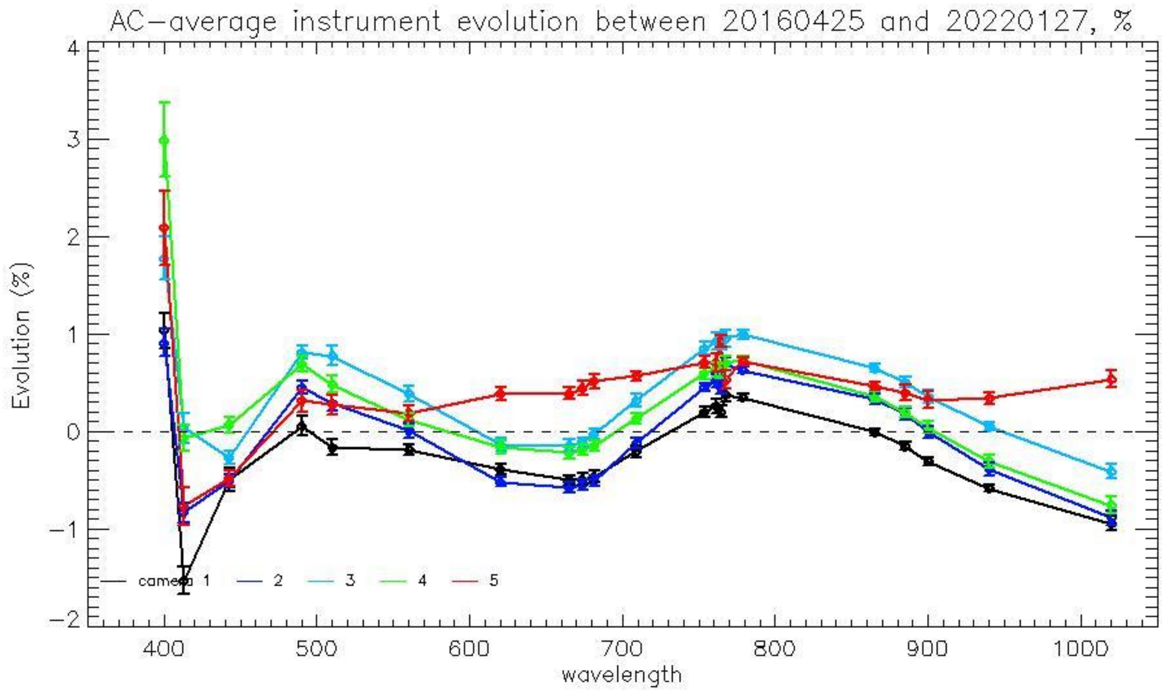

Figure 28: OLCI-A Camera-averaged instrument evolution since channel programming change (25/04/2016) and up to the most recent calibration (27/01/2022) versus wavelength.

The overall per camera performance, as a function of wavelength, and at each orbit is shown on Figure 29 as the average and standard deviation of the model over data ratio.

Finally, Figure 30 to Figure 32 show the detail of the model performance, with across-track plots of the model over data ratios at each orbit, one plot for each channel.

Comparisons of Figure 30 to Figure 32 with their counterparts in Report of Cycle 62 clearly demonstrate the improvement brought by the new model whatever the level of detail.

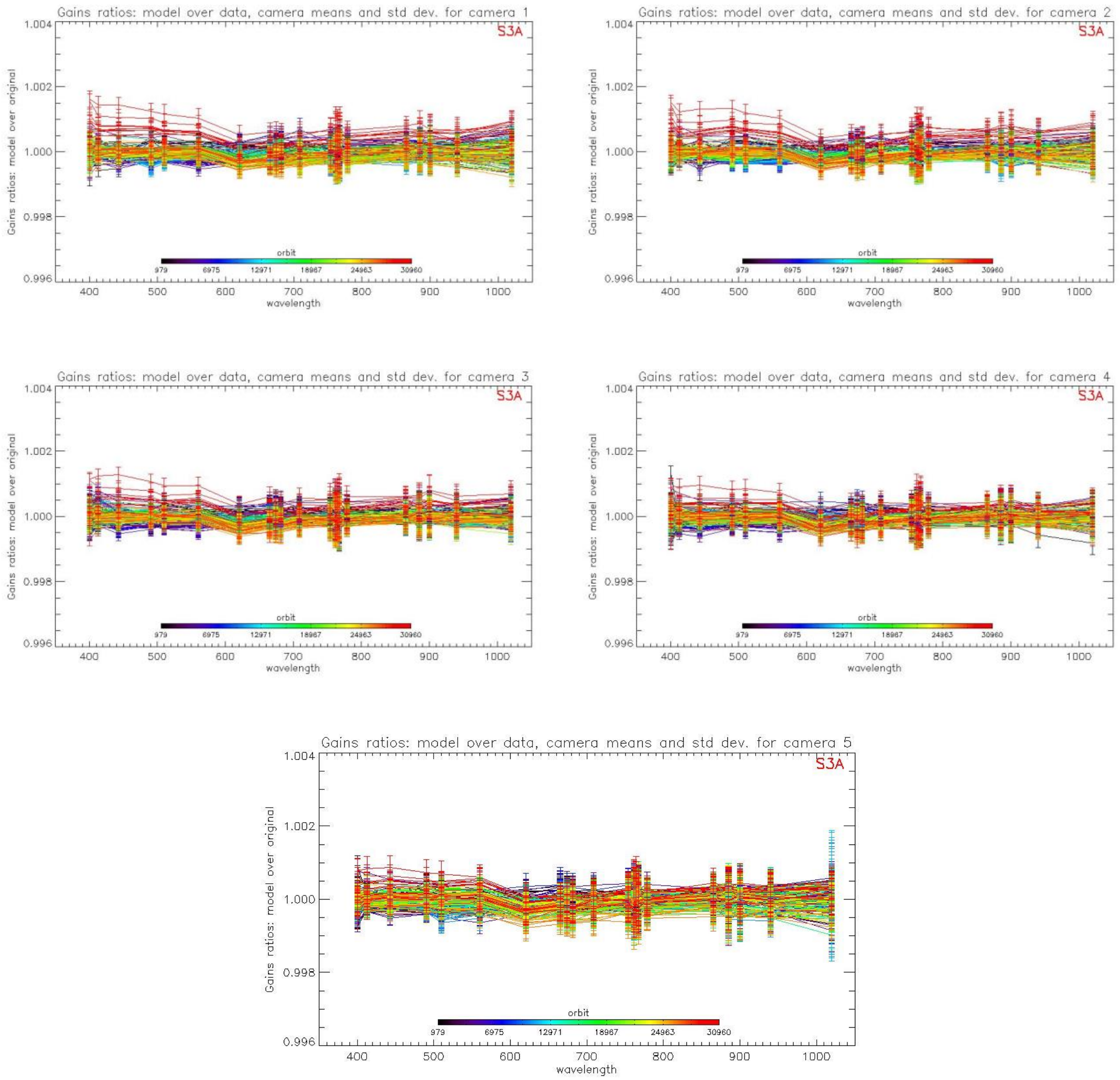

Figure 29: For the 5 cameras: OLCI-A Evolution model performance, as camera-average and standard deviation of ratio of Model over Data vs. wavelength, for each orbit of the test dataset, including 8 calibrations in extrapolation, with a colour code for each calibration from blue (oldest) to red (most recent).

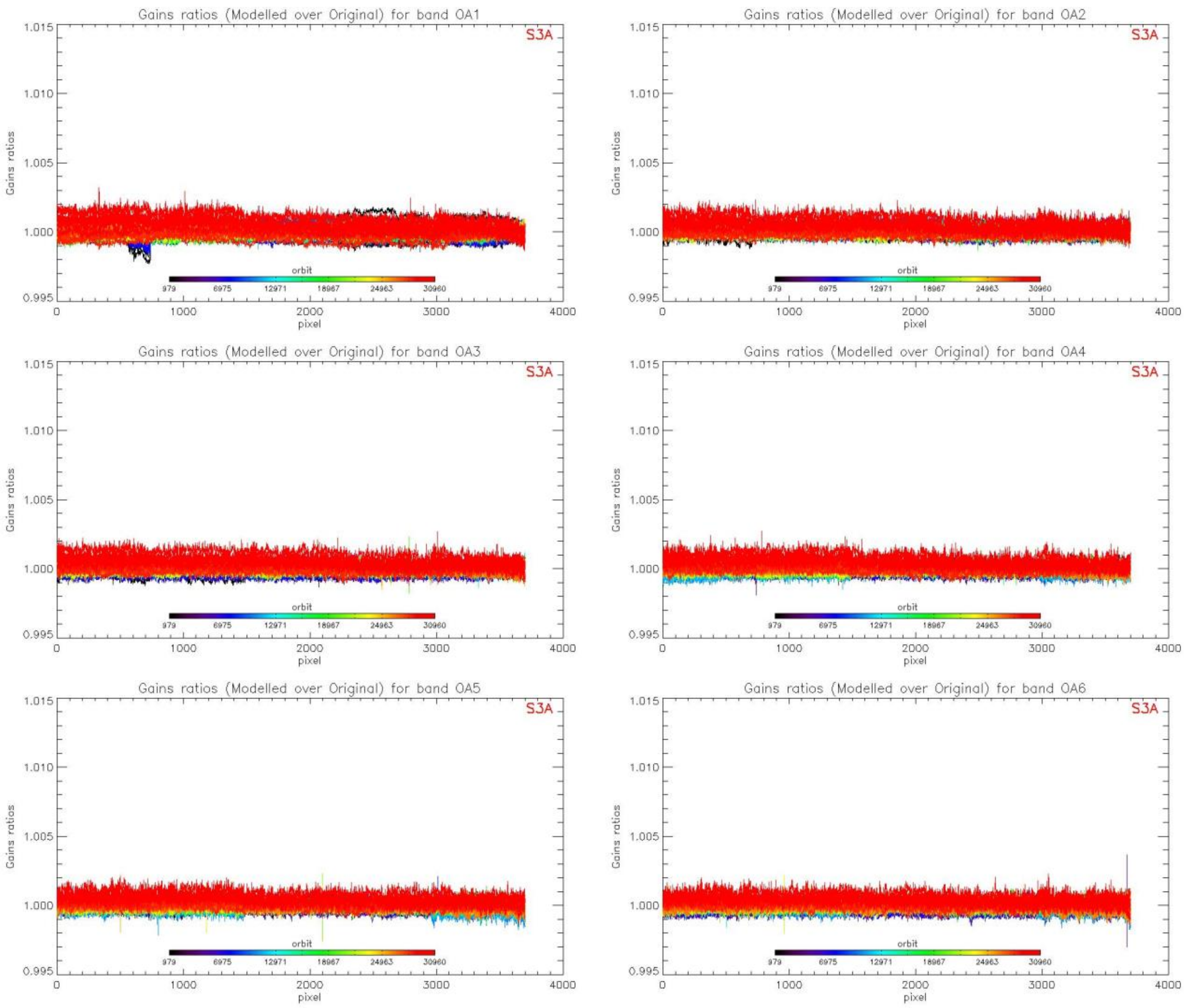

Figure 30: OLCI-A evolution model performance, as ratio of Model over Data vs. pixels, all cameras side by side, over the whole current calibration dataset (since instrument programing update), including 8 calibrations in extrapolation, channels Oa1 to Oa6.

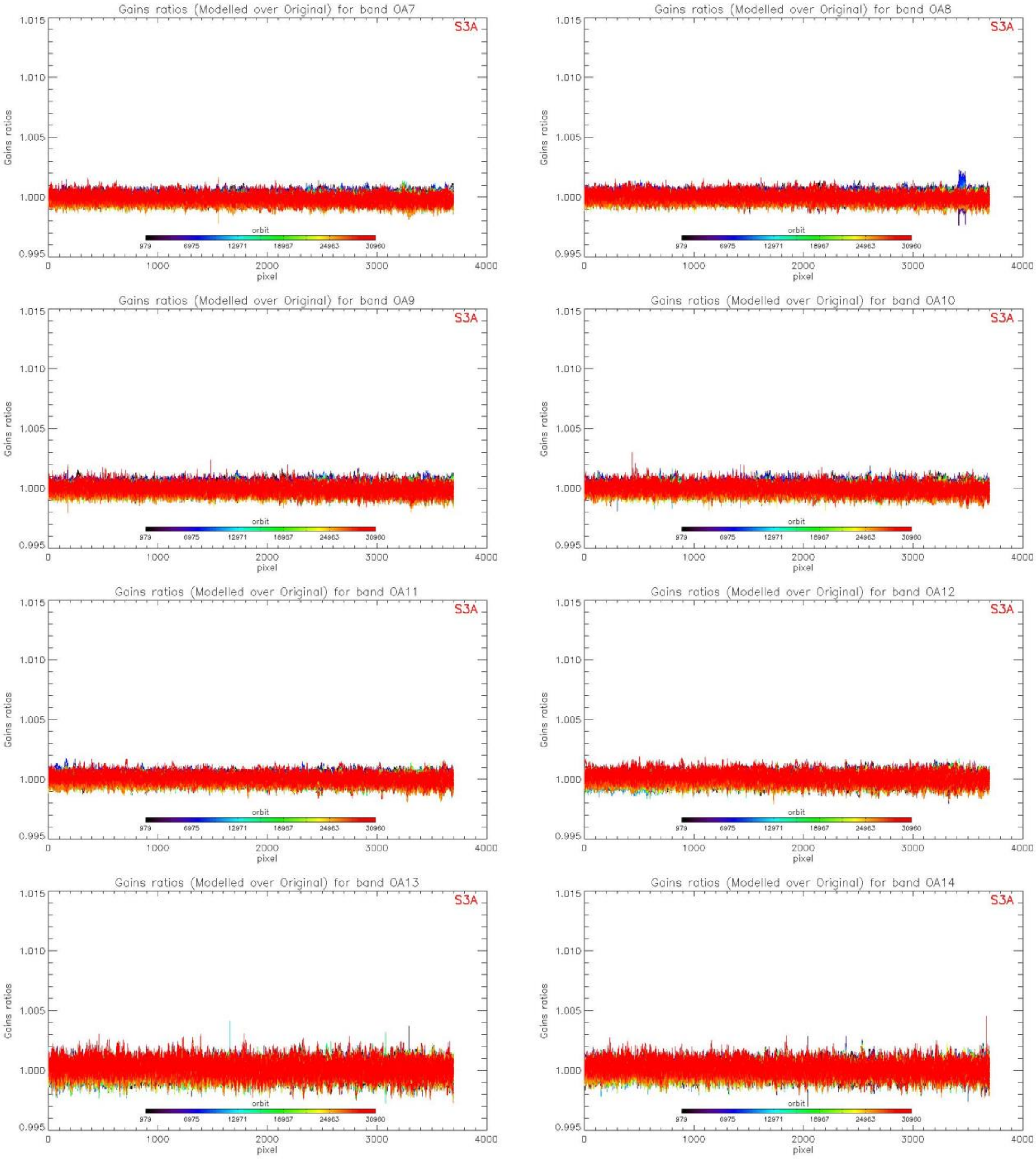

Figure 31: same as Figure 30 for channels Oa7 to Oa14.

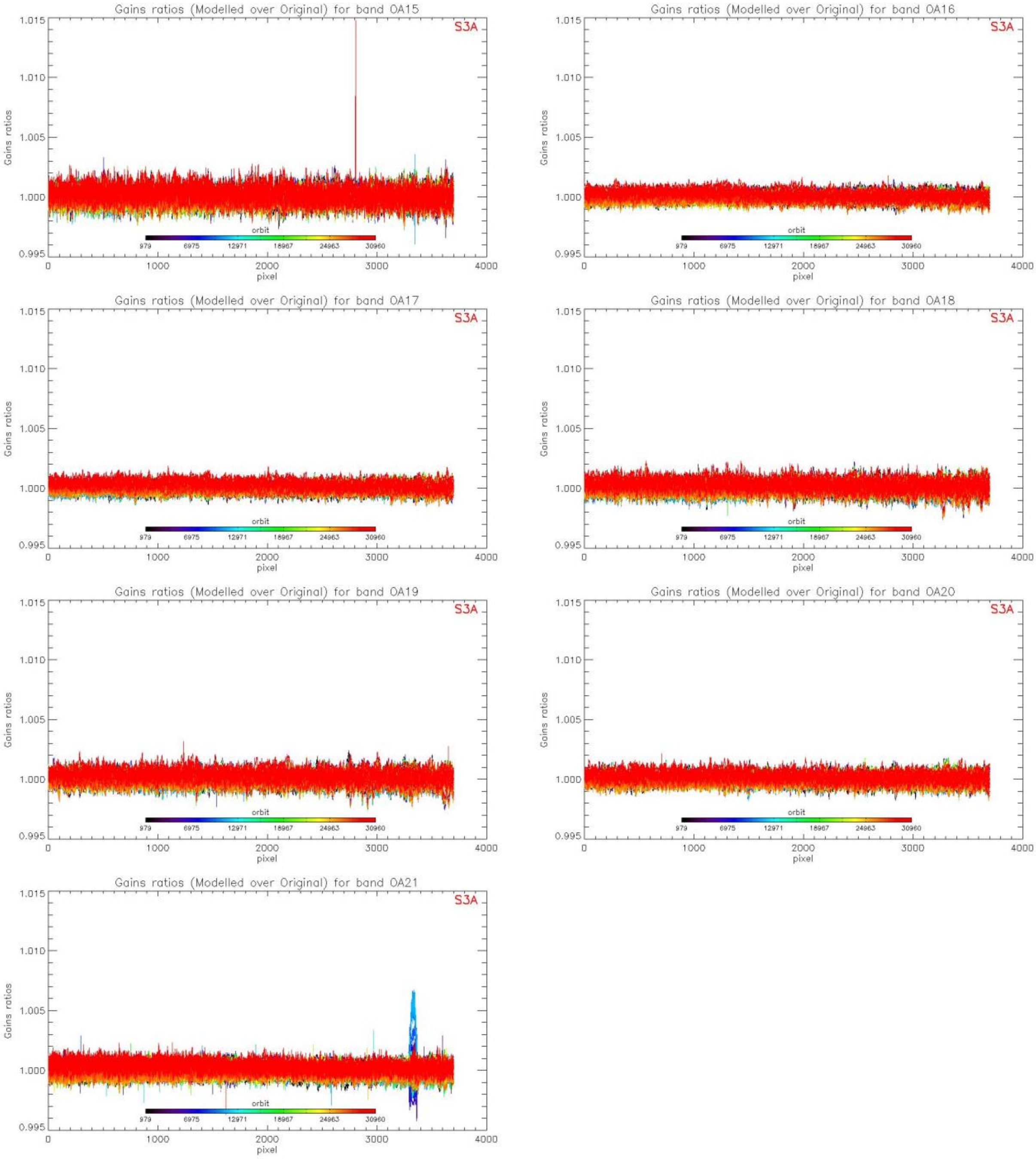

Figure 32: same as Figure 30 for channels Oa15 to Oa21.

2.2.2.2.2 OLCI-B

The current instrument response and degradation modelling for OLCI-B, including the use of the in-flight BRDF model (based on 11th December 2018 Yaw Manoeuvres), has been deployed at PDGS on 18/11/2021 (Processing Baseline 3.01). This model has been derived on the basis of an extended Radiometric Calibration dataset (from 18/06/2019 to 16/09/2021), and most of all a revised Ageing model. It includes the correction of the diffuser ageing for the five bluest bands (Oa1 to Oa5) for which it is clearly measurable. The model performance over the complete dataset (including 9 calibrations in extrapolation over about 4.5 months) is illustrated in Figure 33. It remains better than 0.10% when averaged over the whole field of view for all bands, at the exception of an isolated peak which is present in recent data near orbit 19000 where performance degrades for all bands, up to about 0.15 % for band Oa01. This peak is present in Gain measurements, thus reflects in model performance. It is not yet understood and is under investigation. The same behaviour is seen on OLCI-A (see Figure 26). The previous model, trained on a Radiometric Dataset limited to 09/08/2020, shows a strong drift of the model with respect to most recent data, especially for band Oa01 (Figure 34). Comparison of the two figures shows the improvement brought by the updated Model over all the mission.

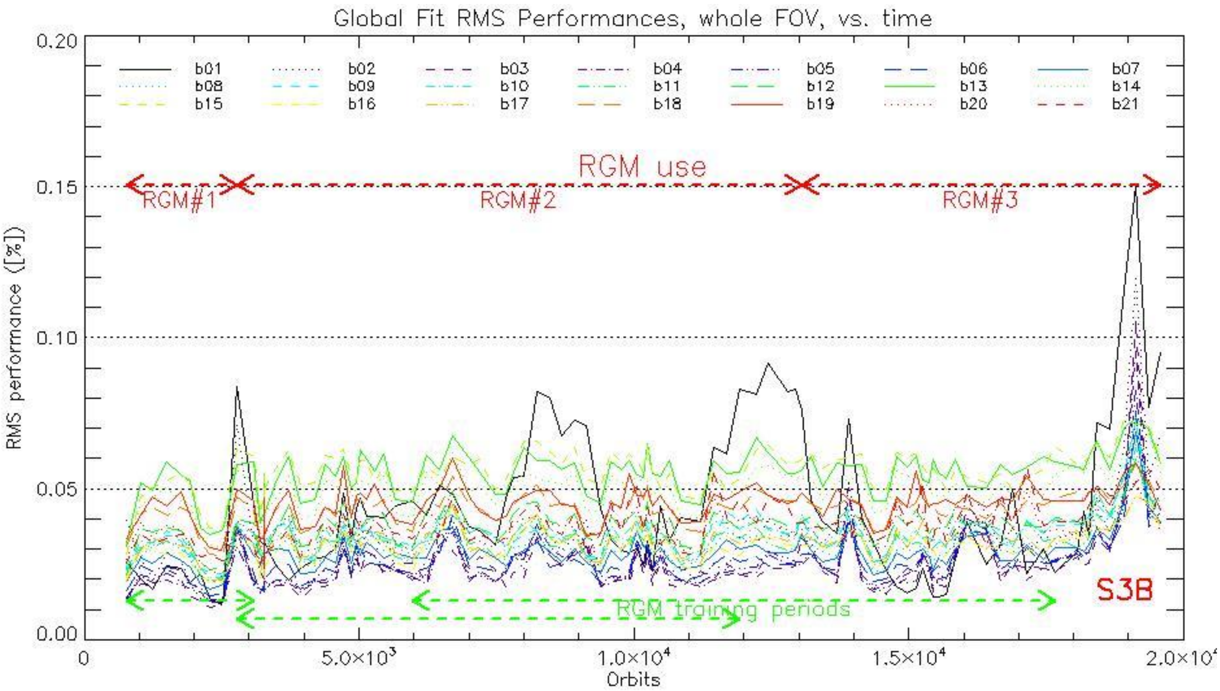

Figure 33: RMS performance of the OLCI-B Gain Model of the current processing baseline as a function of orbit.

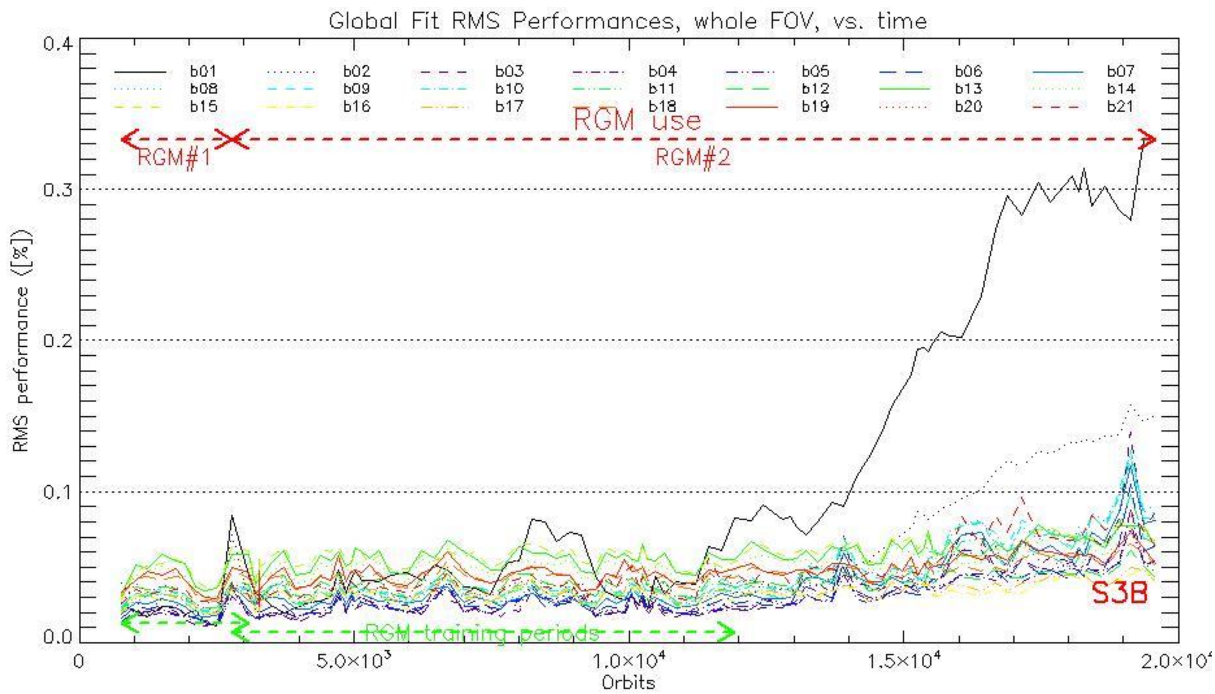

Figure 34: RMS performance of the OLCI-B Gain Model of the previous processing baseline as a function of orbit (please note the different vertical scale with respect to Figure 33).

The overall instrument evolution since channel programming change (18/06/2018) is shown on Figure 35.

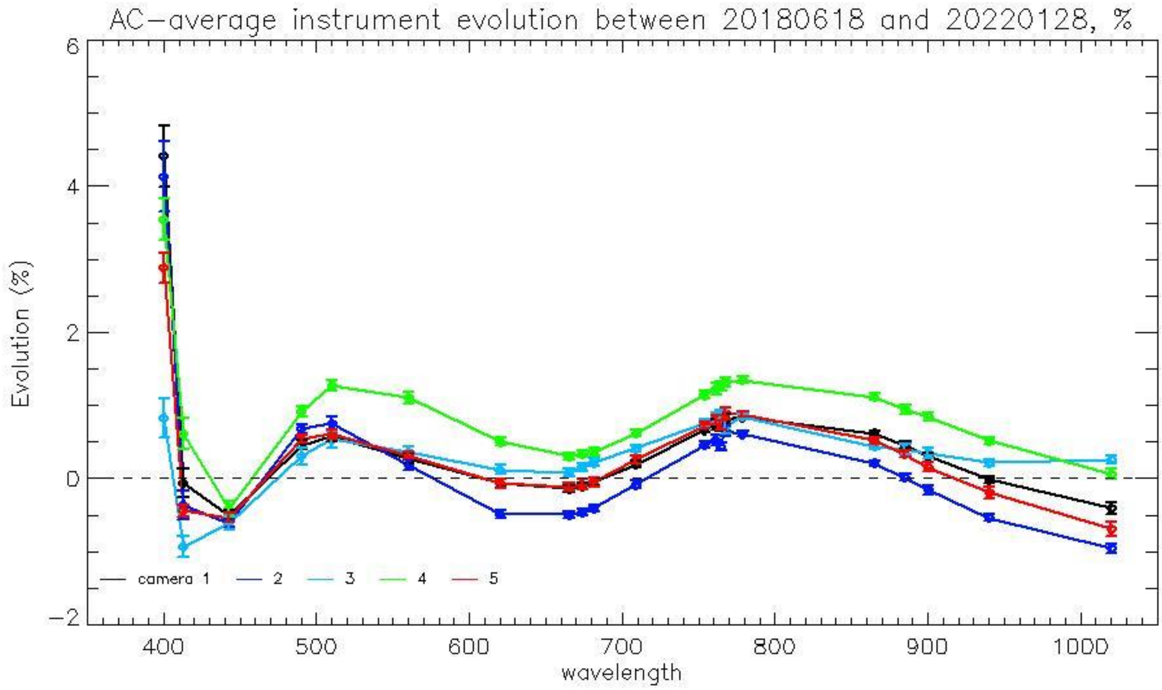

Figure 35: OLCI-B Camera-averaged instrument evolution since channel programming change (18/06/2018) and up to most recent calibration (28/01/2022) versus wavelength.

The overall per camera performance, as a function of wavelength, and at each orbit is shown on Figure 36 as the average and standard deviation of the model over data ratio.

Finally, Figure 37 to Figure 39 show the detail of the model performance, with across-track plots of the model over data ratios at each orbit, one plot for each channel.

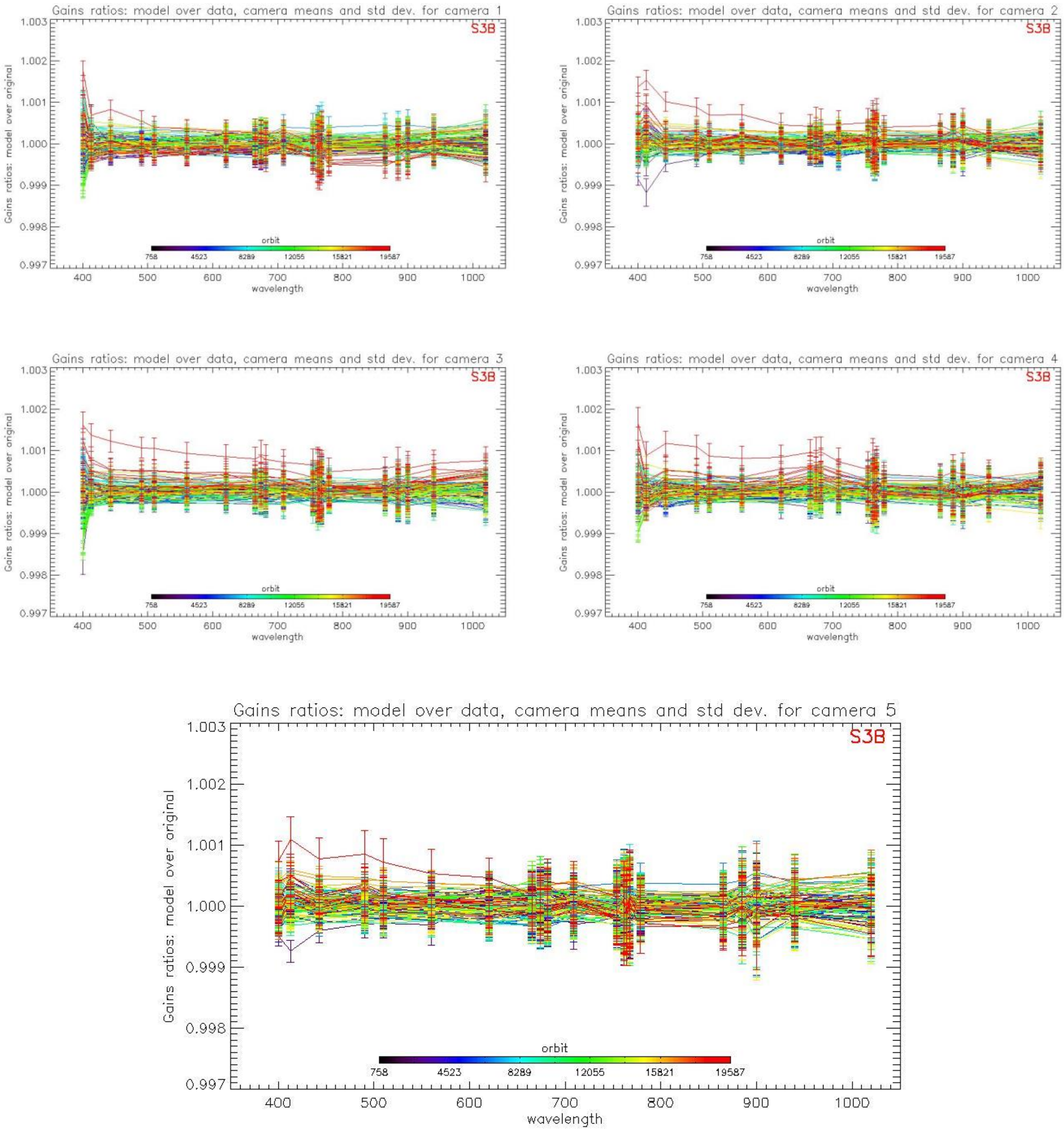

Figure 36: For the 5 cameras: OLCI-B Evolution model performance, as camera-average and standard deviation of ratio of Model over Data vs. wavelength, for each orbit of the test dataset, including 9 calibrations in extrapolation, with a colour code for each calibration from blue (oldest) to red (most recent).

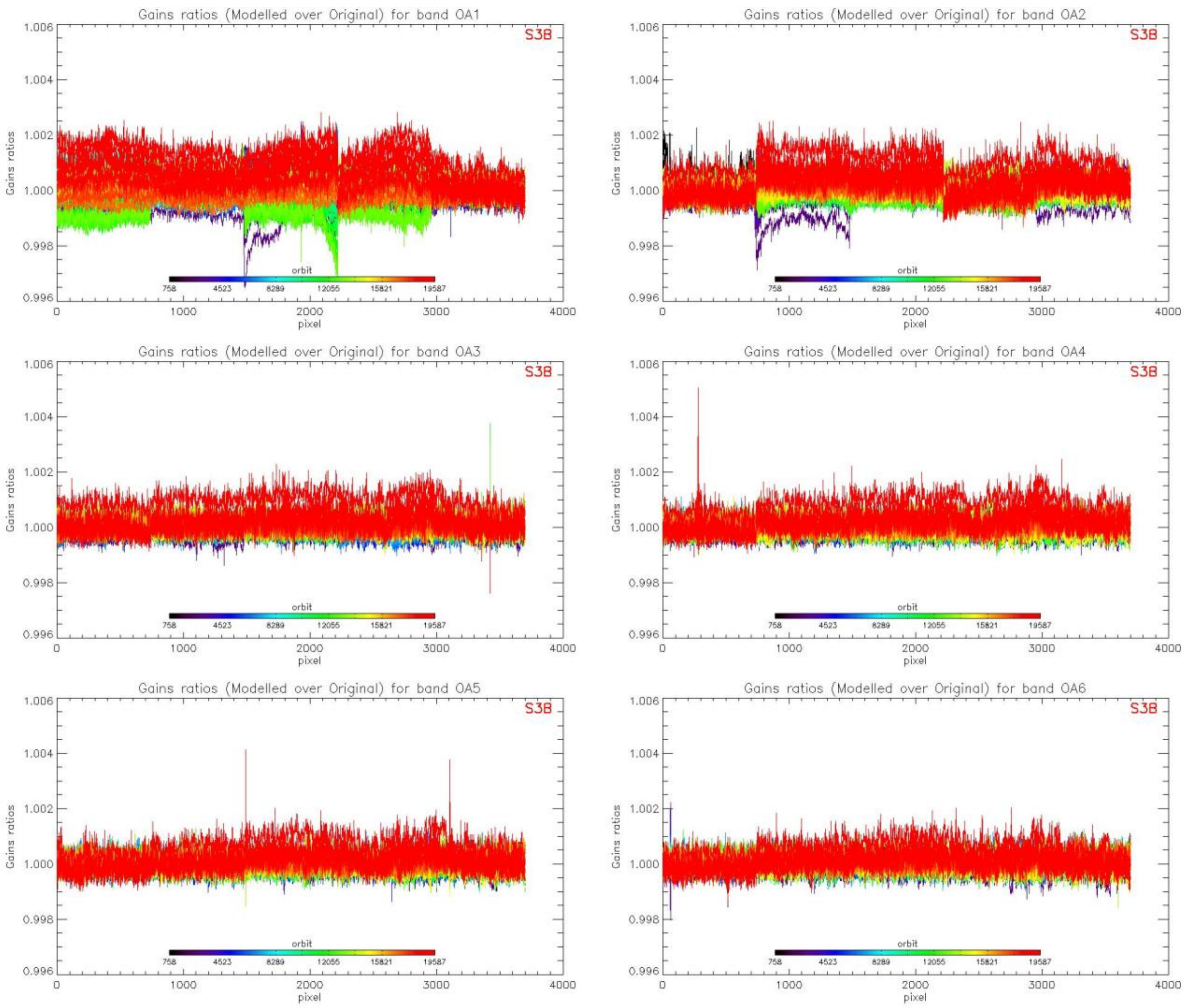

Figure 37: OLCI-B evolution model performance, as ratio of Model over Data vs. pixels, all cameras side by side, over the whole current calibration dataset (since instrument programming update), including 9 calibrations in extrapolation, channels Oa1 to Oa6.

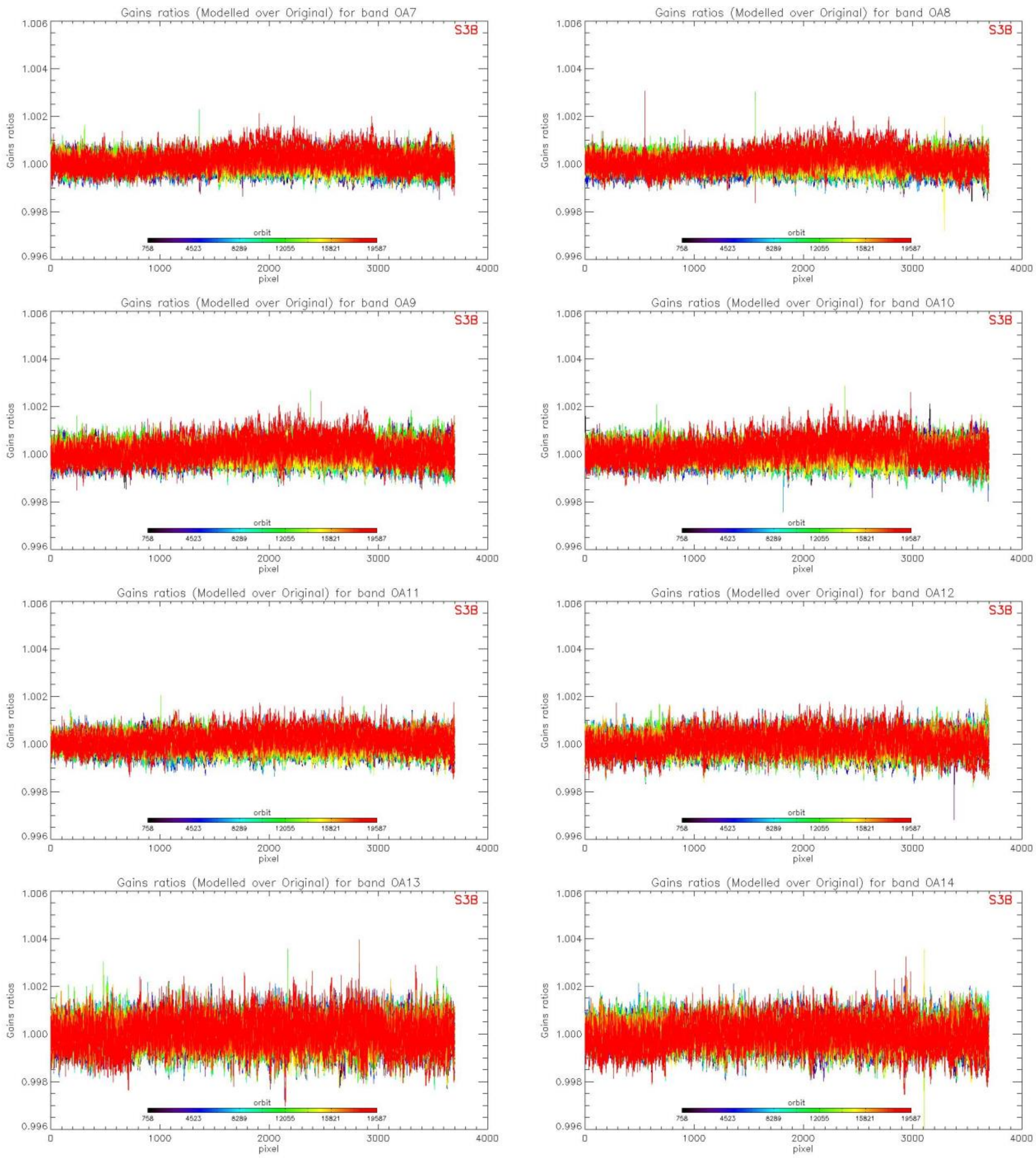

Figure 38: same as Figure 37 for channels Oa7 to Oa14.

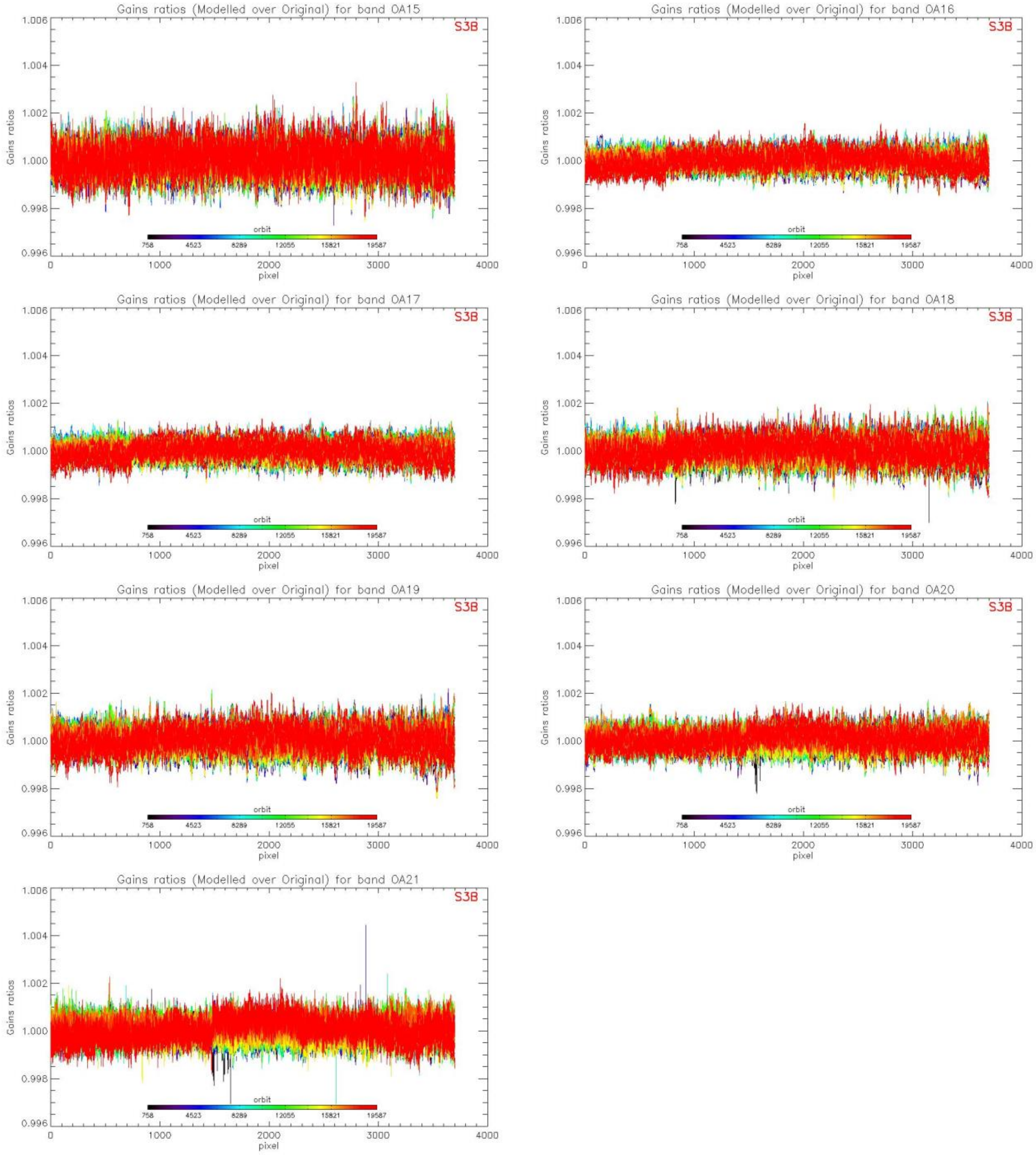

Figure 39: same as Figure 37 for channels Oa15 to Oa21.

2.2.3 Ageing of nominal diffuser [OLCI-L1B-CV-240]

2.2.3.1 OLCI-A

There has been one calibration sequence S05 (reference diffuser) for OLCI-A during the current reported period :

- S05 sequence (diffuser 2) on 27/01/2022 02:00 to 02:02 (absolute orbit 30961)

With the associated S01 sequence (nominal diffuser) in order to compute ageing:

- S01 sequence (diffuser 1) on 27/01/2022 00:19 to 00:21 (absolute orbit 30960)

An other calibration sequence S05 for OLCI-A had been acquired since the last Cyclic Performance Report:

- S05 sequence (diffuser 2) on 23/11/2021 08:29 to 08:31 (absolute orbit 30038)

With the associated S01 sequence (nominal diffuser) in order to compute ageing:

- S01 sequence (diffuser 1) on 23/11/2021 06:48 to 06:50 (absolute orbit 30037)

The diffuser 1 Ageing is computed for each 3700 detector and each spectral band by formula:

Ageing(orb)=G1(orb)/G2(orb)- G1(orb_ref)/G2(orb_ref)

Where:

- G1 is the diffuser 1 (= nominal diffuser) Gain coefficients
- G2 is the diffuser 2 (= reference diffuser) Gain coefficients
- orb_ref is a reference orbit chosen at the beginning of the mission

Ageing is represented in Figure 40 for band Oa01 and in Figure 41 for band Oa17. The negative shift of the sequence at orbit 5832 (for which a slight increase would be expected instead) is not explained so far and still under investigation. It should be noted that the corresponding orbit of diffuser 1 (nominal) has also been detected as an outlier in the modelling of the radiometric long-term trend with an unexpected excess of brightness.

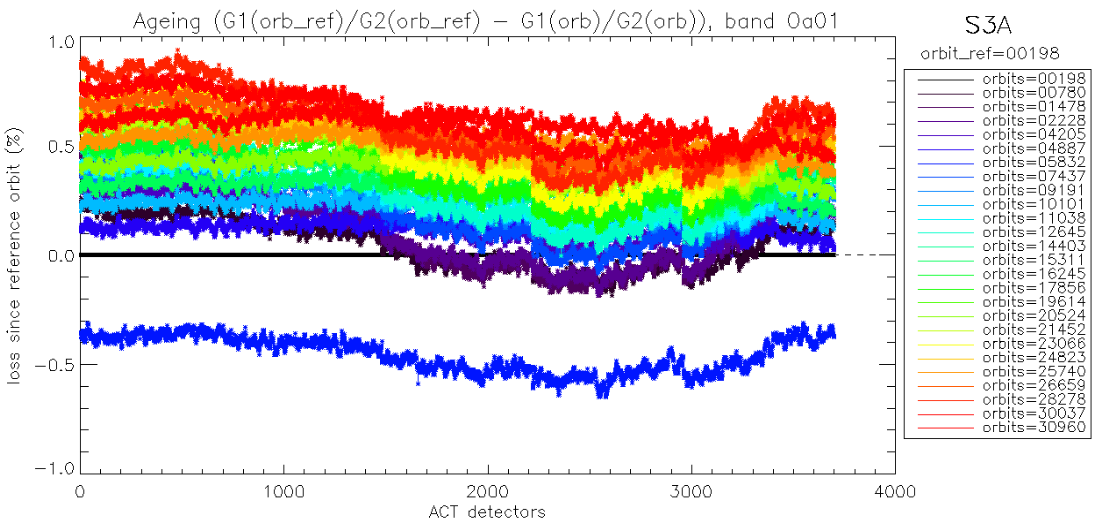

Figure 40: diffuser 1 ageing for spectral band Oa01. We see strong ACT low frequency structures that are due to residual of BRDF modelling.

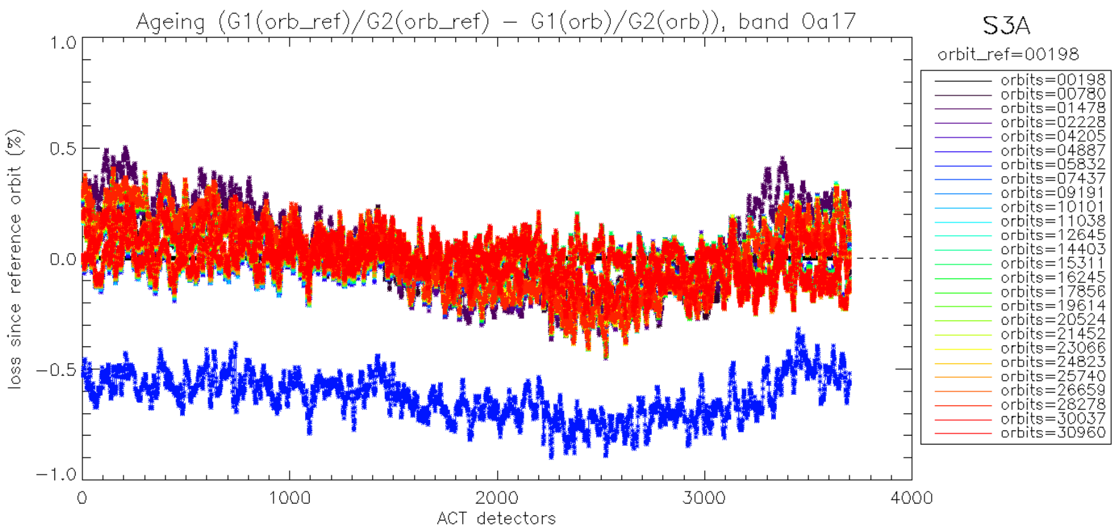

Figure 41: same as Figure 40 for spectral band Oa17. We use this band in order to normalize other bands and remove the ACT structures due to residual of BRDF modelling. Normalized curve for spectral band Oa01 is presented in Figure 42.

Figure 40 and Figure 41 show that the Ageing curves are impacted by a strong ACT pattern which is due to residuals of the bad modelling (on-ground) of the diffuser BRDF. This pattern is dependant of the azimuth angle. It is a 'white' pattern which means it is the same for all spectral bands. As such, we can remove this pattern by normalizing the ageing of all bands by the curve of band Oa17 which is expected not to be impacted by ageing because in the red part of the spectrum. We use an ACT smoothed version (window of 100 detectors) of band Oa17 in order to reduce the high frequency noise. Normalized ageing for spectral band Oa01 is represented in Figure 42 where we can see that this band is impacted by ageing of the diffuser.

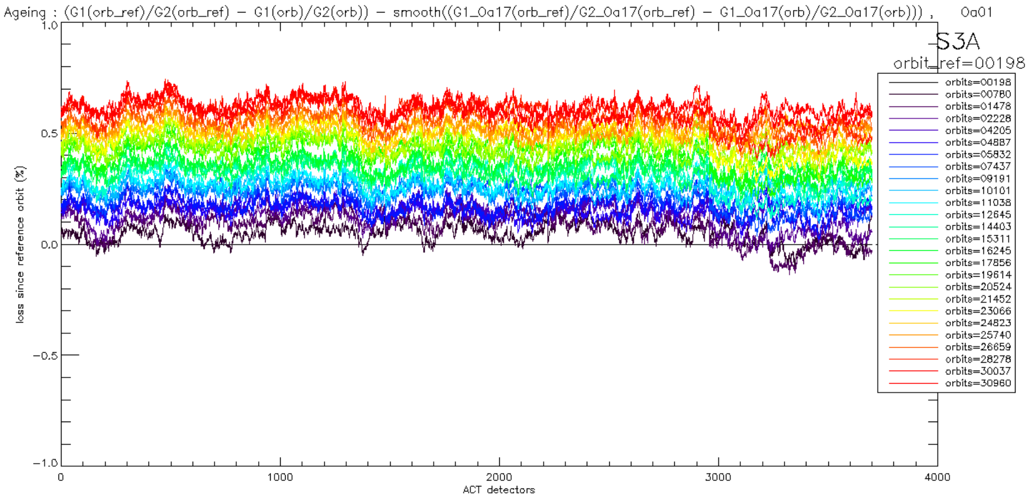

Figure 42: same as Figure 40 after normalization by band Oa17. Ageing of the diffuser 1 is now visible in the 5 cameras.

Camera averaged ageing (normalized by band Oa17) as a function of wavelength is represented in Figure 43 where we can see that ageing is stronger in the 'bluest' spectral bands (short wavelengths). Ageing is clearly visible only for the 6 first spectral bands so far in the OLCI mission life.

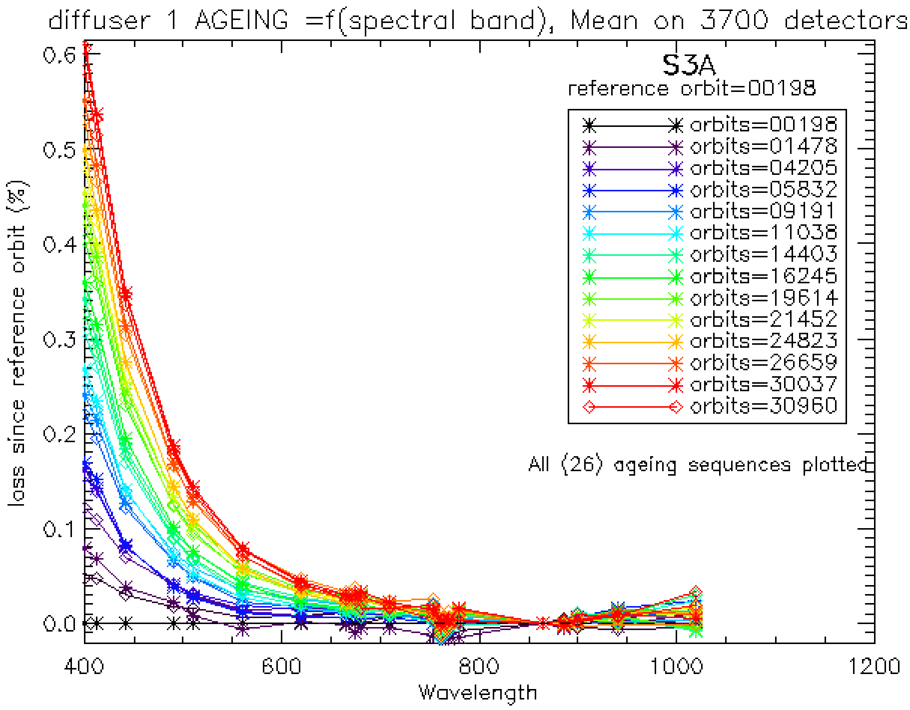

Figure 43: Diffuser 1 ageing as a function of wavelength (or spectral band). Ageing is clearly visible in spectral band #1 to #6. Note that all ageing sequences are plotted but in order to fit in the figure the box legend only displays 1 ageing sequence over 2 (including the most recent one).

Figure 44 shows the evolution, for spectral band Oa01, of the 5 cameras averaged ageing as a function of time.

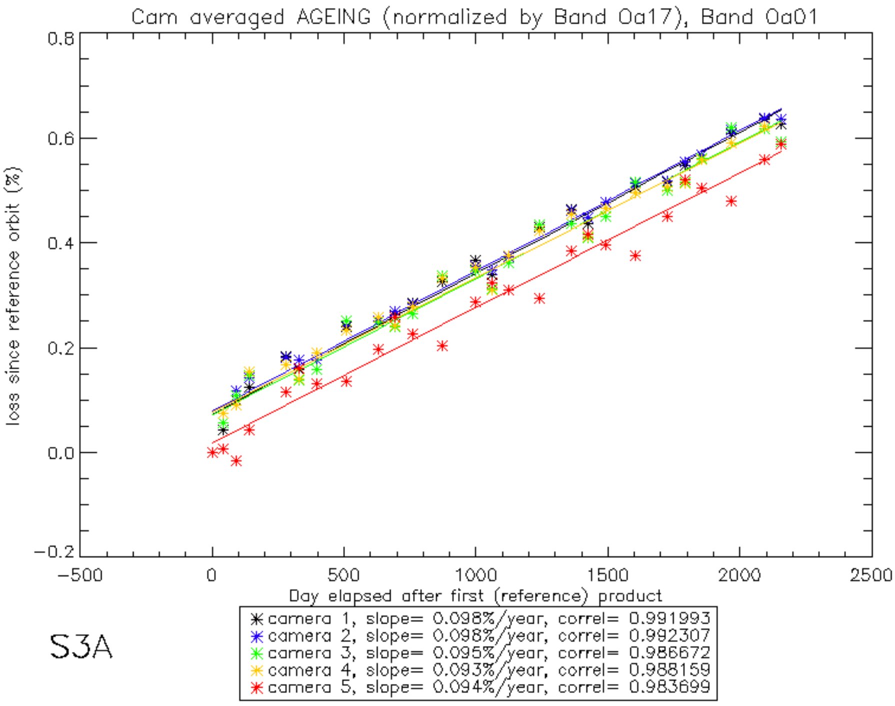

Figure 44: Camera averaged ageing for band Oa01 (normalized by band Oa17) as a function of elapsed time. Linear fit for each camera is plotted. The slope (% loss per year) and the correlation coefficient.

A model of diffuser ageing as a function of cumulated exposure time (i.e. number of acquisition sequence on nominal diffuser, regardless of the band setting) has been built and is described in Cyclic #23 Report. The results of this model confirm the need to model ageing against cumulated exposure rather than elapsed time, as it provides a more linear trend, even if not perfect (see Figure 21 of Cyclic #23 Report).

The slope of this ageing model (% of loss per exposure) as a function of wavelength is presented in Figure 45).

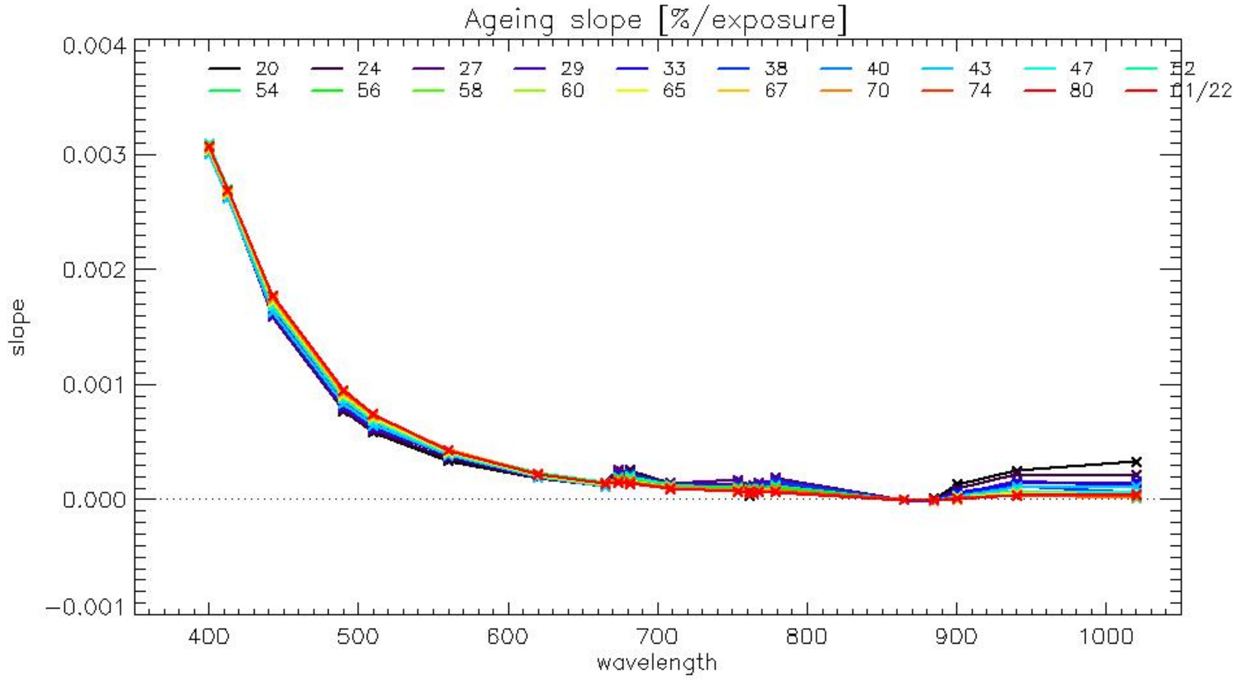

Figure 45: Slope of ageing fit (% of loss per exposure) vs wavelengths, using all the available ageing sequence at the time of the current cycle (red curve) and at the time of previous cycle for which an ageing sequence was measured (see legend within the figure).

In Figure 45, we see that the Ageing slopes have not significantly changed between the current reporting period and the last 19 reporting periods containing a S05 sequence (cycles #80, #74, #70, #67, #65, #60, #56, #58, #54, #52, #47, #43, #40, #38, #33, #29, #27, #24 and #20). Cycle #47 has been used to derive the Ageing Correction model used for the currently operational Gain Model. The exposure time dependent ageing model is used to derive the Gain Model, the most recent version of which has been put in operations in PDGS on 18th November 2021 (Processing Baseline 3.01).

2.2.3.2 OLCI-B

There has been one calibration sequence S05 (reference diffuser) for OLCI-B during acquisition Cycle 63:

- S05 sequence (diffuser 2) on 28/01/2022 12:41 to 12:43 (absolute orbit 19588)

with the associated S01 sequence in order to compute ageing:

- S01 sequence (diffuser 1) on 28/01/2022 11:00 to 11:08 (absolute orbit 19587)

An other calibration sequence S05 for OLCI-B had been acquired since the last Cyclic Performance Report:

- S05 sequence (diffuser 2) on 24/11/2021 09:05 to 09:07 (absolute orbit 18659)

With the associated S01 sequence (nominal diffuser) in order to compute ageing:

- S01 sequence (diffuser 1) on 24/11/2021 07:24 to 07:26 (absolute orbit 18658)

The diffuser 1 Ageing is computed for each 3700 detector and each spectral band by formula:

Ageing(orb)=G1(orb)/G2(orb)- G1(orb_ref)/G2(orb_ref)

Where:

- G1 is the diffuser 1 (= nominal diffuser) Gain coefficients
- G2 is the diffuser 2 (= reference diffuser) Gain coefficients
- orb_ref is a reference orbit chosen at the beginning of the mission

Ageing is represented in Figure 46 for band Oa01 and in Figure 47 for band Oa17.

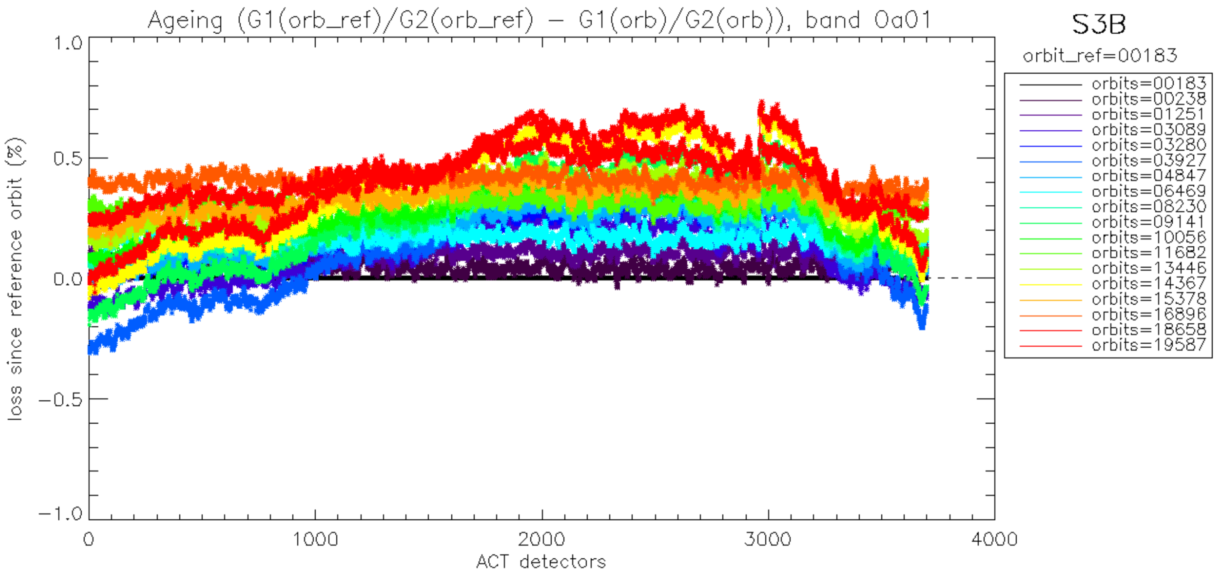

Figure 46: OLCI-B diffuser 1 ageing for spectral band Oa01. We see strong ACT low frequency structures that are due to residual of BRDF modelling.

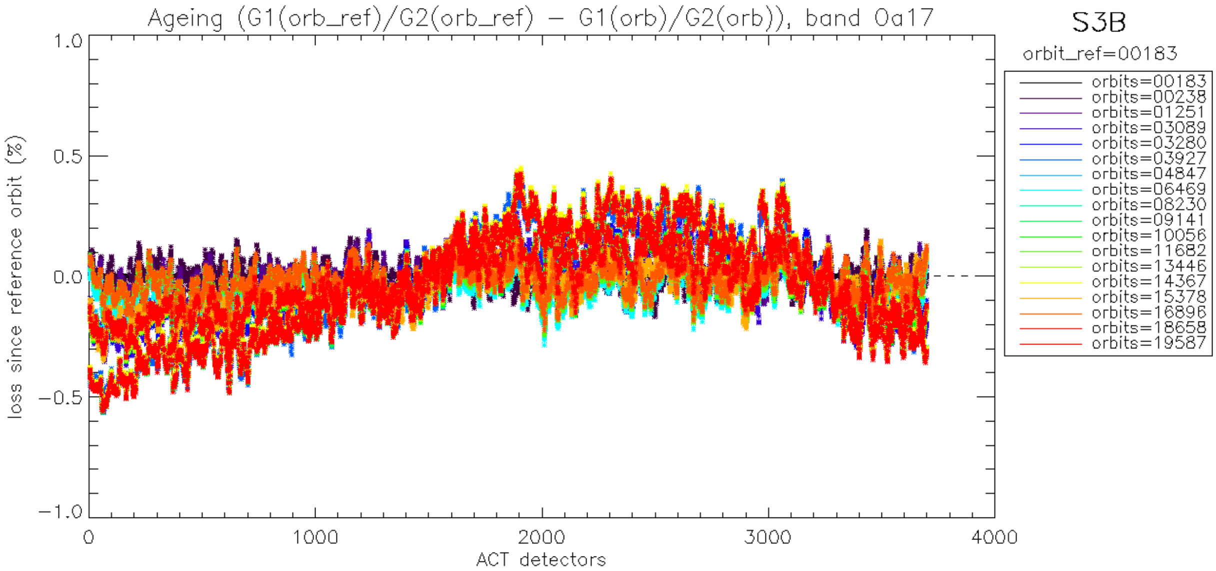

Figure 47: same as Figure 46 for spectral band Oa17. We use this band in order to normalize other bands and remove the ACT structures due to residual of BRDF modelling. Normalized curve for spectral band Oa01 is presented in Figure 48.

Figure 46 and Figure 47 show that the Ageing curves are impacted by a strong ACT pattern which is due to residuals of the bad modelling (on-ground) of the diffuser BRDF. This pattern is dependant of the azimuth angle. It is a 'white' pattern which means it is the same for all spectral bands. As such, we can remove this pattern by normalizing the ageing of all bands by the curve of band Oa17 which is expected not to be impacted by ageing because in the red part of the spectrum. We use an ACT smoothed version (window of 100 detectors) of band Oa17 in order to reduce the high frequency noise. Normalized ageing for spectral band Oa01 is represented in Figure 48 where we can see that this band is impacted by ageing of the diffuser.

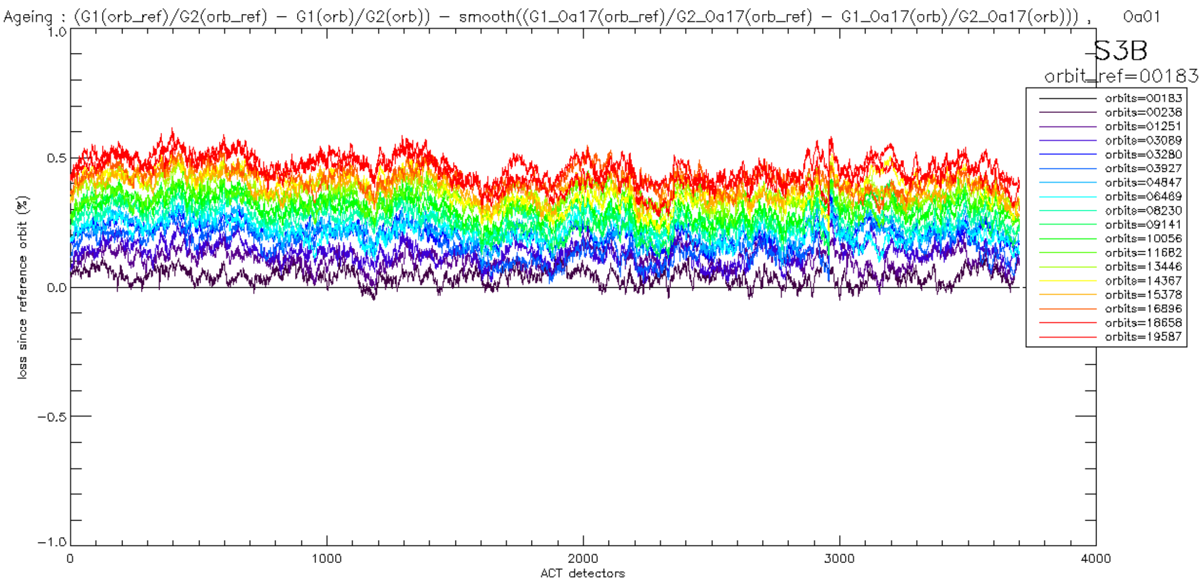

Figure 48: same as Figure 46 after normalization by band Oa17. Ageing of the diffuser 1 is now visible in the 5 cameras.

Camera averaged ageing (normalized by band Oa17) as a function of wavelength is represented in Figure 49 where we can see that ageing is stronger in the 'bluest' spectral bands (short wavelengths). Ageing is clearly visible only for the 5 first spectral bands so far in the OLCI-B mission life. We see a bump around 680 nm which is probably due to characterisation errors that are strongly geometry dependant and affect differently the various camera. This behaviour is under investigation.

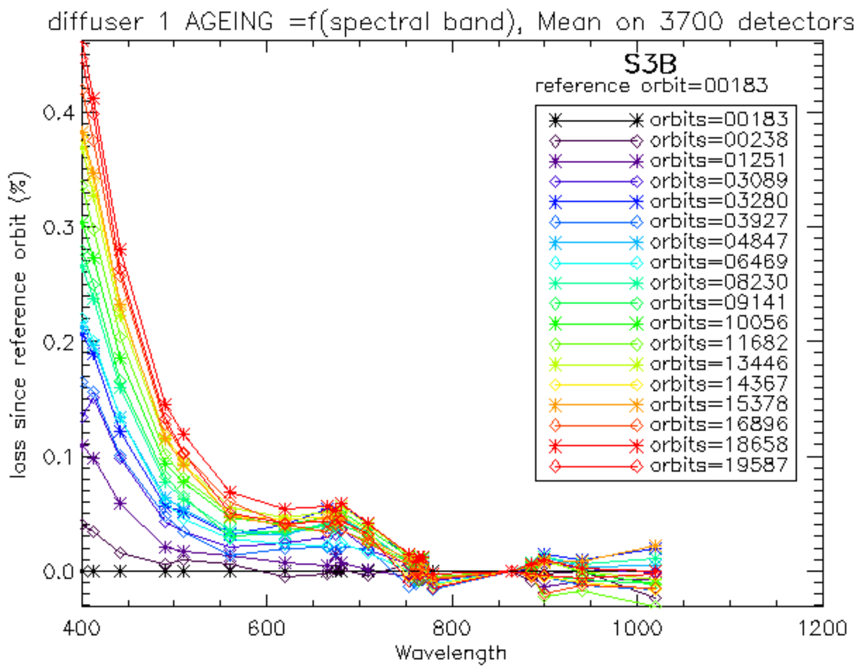

Figure 49: OLCI-B Diffuser 1 ageing as a function of wavelength (or spectral band). Ageing is clearly visible in spectral band #1 to #5.

As for OLCI-A, the OLCI-B Diffuser Ageing has been modelled as a function of cumulated exposure time (i.e. number of acquisition sequence on nominal diffuser, regardless of the band setting). The OLCI-A modelling methodology has been applied to OLCI-B. The results of this modelling, iterated at each new Ageing Sequence acquisition, expressed as the rate of ageing (% of loss per exposure) as a function of wavelength is presented in Figure 50.

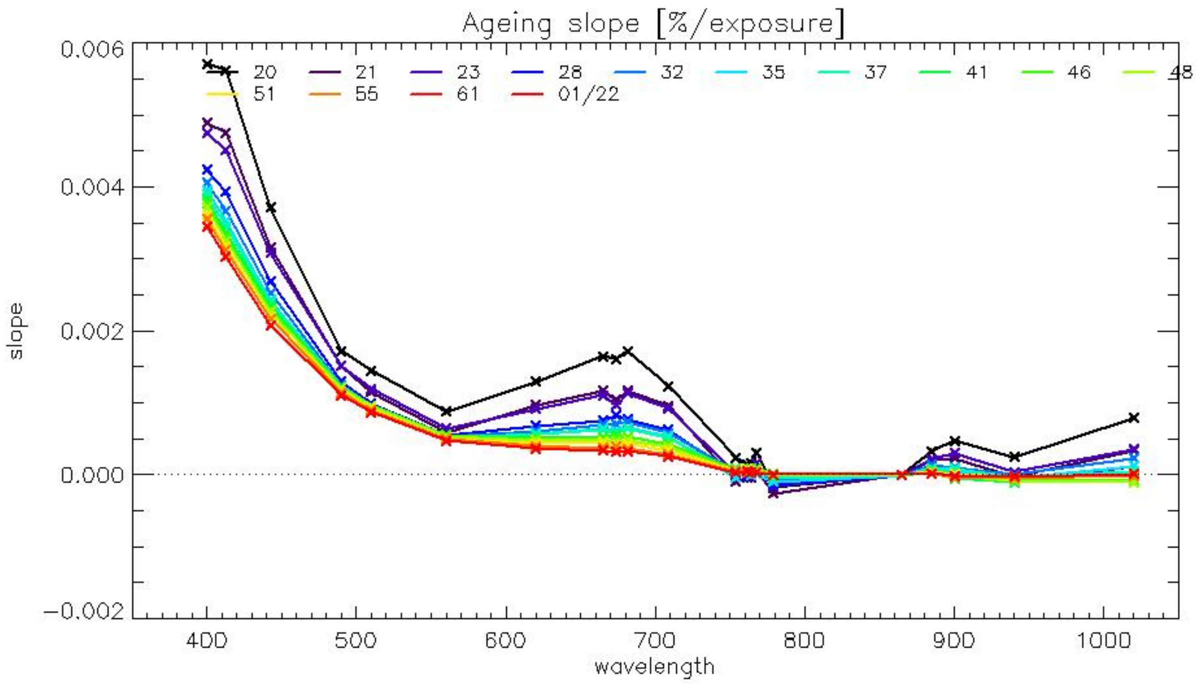

Figure 50: Slope of ageing fit (% of loss per exposure) vs wavelengths, using all the available ageing sequence at the time of the current cycle (red curve) and at the time of previous cycle for which an ageing sequence was measured (see legend within the figure).

The general behaviour of the ageing assessment strongly differ to that of OLCI-A (Figure 45) in two ways: variability with time is much higher and the spectral shape is not as expected. This is interpreted as an unexpected dependency of the *ratio* of diffusers BRDF with illumination conditions. This justified the used of an alternative method using direct comparisons of two nominal diffuser observations, acquired under the same geometry (i.e. directly comparable) and the same day (i.e. with no significant instrument sensitivity evolution) but separated by 7 more exposures to light (during the Yaw Manoeuvres dedicated to the in-flight BRDF modelling). This is in theory the best ageing measurement but as composed of only one measure, it is subject to a large uncertainty. At the time it was derived, it showed a reliable spectral shape up to 850 nm and a good agreement with the nominal assessment in the blue (Figure 51), so that it was used until recently to derive the Radiometric Gain Models. It is referred to as the “YM model”.

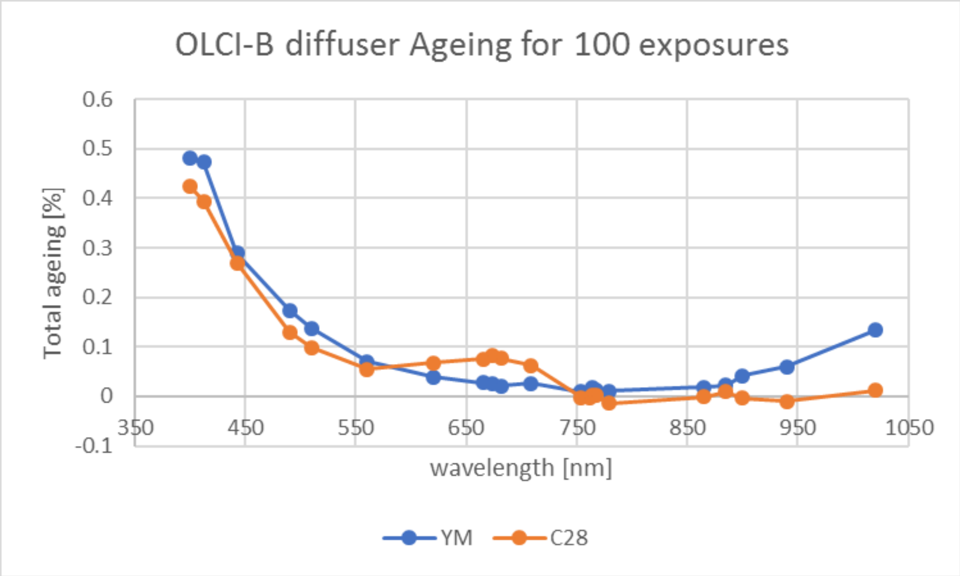

Figure 51: OLCI-B diffuser ageing (after 100 exposures, i.e. about two years) according to direct assessment from Yaw Manoeuvres (blue) and nominal method at Cycle 28 (orange).

The regular decrease of the ageing slopes according to the nominal method makes YM ageing model more and more overestimated, and a new method has been explored.

As the anomalous ageing estimated in the red have shown to be correlated with Sun illumination geometry, a reanalysis of the Ageing sequences has been done on sub-sets of sequences with equal or close illumination conditions. Once sorted by Sun azimuth angles, a set of 3 clusters (Figure 52) provide independent ageing estimates. The estimates quality can be inferred from in-FOV consistency, both inside each camera and between cameras, as the diffuser ageing is independent of the viewing direction. The final estimate is a weighted average of the clusters assessments.

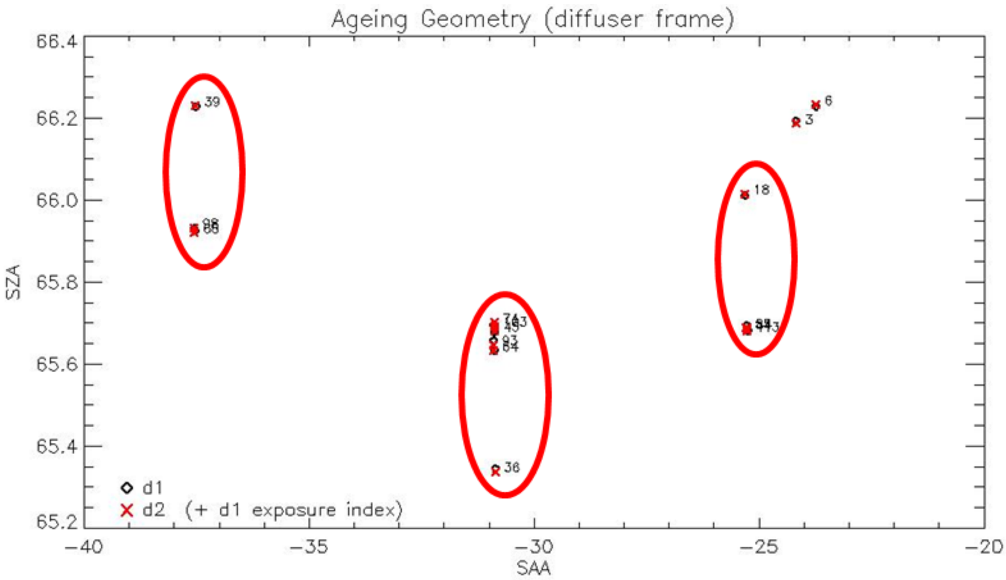

Figure 52: clustered Ageing sequences illumination geometries.

The results are quite satisfactory with good in-FOV consistency, well improved with respect to other methods, and a rather good inter-cluster consistency. The final results, together with those of the two other methods are shown on Figure 53.

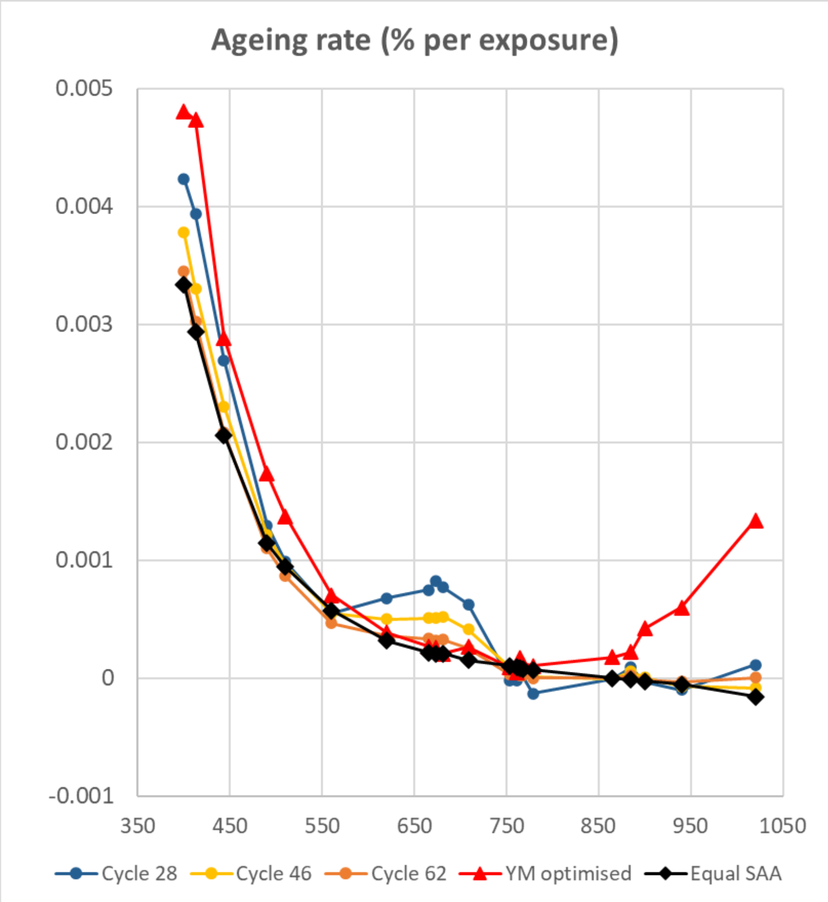

Figure 53: various estimates of the ageing rate, according to nominal method for cycles 28, 46 and 62, according to direct assessment during Yaw manoeuvres, and according to the Equal SAA clustering.

This new "Equal SAA" ageing model has been used to derive the most recent radiometric Gain Model, put in operations in PDGS on 18 November 2021 (Processing Baseline 3.01).

2.2.4 Updating of calibration ADF [OLCI-L1B-CV-260]

2.2.4.1.1 OLCI-A

No CAL_AX ADF has been delivered to PDGS during the report period for OLCI-A.

2.2.4.1.2 OLCI-B

No CAL_AX ADF has been delivered to PDGS during the report period for OLCI-B.

2.3 Spectral Calibration [OLCI-L1B-CV-400]

2.3.1 OLCI-A

There has been no S02+S03 Spectral Calibration for OLCI-A in the reporting period.

Consequently, the last spectral calibration results, presented in CPR #78/#59, remain valid.

2.3.2 OLCI-B

There has been no S02+S03 Spectral Calibration for OLCI-B in the reporting period.

Consequently, the last spectral calibration results, presented in CPR #78/#59, remain valid.

2.4 Signal to Noise assessment [OLCI-L1B-CV-620]

2.4.1 SNR from Radiometric calibration data

2.4.1.1 OLCI-A

SNR computed for all calibration data (S01, S04 and S05 sequences) as a function of band number is presented in

Figure 54.

SNR computed for all calibration data as a function of orbit number for band Oa01 (the less stable band) is presented in Figure 55.

There is no significant evolution of this parameter during the current cycle and the ESA requirement is fulfilled for all bands.

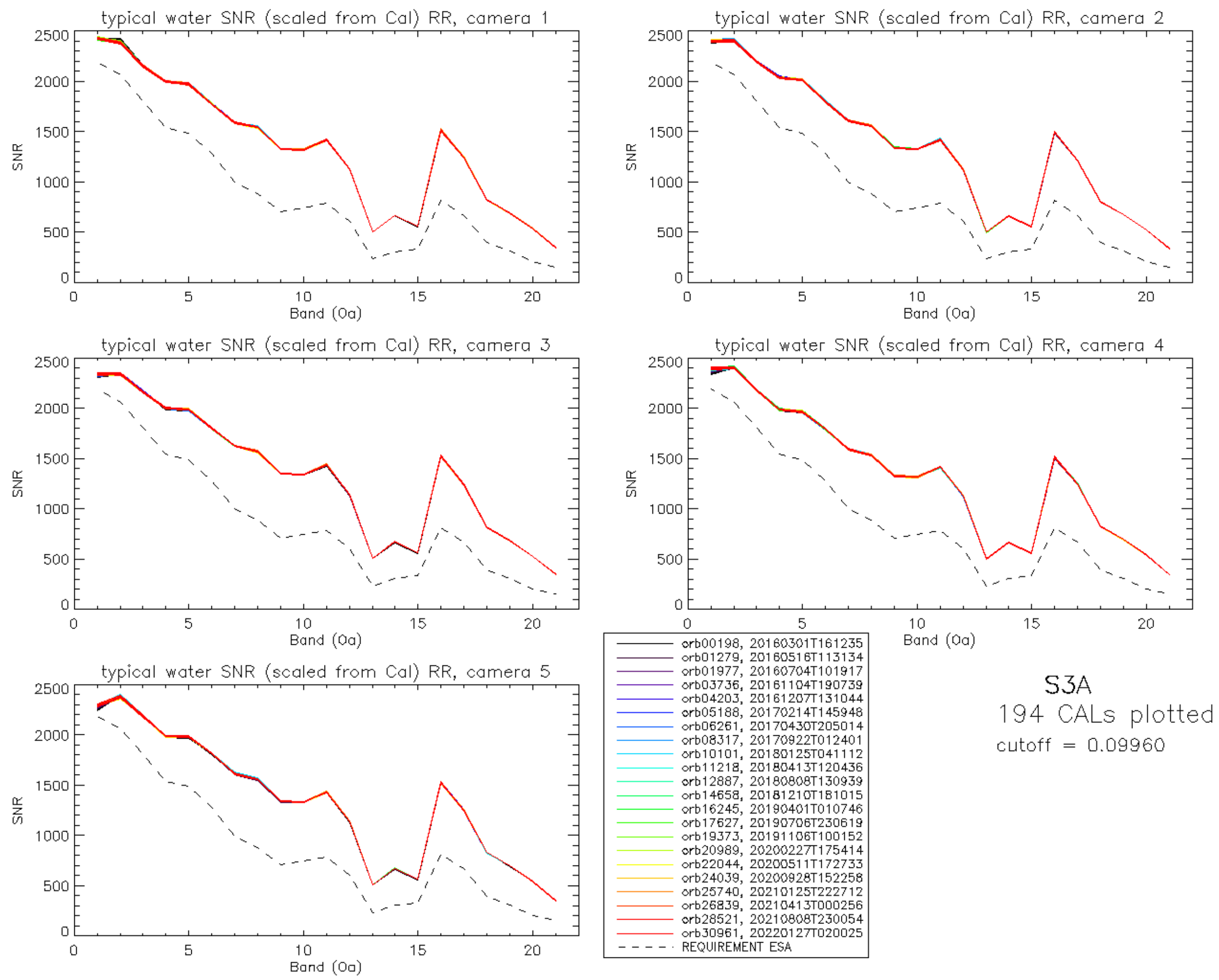

Figure 54: OLCI-A Signal to Noise ratio as a function of the spectral band for the 5 cameras. These results have been computed from radiometric calibration data. All calibrations except first one (orbit 183) are presents with the colours corresponding to the orbit number (see legend). The SNR is very stable with time: the curves for all orbits are almost superimposed. The dashed curve is the ESA requirement.

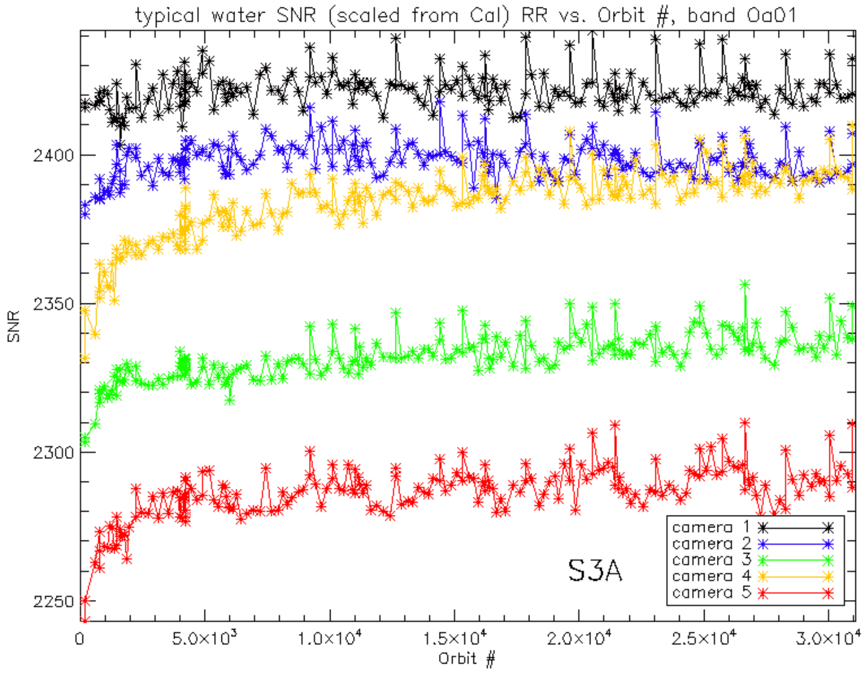

Figure 55: long-term stability of the SNR estimates from Calibration data, example of channel Oa1.

The mission averaged SNR figures are provided in Table 1 below, together with their radiance reference level. According to the OLCI SNR requirements, these figures are valid at these radiance levels and at Reduced Resolution (RR, 1.2 km). They can be scaled to other radiance levels assuming shot noise (CCD sensor noise) is the dominating term, i.e. radiometric noise can be considered Gaussian with its standard deviation varying as the square root of the signal; in other words: $SNR(L) = SNR(L_{ref}) \cdot \sqrt{\frac{L}{L_{ref}}}$. Following the same assumption, values at Full Resolution (300m) can be derived from RR ones as 4 times smaller.

Table 1: OLCI-A SNR figures as derived from Radiometric Calibration data. Figures are given for each camera (time average and standard deviation), and for the whole instrument. The requirement and its reference radiance level are recalled (in mW.sr^{-1}.m^{-2}.nm^{-1}).

	L_{ref}	SNR	C1		C2		C3		C4		C5		All	
nm	LU	RQT	avg	*std*	avg	*std*	avg	*std*	avg	*std*	avg	*std*	avg	*std*
400.000	63.0	2188	2421	6.2	2398	6.2	2332	7.9	2383	12.0	2286	9.3	2364	7.0
412.000	74.1	2061	2388	9.3	2404	6.8	2339	4.9	2401	5.0	2380	9.0	2382	5.5
442.000	65.6	1811	2158	5.9	2196	6.0	2163	4.9	2185	4.1	2194	5.7	2179	4.0
490.000	51.2	1541	2000	4.6	2036	4.9	1998	4.2	1984	4.4	1988	4.5	2001	3.2
510.000	44.4	1488	1979	5.3	2014	4.9	1986	4.5	1967	4.4	1985	4.3	1986	3.5
560.000	31.5	1280	1775	4.5	1802	4.1	1803	4.7	1794	3.8	1818	3.3	1799	3.0
620.000	21.1	997	1591	4.1	1608	4.3	1624	3.1	1593	3.2	1615	3.5	1606	2.6
665.000	16.4	883	1546	4.1	1557	4.4	1567	3.9	1533	3.5	1561	3.7	1553	3.0
674.000	15.7	707	1328	3.4	1337	3.7	1350	2.8	1323	3.2	1343	3.5	1336	2.4
681.000	15.1	745	1319	3.6	1326	3.1	1338	2.7	1314	2.5	1334	3.4	1326	2.1
709.000	12.7	785	1420	4.2	1420	4.0	1435	3.3	1414	3.5	1431	3.1	1424	2.7
754.000	10.3	605	1127	3.1	1121	2.8	1136	3.1	1125	2.4	1139	2.7	1130	2.2
761.000	6.1	232	502	1.1	498	1.1	505	1.2	501	1.1	508	1.4	503	0.8
764.000	7.1	305	663	1.6	658	1.5	668	2.0	661	1.5	670	2.1	664	1.3
768.000	7.6	330	558	1.4	554	1.3	563	1.3	557	1.3	564	1.3	559	1.0
779.000	9.2	812	1516	4.7	1498	4.6	1526	5.2	1512	4.9	1527	4.9	1516	4.1
865.000	6.2	666	1244	3.5	1213	3.4	1239	3.8	1246	3.5	1250	2.8	1238	2.8
885.000	6.0	395	823	1.7	801	1.6	814	2.0	824	1.5	831	1.6	819	1.1
900.000	4.7	308	691	1.5	673	1.3	683	1.6	693	1.5	698	1.5	688	1.0
940.000	2.4	203	534	1.2	522	1.2	525	0.9	539	1.1	542	1.3	532	0.7
1020.000	3.9	152	345	0.9	337	0.8	348	0.7	345	0.8	351	0.8	345	0.5

2.4.1.2 OLCI-B

SNR computed for all OLCI-B calibration data (S01, S04 (but not the dark-only S04) and S05 sequences) as a function of band number is presented in Figure 56.

SNR computed for all OLCI-B calibration data as a function of orbit number for band Oa01 (the less stable band) is presented in Figure 57.

As for OLCI-A the SNR is very stable in time. There is no significant evolution of this parameter during the current cycle and the ESA requirement is fulfilled for all bands.

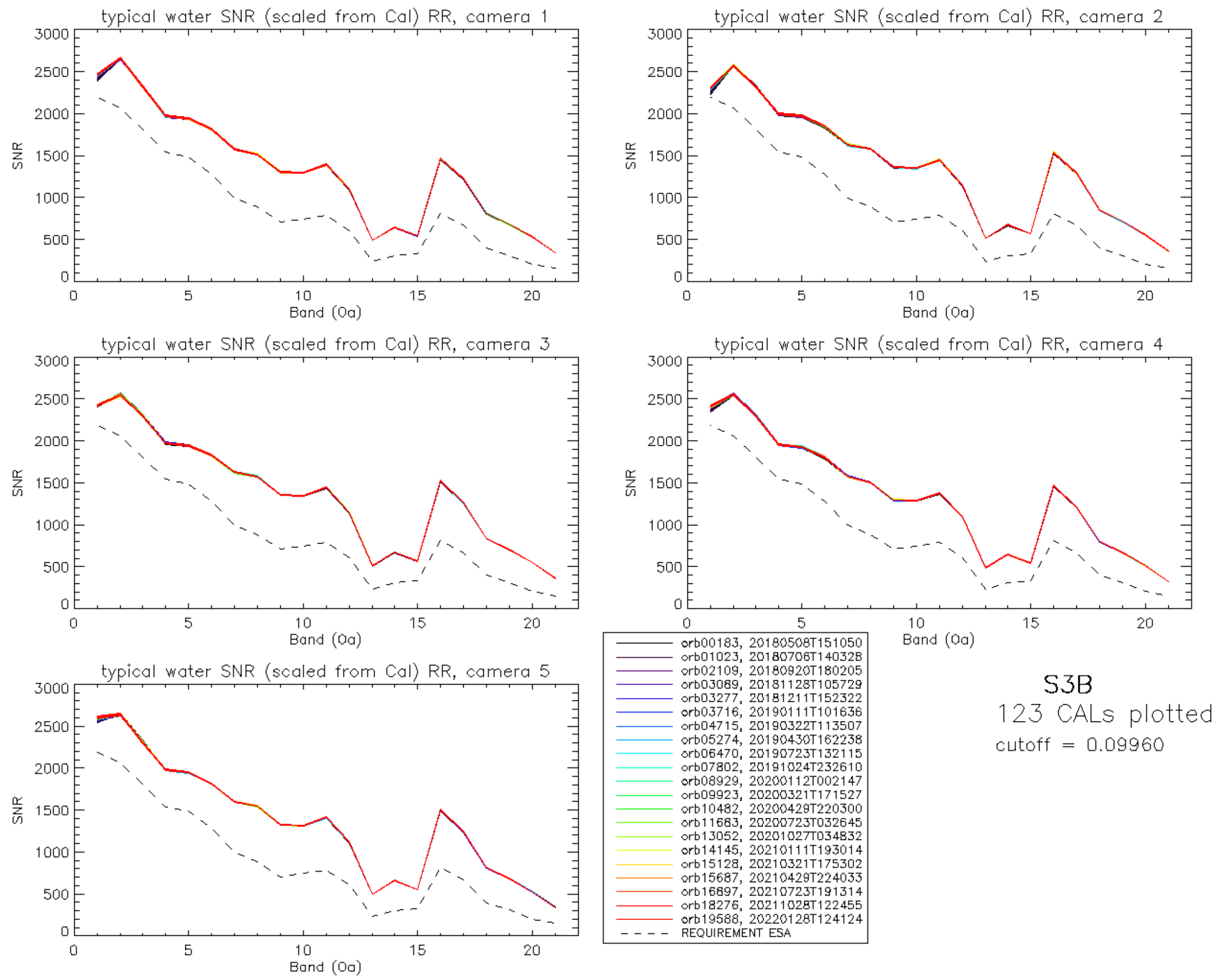

Figure 56: OLCI-B Signal to Noise ratio as a function of the spectral band for the 5 cameras. These results have been computed from radiometric calibration data. All calibrations except first one (orbit 167) are presents with the colours corresponding to the orbit number (see legend). The SNR is very stable with time: the curves for all orbits are almost superimposed. The dashed curve is the ESA requirement.

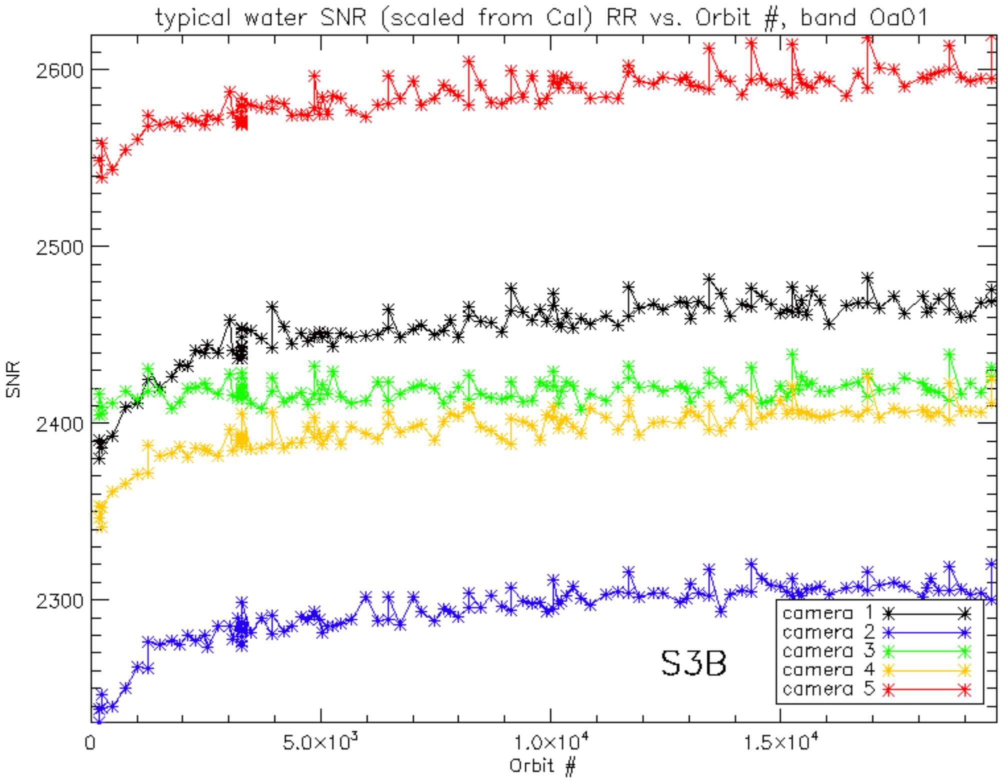

Figure 57: long-term stability of the OLCI-B SNR estimates from Calibration data, example of channel Oa1.

Table 2: OLCI-B SNR figures as derived from Radiometric Calibration data. Figures are given for each camera (time average and standard deviation), and for the whole instrument. The requirement and its reference radiance level are recalled (in mW.sr⁻¹.m⁻².nm⁻¹).

	L_{ref}	SNR	C1		C2		C3		C4		C5		All	
nm	LU	RQT	avg	*std*	avg	*std*	avg	*std*	avg	*std*	avg	*std*	avg	*std*
400.000	63.0	2188	2453	19.3	2293	17.0	2418	6.3	2396	14.0	2585	14.2	2429	13.1
412.000	74.1	2061	2655	6.7	2569	6.1	2545	8.3	2550	6.1	2638	7.1	2591	5.2
442.000	65.6	1811	2324	6.4	2317	5.9	2300	6.3	2303	6.7	2309	6.4	2311	5.3
490.000	51.2	1541	1966	4.8	1989	5.6	1971	4.9	1952	4.6	1979	4.6	1972	3.8
510.000	44.4	1488	1939	4.8	1968	5.9	1943	4.9	1924	5.1	1951	4.8	1945	4.1
560.000	31.5	1280	1813	4.8	1848	5.1	1829	4.6	1804	4.9	1817	4.1	1822	3.7
620.000	21.1	997	1573	4.3	1626	4.6	1625	3.6	1576	3.7	1601	3.2	1600	2.8
665.000	16.4	883	1513	4.2	1579	3.8	1573	3.8	1501	3.0	1547	3.8	1543	2.8
674.000	15.7	707	1301	3.8	1358	3.5	1353	3.2	1292	2.6	1328	3.0	1326	2.3
681.000	15.1	745	1293	3.5	1347	3.2	1343	2.9	1285	2.7	1316	2.9	1317	2.1
709.000	12.7	785	1390	4.1	1447	4.2	1443	4.0	1373	2.9	1412	3.7	1413	3.0
754.000	10.3	605	1096	3.8	1143	3.7	1142	3.5	1089	2.9	1116	3.3	1117	2.9
761.000	6.1	232	487	1.2	509	1.2	509	1.4	485	1.2	498	1.4	498	1.0
764.000	7.1	305	643	1.6	672	2.0	672	1.9	641	1.7	658	1.9	657	1.5
768.000	7.6	330	541	1.5	568	1.5	564	1.4	541	1.4	555	1.6	554	1.1
779.000	9.2	812	1467	4.2	1535	4.7	1527	5.4	1467	4.1	1506	4.5	1501	3.9
865.000	6.2	666	1221	3.6	1287	3.9	1258	3.6	1205	3.6	1238	3.0	1242	2.9
885.000	6.0	395	808	2.3	847	1.9	834	1.9	799	1.7	815	2.1	821	1.5
900.000	4.7	308	679	1.5	714	2.0	704	1.7	670	1.6	683	1.5	690	1.2
940.000	2.4	203	527	1.3	549	1.5	551	1.3	510	1.1	522	1.3	532	0.9
1020.000	3.9	152	336	0.8	358	1.2	358	0.8	318	0.7	338	1.0	342	0.6

2.4.2 SNR from EO data

2.4.2.1 OLCI-A

There has been no update on SNR assessment from EO data during the cycle. Last figures (cycle 9) are considered valid.

2.4.2.2 OLCI-B

The SNR assessment from EO data has not been applied to OLCI-B considering a) that SNR estimates from RC data have been proved more reliable for OLCI-A and b) that it requires a significant amount of human and machine resources that can be more efficiently used for other tasks.

2.5 Geometric Calibration/Validation

2.5.1 OLCI-A

OLCI-A georeferencing performance is compliant since the introduction of MPC Geometric Calibration, put in production on the 14th of March 2018. It has however significantly improved after its last full revision of GCMs (Geometric Calibration Models, or platform to instrument alignment quaternions) and IPPVMs (Instrument Pixels Pointing Vectors) both derived using the GeoCal Tool and put in production on 30/07/2019.

The following figures (Figure 58 to Figure 63) show time series of the overall RMS performance (requirement criterion) and of the across-track and along-track biases for each camera. New plots (Figure 64 and Figure 65) introduce monitoring of the performance homogeneity within the field of view: georeferencing errors in each direction at camera transitions (difference between last pixel of camera N and first pixel of camera N+1) and within a given camera (maximum bias minus minimum inside each camera). The performance improvement since the 30/07/2019 is significant on most figures: the global RMS value decreases form around 0.35 to about 0.2 (Figure 58), the across-track biases decrease significantly for all cameras (Figure 59 to Figure 63), the along-track bias reduces for at least camera 3 (Figure 61) and the field of view homogeneity improves drastically (Figure 64 and Figure 65, but also reduction of the dispersion – distance between the ± 1 sigma lines – in Figure 59 to Figure 63).

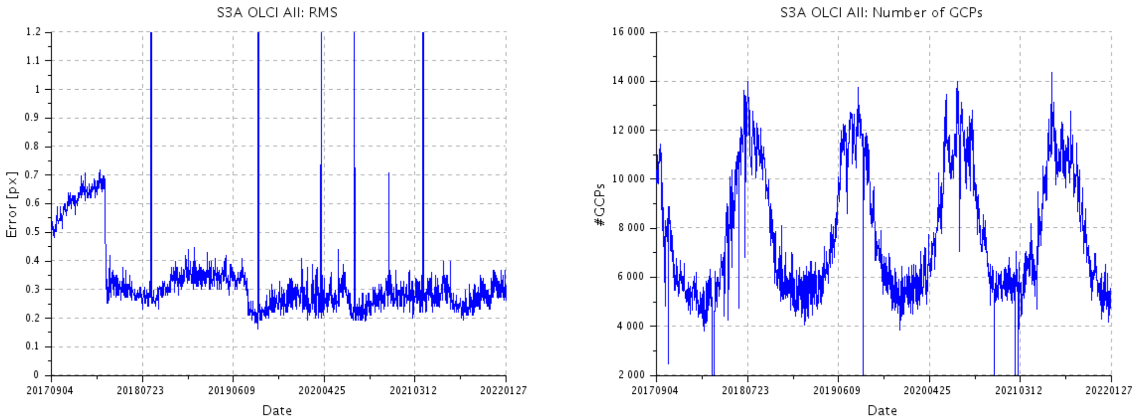

Figure 58: overall OLCI-A georeferencing RMS performance time series (left) and number of validated control points corresponding to the performance time series (right) over the whole monitoring period

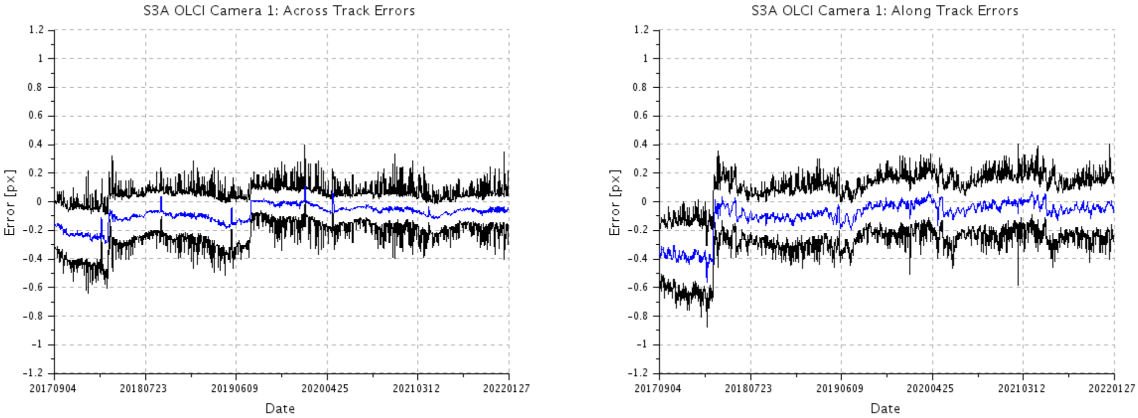

Figure 59: across-track (left) and along-track (right) OLCI-A georeferencing biases time series for Camera 1. Blue line is the average, black lines are average plus and minus 1 sigma.

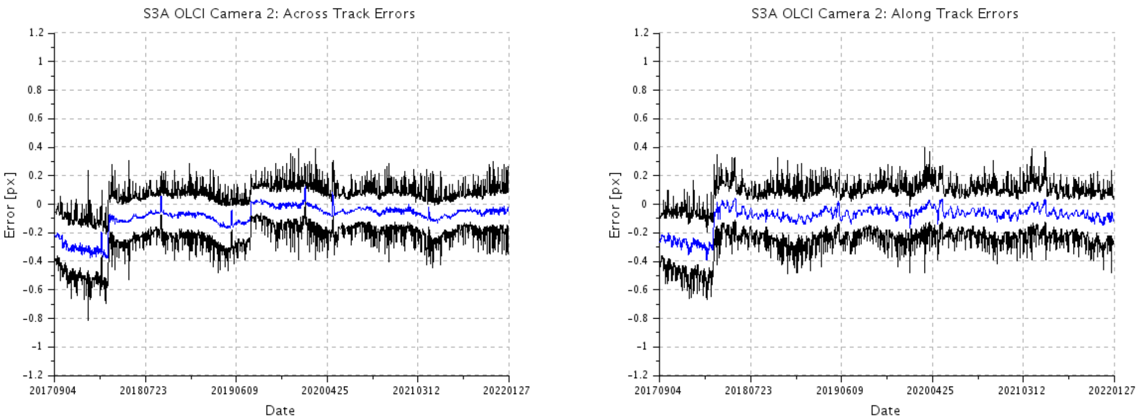

Figure 60: same as Figure 59 for Camera 2.

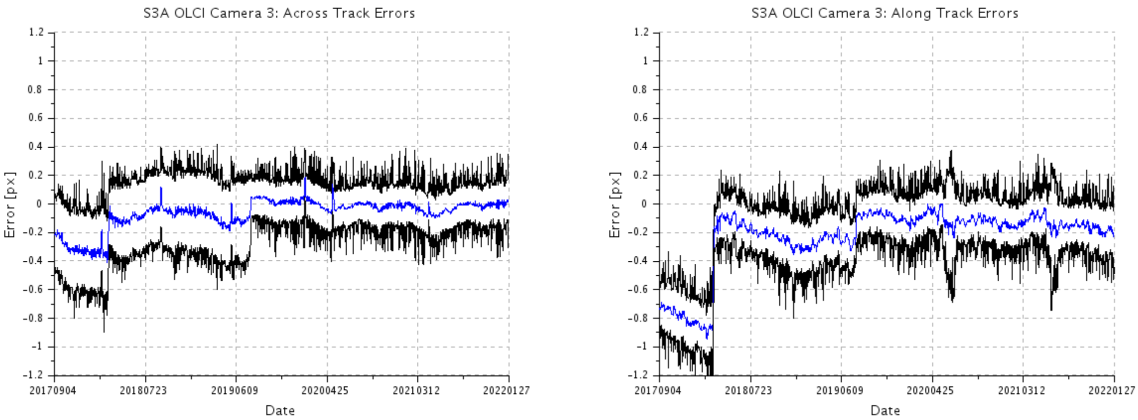

Figure 61: same as Figure 59 for Camera 3.

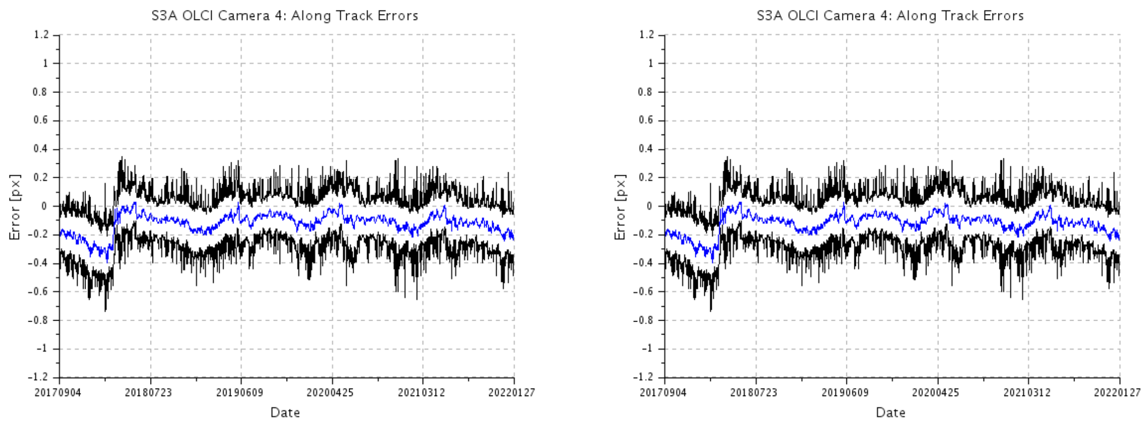

Figure 62: same as Figure 59 for Camera 4.

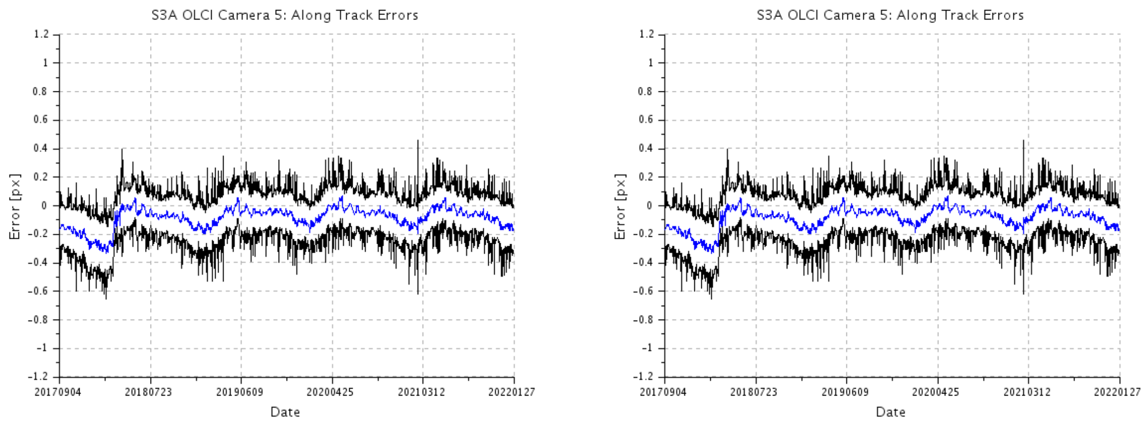

Figure 63: same as Figure 59 for Camera 5.

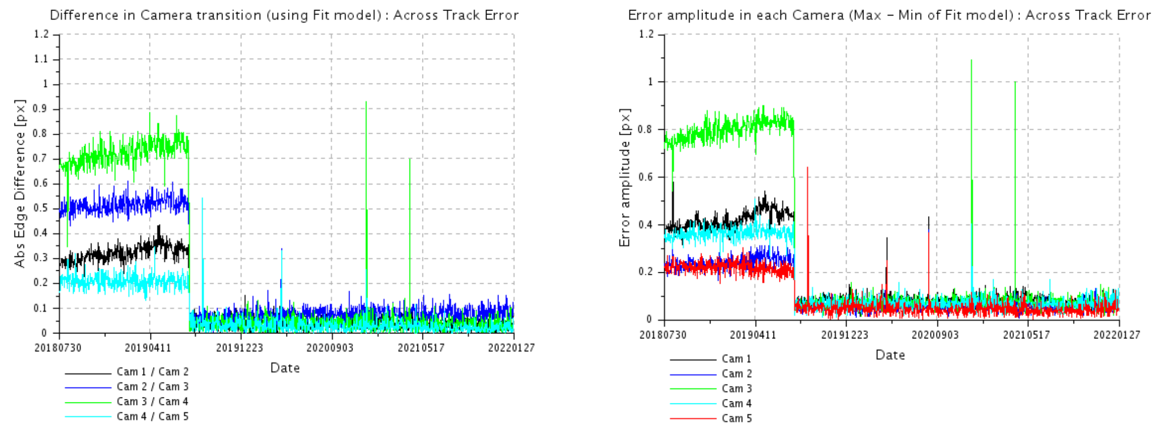

Figure 64: OLCI-A spatial across-track misregistration at each camera transition (left) and maximum amplitude of the across-track error within each camera (left).

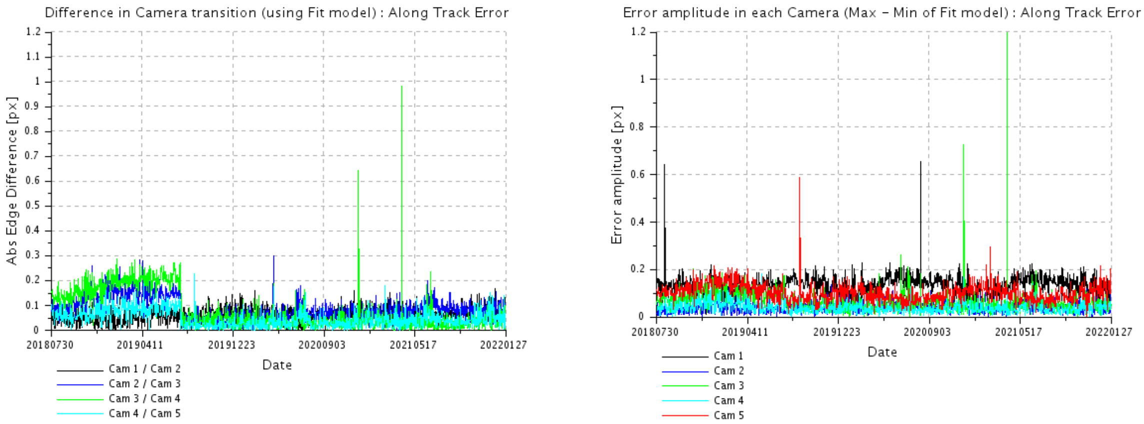

Figure 65: OLCI-A spatial along-track misregistration at each camera transition (left) and maximum amplitude of the along-track error within each camera (left).

2.5.2 OLCI-B

Georeferencing performance of OLCI-B improved significantly with the fourth geometric calibration introduced the 30/07/2019. However, the instrument pointing is still evolving, in particular for camera 2 (Figure 72) and a new geometric calibration has been done and introduced in the processing chain on the 16th of April 2020. Its impact is significant on the along-track biases of all cameras (Figure 67 to Figure 71), but also on the continuity at camera interfaces (Figure 72, left) and on intra-camera homogeneity (Figure 72, right). Since then, further adjustments to the geometric calibration have been introduced, mainly to correct the along-track drifts. The most recent was put in production on 29/07/2021and its effect can be seen e.g. on left graphs of Figure 68, Figure 69 and Figure 71 (across-track biases of cameras 2, 3 & 5).

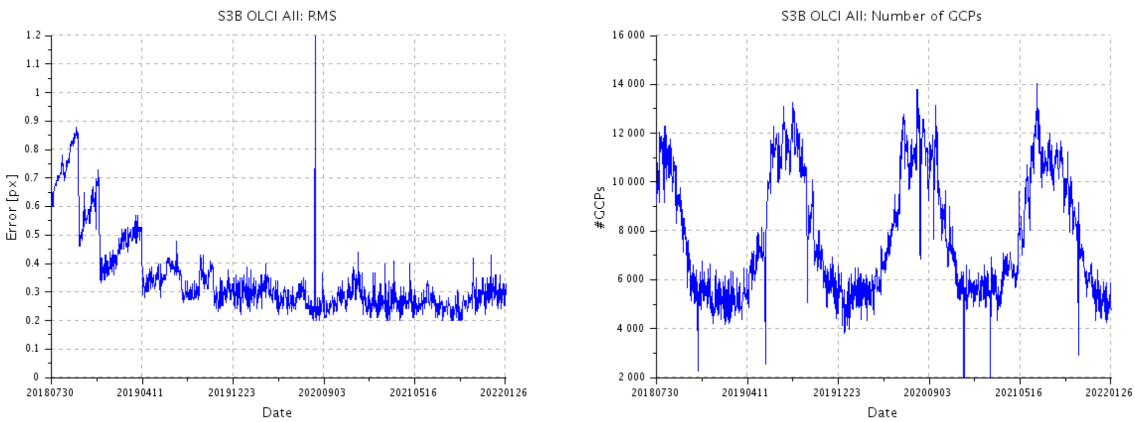

Figure 66: overall OLCI-B georeferencing RMS performance time series over the whole monitoring period (left) and corresponding number of validated control points (right)

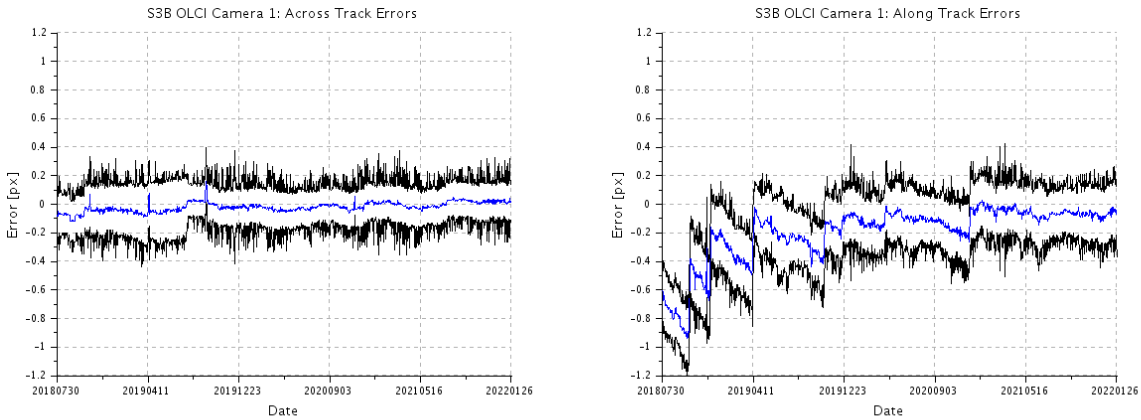

Figure 67: across-track (left) and along-track (right) OLCI-B georeferencing biases time series for Camera 1.

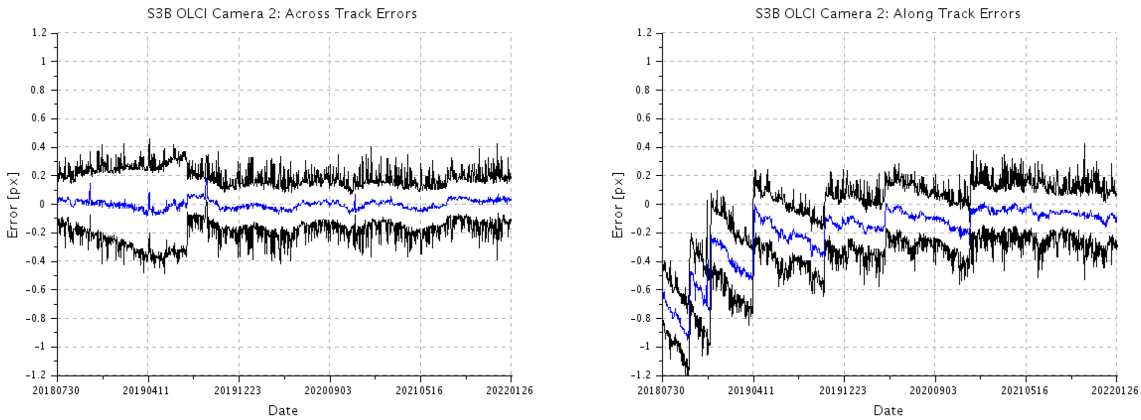

Figure 68: same as Figure 67 for Camera 2.

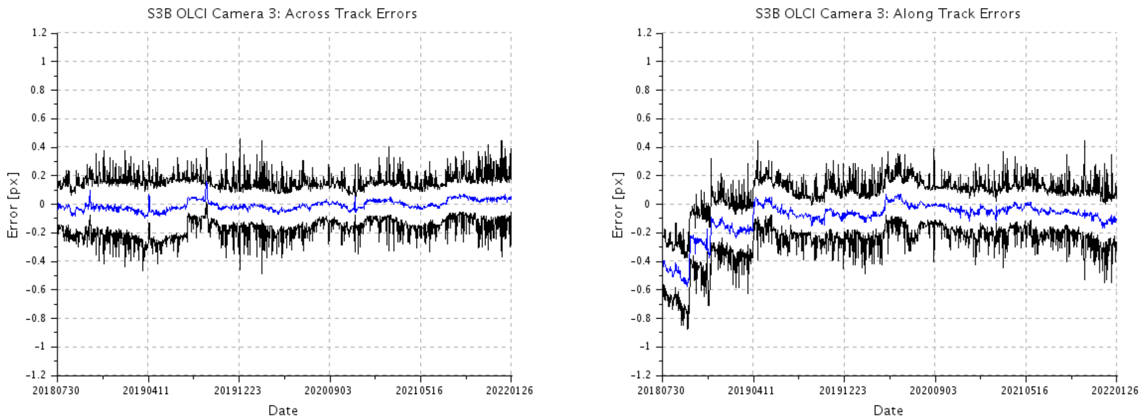

Figure 69: same as Figure 67 for Camera 3.

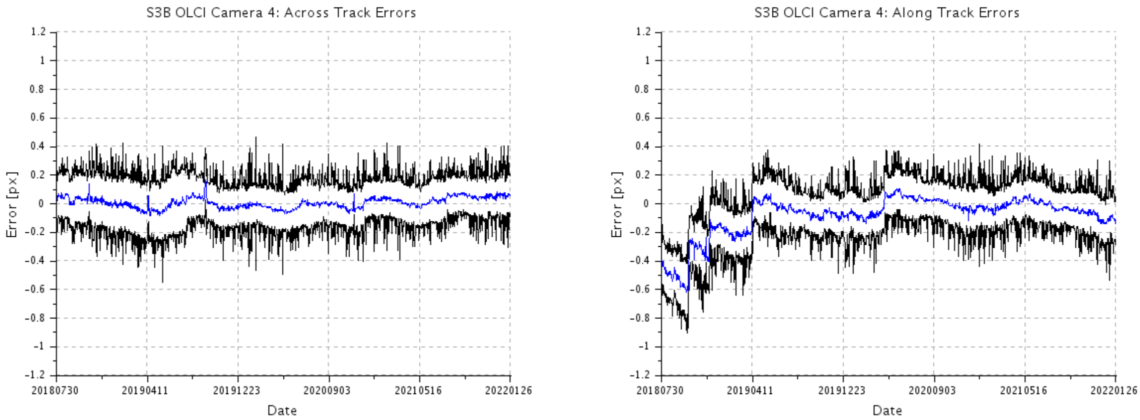

Figure 70: same as Figure 67 for Camera 4.

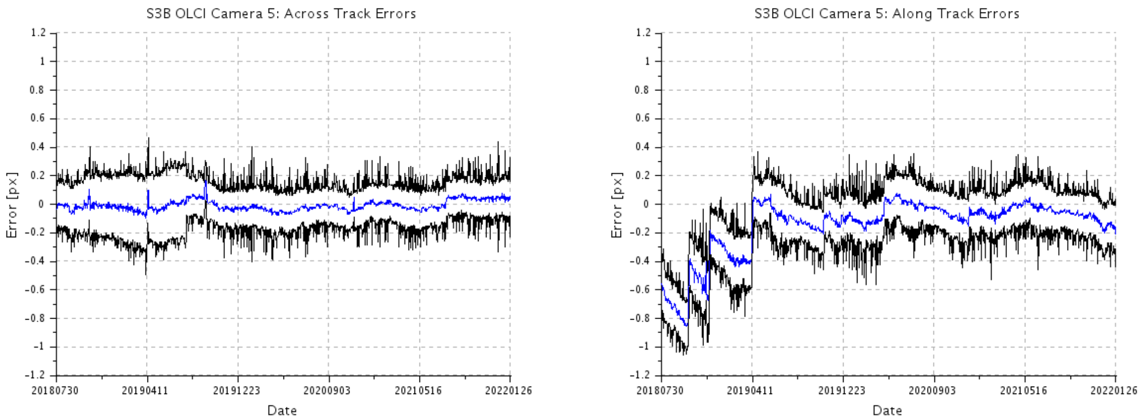

Figure 71: same as Figure 67 for Camera 5.

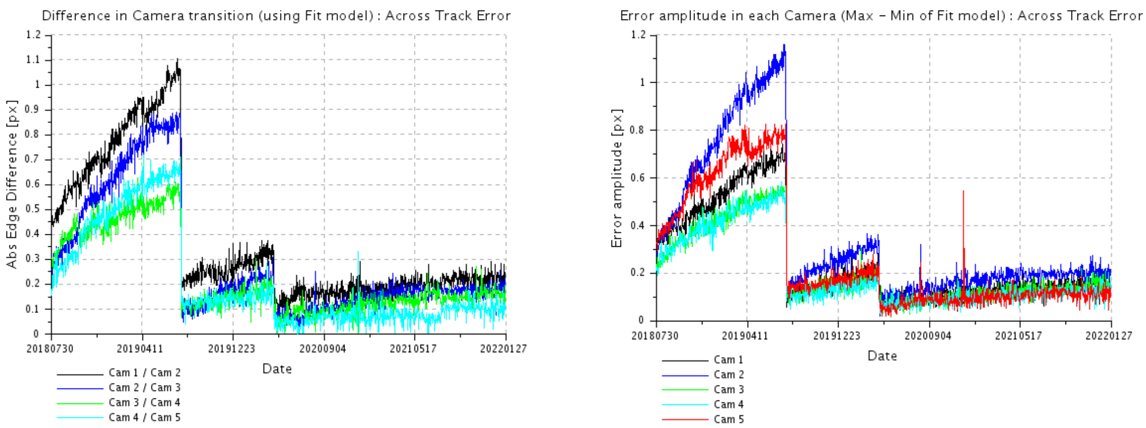

Figure 72: OLCI-B spatial across-track misregistration at each camera transition (left) and maximum amplitude of the across-track error within each camera (left).

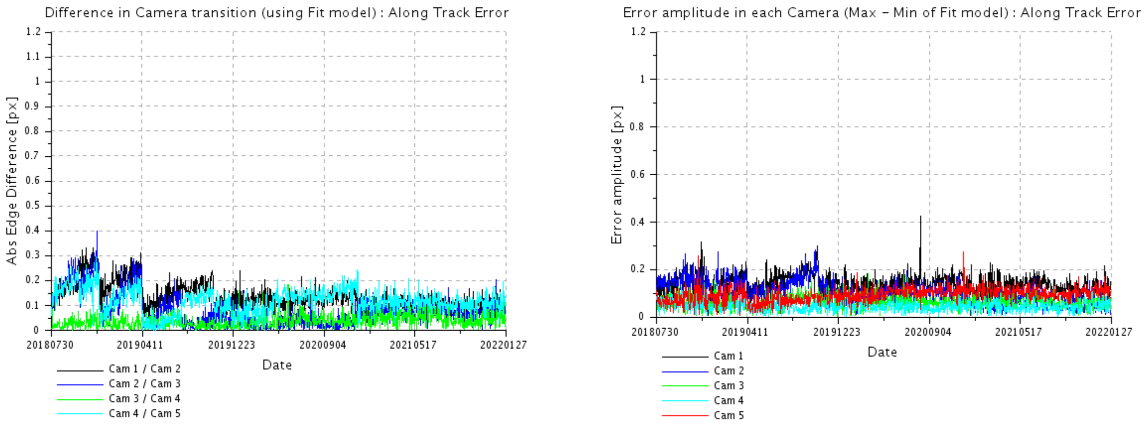

Figure 73: OLCI-B spatial along-track misregistration at each camera transition (left) and maximum amplitude of the along-track error within each camera (left).

3 OLCI Level 1 Product validation

3.1 [OLCI-L1B-CV-300], [OLCI-L1B-CV-310] – Radiometric Validation

3.1.1 S3ETRAC Service

Activities done

The S3ETRAC service extracts OLCI L1 RR and SLSTR L1 RBT data and computes associated statistics over 49 sites corresponding to different surface types (desert, snow, ocean maximizing Rayleigh signal, ocean maximizing sunglint scattering and deep convective clouds). The S3ETRAC products are used for the assessment and monitoring of the L1 radiometry (optical channels) by the ESLs.

All details about the S3ETRAC/OLCI and S3ETRAC/SLSTR statistics are provided on the S3ETRAC website http://s3etrac.acri.fr/index.php?action=generalstatistics.

- Number of OLCI products processed by the S3ETRAC service
- Statistics per type of target (DESERT, SNOW, RAYLEIGH, SUNGLINT and DCC)
- Statistics per sites
- Statistics on the number of records

For illustration, we provide below statistics on the number of S3ETRAC/OLCI records generated per type of targets (DESERT, SNOW, RAYLEIGH, SUNGLINT and DCC) for both OLCI-A (Figure 74) and OLCI-B (Figure 75).

Figure 74: summary of S3ETRAC products generation for OLCI-A
(number of OLCI-A L1 products Ingested, blue – number of S3ETRAC extracted products generated, green – number of S3ETRAC runs without generation of output product (data not meeting selection requirements), yellow – number of runs ending in error, red, one plot per site type).

Figure 75: summary of S3ETRAC products generation for OLCI-B (number of OLCI-B L1 products Ingested, yellow – number of S3ETRAC extracted products generated, blue – number of S3ETRAC runs without generation of output product (data not meeting selection requirements), green – number of runs ending in error, red, one plot per site type).

3.1.2 Radiometric validation with DIMITRI

Highlights

OLCI-A and OLCI-B L1B radiometry verification as follow:

- The verification is performed over Ocean-sites **until 20th January of 2022** and over Desert-sites **until 30th of December 2021**.
- All results from OLCI-A and OLCI-B over Rayleigh, Glint and PICS are consistent with the previous cycle over the used CalVal sites.
- Good stability of both sensors OLCI-A and OLCI-B could be observed, nevertheless the time-series average shows higher reflectance from OLCI-A.
- Bands with high gaseous absorption are excluded.

Verification and Validation over PICS

1. The ingestion of all the available L1B-LN1-NT products from OLCI-A and OLCI-B over the 6 desert CalVal-sites (Algeria3 & 5, Libya 1 & 4 and Mauritania 1 & 2) has been performed until the **30th of November 2021**.
2. The results are consistent over all the six used PICS sites (Figure 76 and Figure 77). Both sensors show a good stability over the analysed period.
3. The temporal average over the period **January 2021 - 30th December 2021** of the elementary ratios (observed reflectance to the simulated one) for **OLCI-A** shows gain values between 2-4% over all the VNIR bands (Figure 78). Unlikely, the temporal average over the same period of the elementary ratios for **OLCI-B** shows gain values within 2% (mission requirements) over the VNIR spectral range (Figure 78). The spectral bands with significant absorption from water vapor and O_2 (Oa11, Oa13, Oa14, Oa15 and Oa20) are excluded.

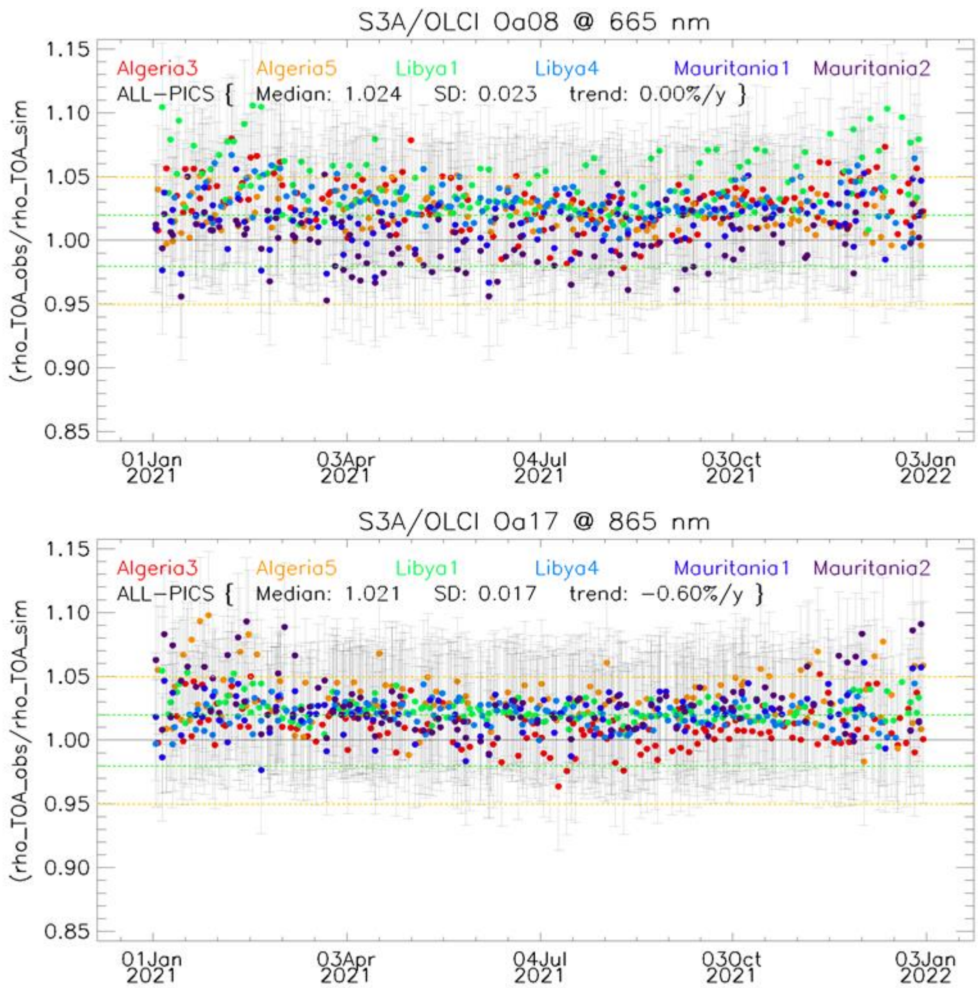

Figure 76: Time-series of the elementary ratios (observed/simulated) signal from OLCI-A for (top to bottom) bands Oa03 and Oa17 respectively over January 2021-Present from the six PICS Cal/Val sites. Dashed-green and orange lines indicate the 2% and 5% respectively. Error bars indicate the desert methodology uncertainty.

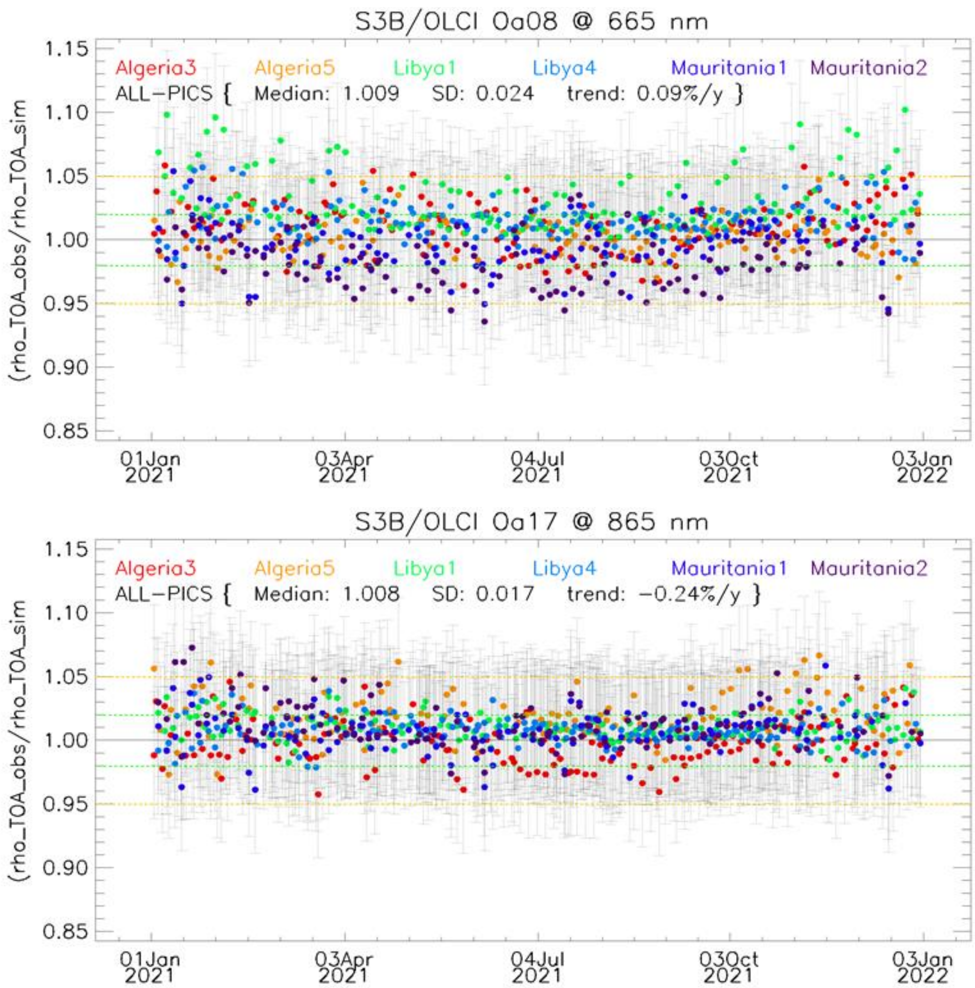

Figure 77: Time-series of the elementary ratios (observed/simulated) signal from OLCI-B for (top to bottom) bands Oa08 and Oa17 respectively over January 2021-Present from the six PICS Cal/Val sites. Dashed-green and orange lines indicate the 2% and 5% respectively. Error bars indicate the desert methodology uncertainty.

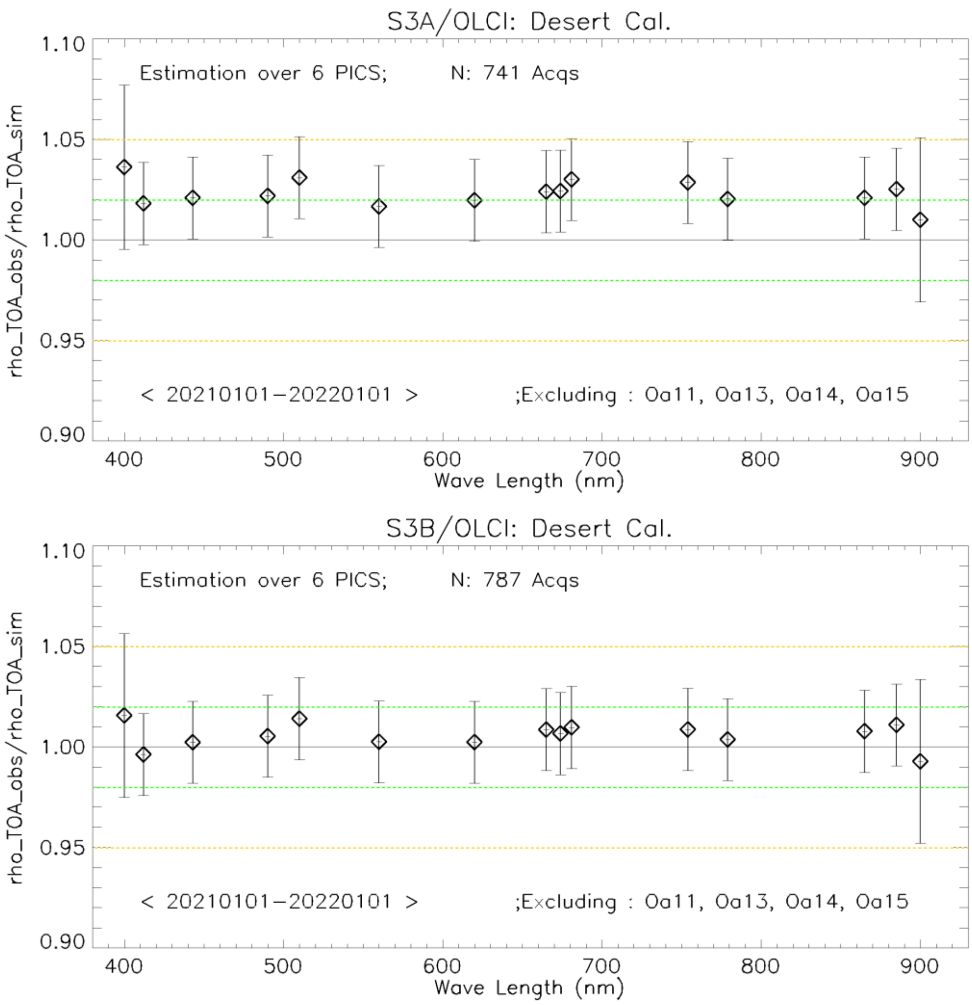

Figure 78: The estimated gain values for OLCI-A and OLCI-B over the 6 PICS sites identified by CEOS over the period January 2021-December 2021 as a function of wavelength. Dashed-green and orange lines indicate the 2% and 5% respectively. Error bars indicate the desert methodology uncertainty.

Validation over Rayleigh

Rayleigh method has been performed from the available mini-files over the **last 12 months** for OLCI-A and OLCI-B. The results were produced with the configuration (ROI-AVERAGE). The gain coefficients of OLCI-A are consistent with the previous results. Bands Oa01-Oa05 display biases values between 3%-5% while bands Oa06-Oa09 exhibit biases between about 2%, just within the mission requirement (Figure 79). The gain coefficients of OLCI-B are lower than OLCI-A ones, where bands Oa01-Oa05 display biases values about 2-5%, when bands Oa6-Oa9 exhibit biases around the 2% mission requirement (Figure 79).

Validation over Glint and synthesis

Glint calibration method with the configuration (ROI-PIXEL) has been performed over the **last 12 months** for OLCI-A and OLCI-B. The outcome of this analysis shows a good consistency with the desert and Rayleigh outputs over the NIR spectral range Oa06-Oa09 for both sensors. Glint results from OLCI-A show that the

NIR bands are within the 2% (mission requirements), except Oa21 which shows higher biases more than ~5% for both sensors (see Figure 79). Again, the glint gain from OLCI-B looks slightly lower than OLCI-A one.

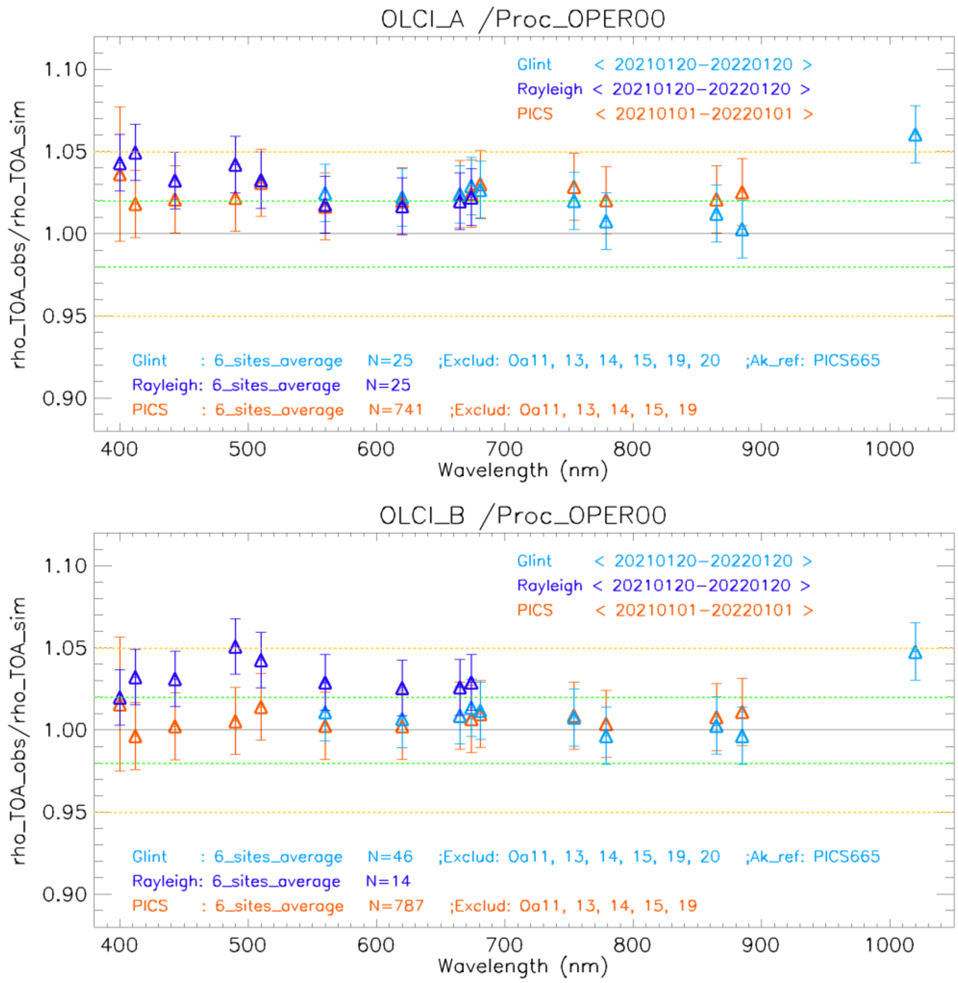

Figure 79: The estimated gain values for OLCI-A and OLCI-B from Glint, Rayleigh and PICS methods over the past twelve months as a function of wavelength. We use the gain value of Oa8 from PICS-Desert method as reference gain for Glint method. Dashed-green and orange lines indicate the 2% and 5% respectively. Error bars indicate the method uncertainties.

Cross-mission Intercomparison over PICS:

X-mission Intercomparison with MODIS-A MSI-A and MSI-B has been performed until October 2021.

Figure 80 shows the estimated gain over different time-series for different sensors over PICS. The spectral bands with significant absorption from water vapor and O2 are excluded. OLCI-A seems to have higher gain wrt the other sensors, and about 1-2% higher gain wrt to OLCI-B over VNIR spectral range.

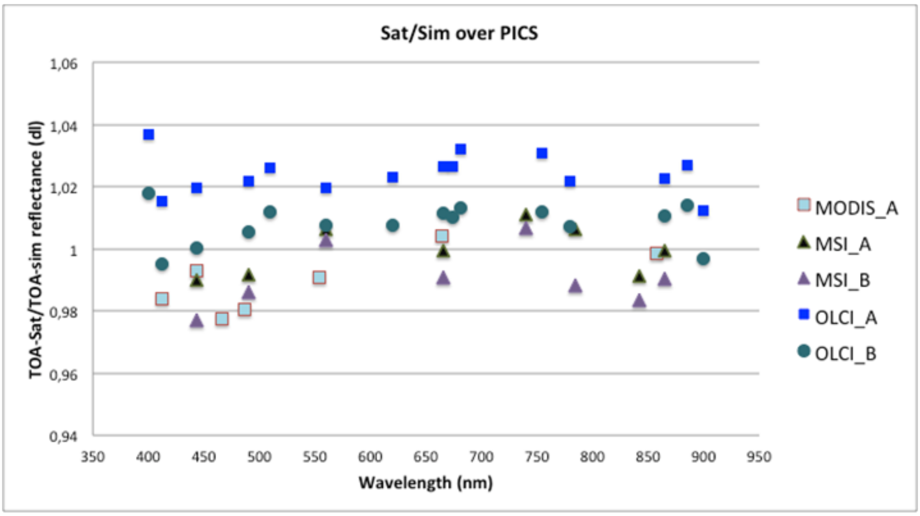

Figure 80: Ratio of observed TOA reflectance to simulated one for (green-yellow) S2A/MSI, (red) Aqua/MODIS, (blue) S3A/OLCI and (green) S3B/OLCI averaged over the six PICS test sites as a function of wavelength.

3.1.3 Radiometric validation with OSCAR

OSCAR Rayleigh results

The OSCAR Rayleigh have been applied to the S3A and S3B S3ETRAC data from the 6 oceanic calibration sites (Table 3) using a new chlorophyll climatology which has been derived from the CMEMS OLCI monthly CHL products from considering the years 2017, 2018 and 2019.

Table 3: S3ETRAC Rayleigh Calibration sites

Site Name	Ocean	North Latitude	South Latitude	East Longitude	West Longitude
PacSE	South-East of Pacific	-20.7	-44.9	-89	-130.2
PacNW	North-West of Pacific	22.7	10	165.6	139.5
PacN	North of Pacific	23.5	15	200.6	179.4
AtlN	North of Atlantic	27	17	-44.2	-62.5
AtlS	South of Atlantic	-9.9	-19.9	-11	-32.3
IndS	South of Indian	-21.2	-29.9	100.1	89.5

In Figure 81 the average OSCAR OLCI-A and OLCI-B Rayleigh results are given for November 2021 (only partially processed). In Figure 82 and Table 4 the average of all scenes currently (re)processed with this new climatology is given. The (re)processing was done on the S3ETRAC scenes from all months of 2019 and 2020, and Jan – Nov. 2021.

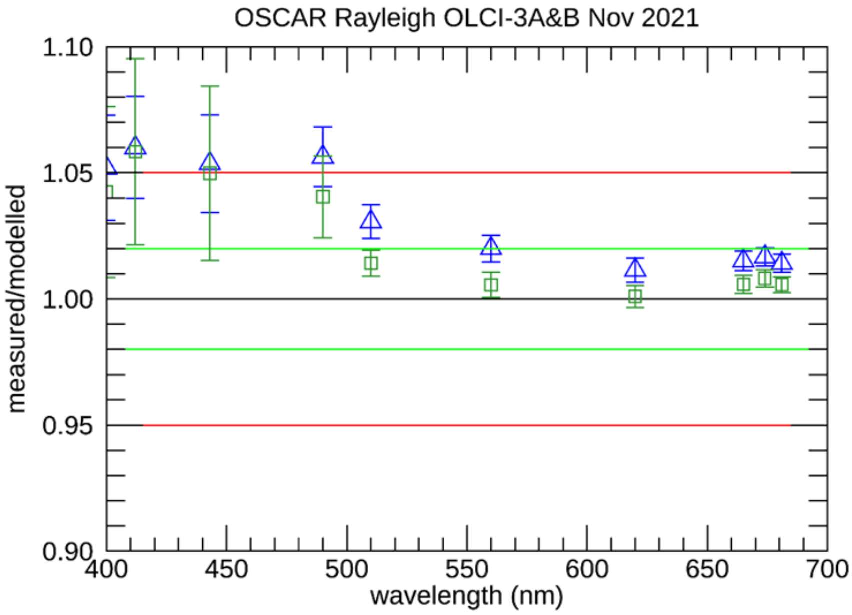

Figure 81: OSCAR Rayleigh S3A and S3B Calibration results as a function of wavelength for November 2021. The results are obtained with a new climatology derived from CMEMS OLCI monthly CHL products.

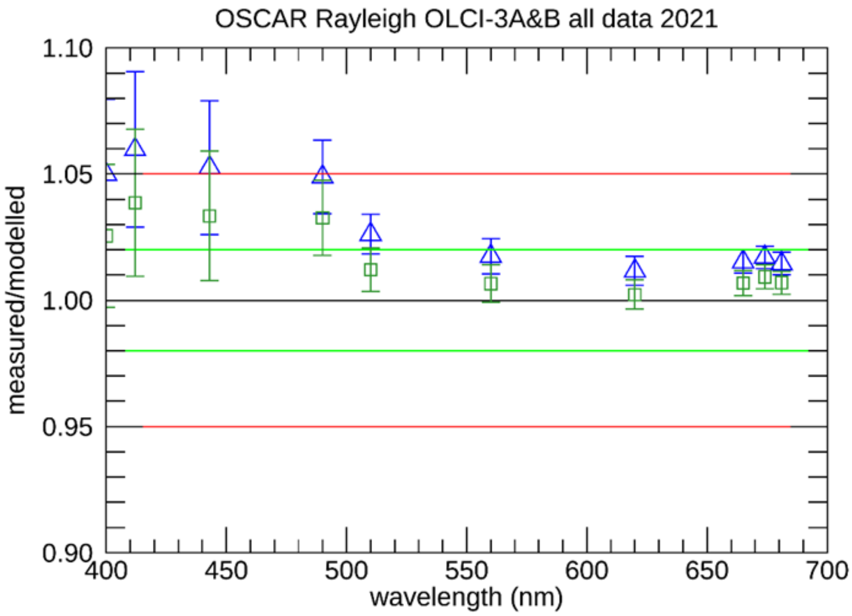

Figure 82. OSCAR Rayleigh S3A and S3B Calibration results as a function of wavelength for Jan – November 2021. Average and standard deviation over all scenes currently (re)processed with the new climatology.

Table 4. OSCAR Rayleigh calibration results for S3A and S3B (average and standard deviation over all acquisitions) over all scenes currently (re)processed with the new climatology and observed difference (in %) between OLCIA and OLCIB

OLCI band	Wavelength	Oscar Rayleigh OLCIA		Oscar Rayleigh OLCIB		% difference OLCIA and OLCIB
	(nm)	avg	stdev	avg	stdev	
Oa01	400	1.050	0.030	1.026	0.028	2.32%
Oa02	412	1.060	0.031	1.039	0.029	1.98%
Oa03	443	1.053	0.027	1.033	0.025	1.82%
Oa04	490	1.049	0.015	1.033	0.015	1.54%
Oa05	510	1.026	0.008	1.012	0.009	1.37%
Oa06	560	1.017	0.007	1.007	0.007	1.07%
Oa07	620	1.012	0.006	1.002	0.006	0.92%
Oa08	665	1.015	0.005	1.007	0.005	0.83%
Oa09	674	1.017	0.004	1.009	0.005	0.76%
Oa10	681	1.015	0.004	1.007	0.005	0.75%
Oa11	709	0.998	0.008	0.993	0.008	0.45%
Oa12	754	1.009	0.001	1.008	0.002	0.13%

4 Level 2 Land products validation

4.1 [OLCI-L2LRF-CV-300]

4.1.1 Routine extractions

- The focus for this time period has been on the rolling archive Non Time Critical (NT) data until the 3rd of December 2021. More data available for statistical analysis as a concatenation procedure for all available data in the MERMAID processing has been implemented.
- Concatenated time series of OLCI Global Vegetation Index and OLCI Terrestrial Chlorophyll Index have been regenerated on the current rolling archive availability including previous extractions since June 2016 and April 2018 for S3A and S3B respectively.

4.1.1.1 OLCI-A

Figure 83 to Figure 92 below present the Core Land Sites OLCI-A time series over the current period.

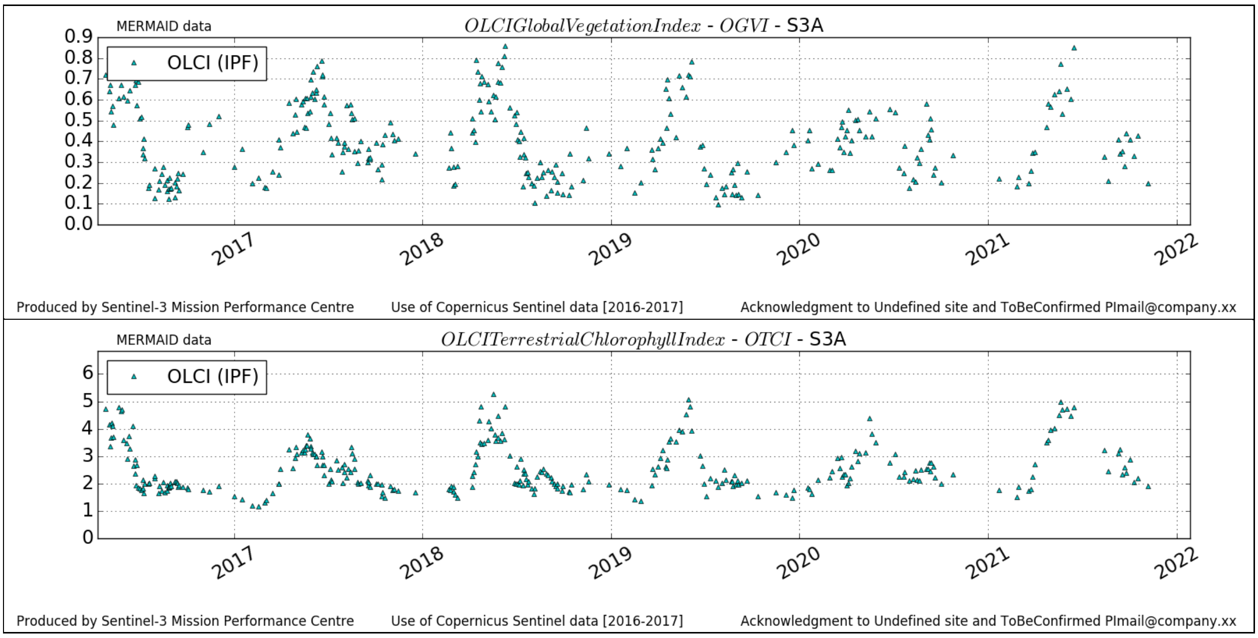

Figure 83: DeGeb time series over current report period

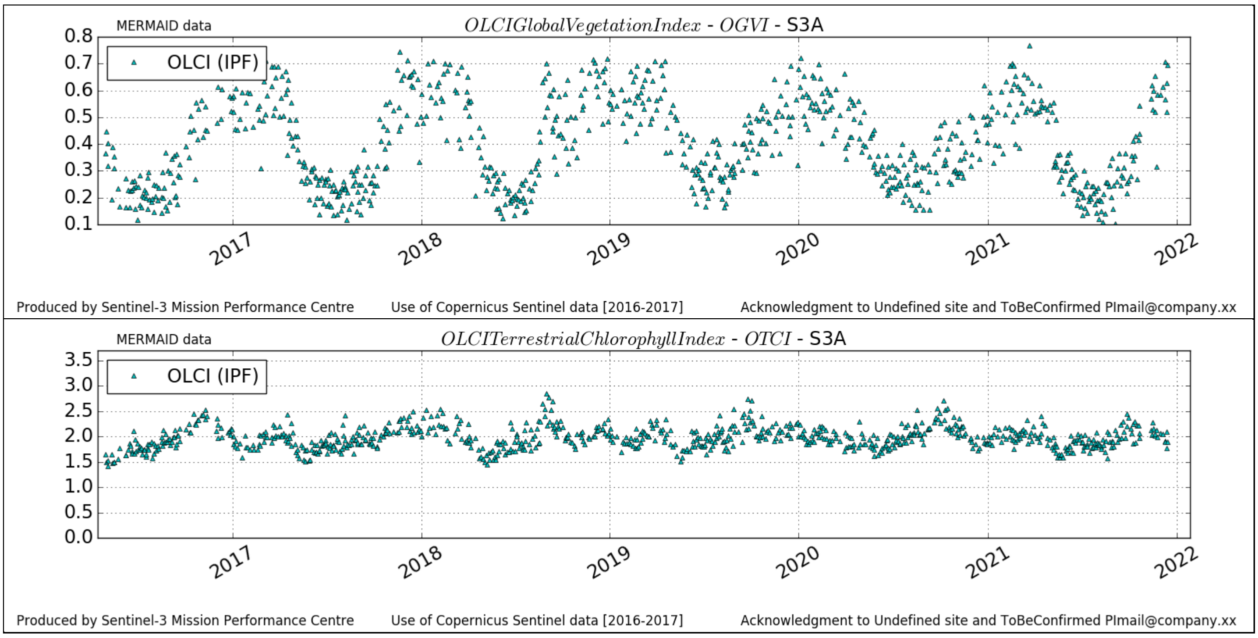

Figure 84: ITCat time series over current report period

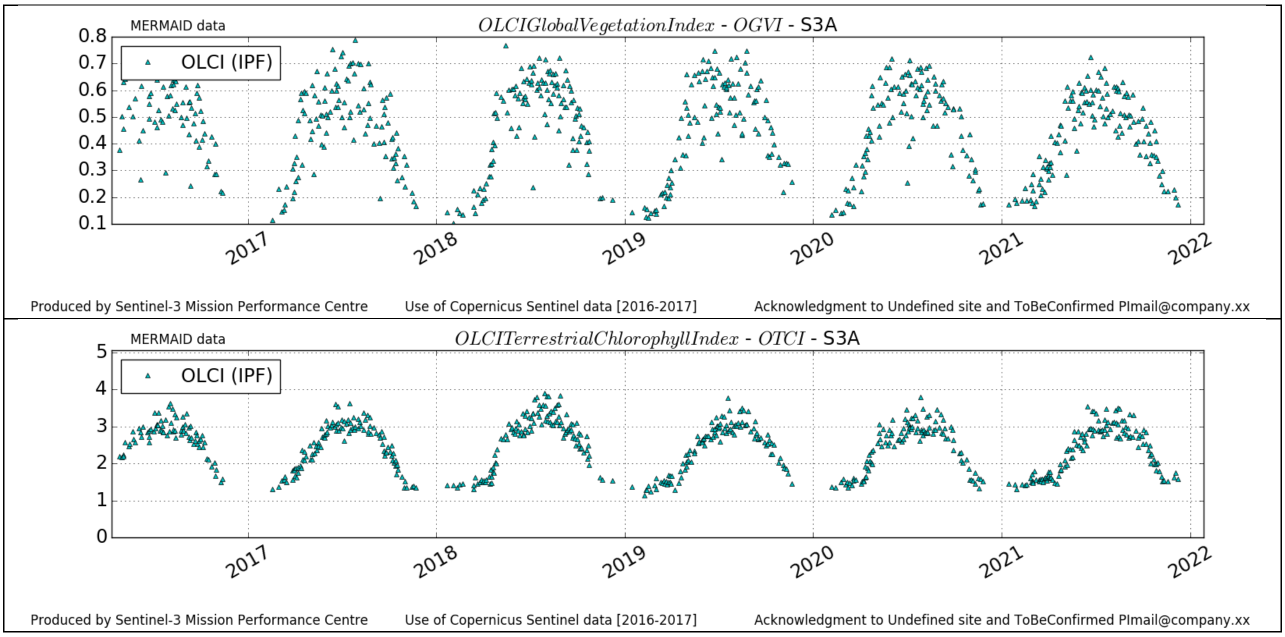

Figure 85: ITIsp time series over current report period

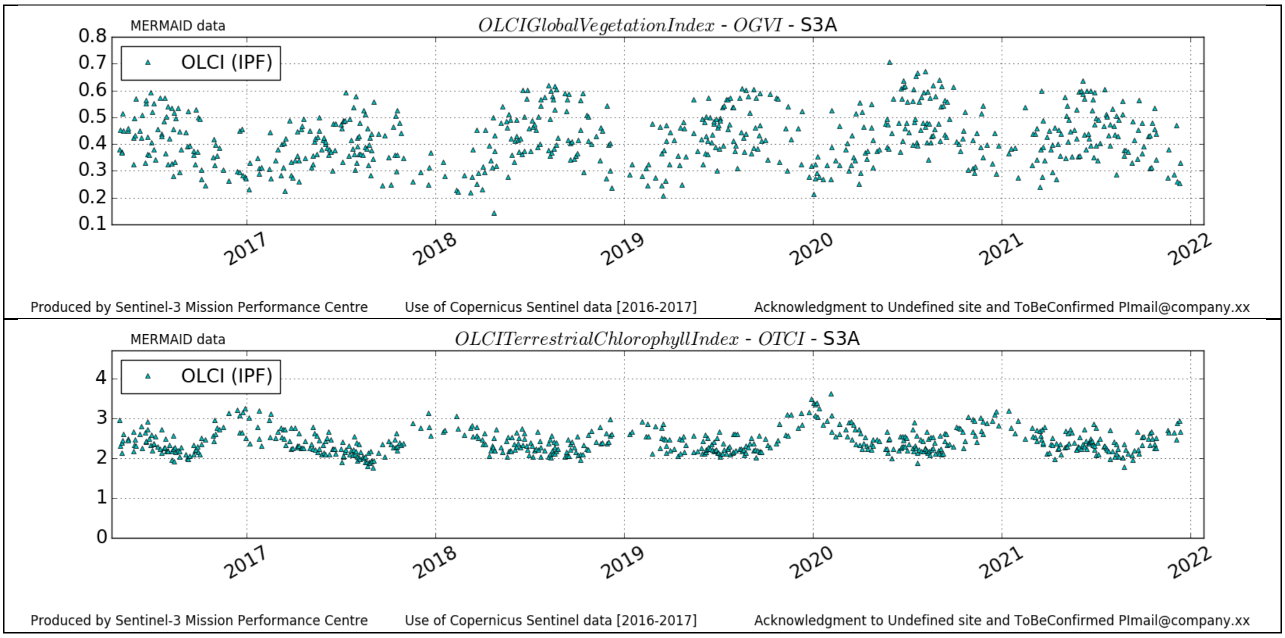

Figure 86: ITSro time series over current report period

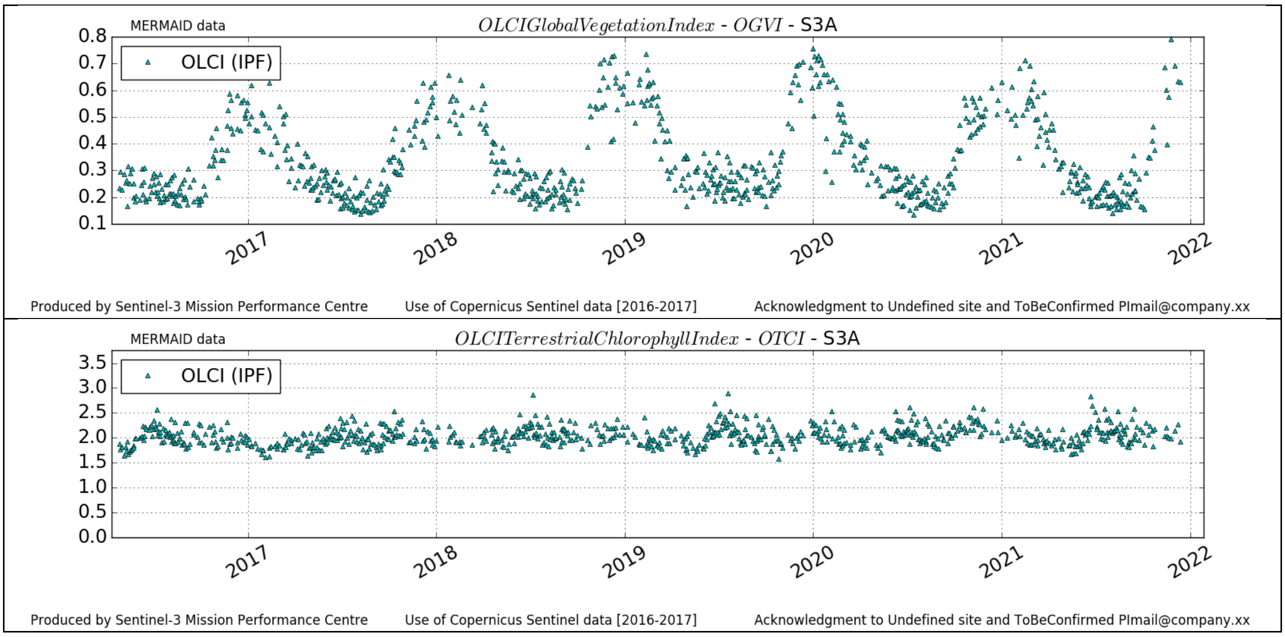

Figure 87: ITTra time series over current report period

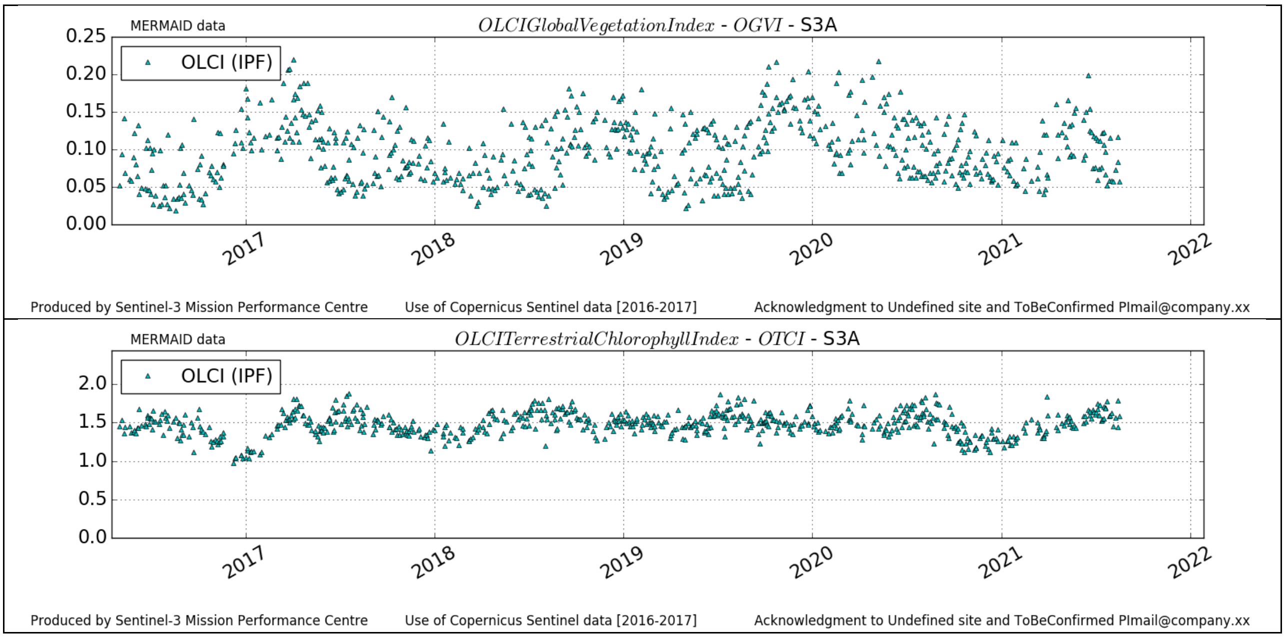

Figure 88: SPAli time series over current report period

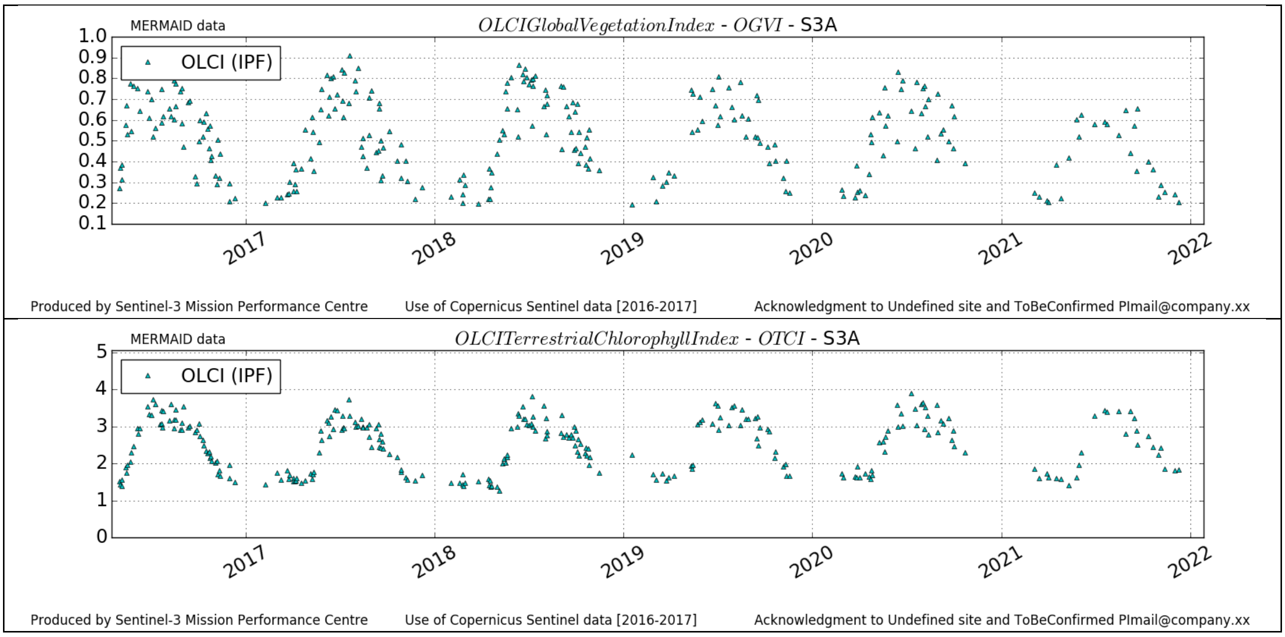

Figure 89: UKNFo time series over current report period

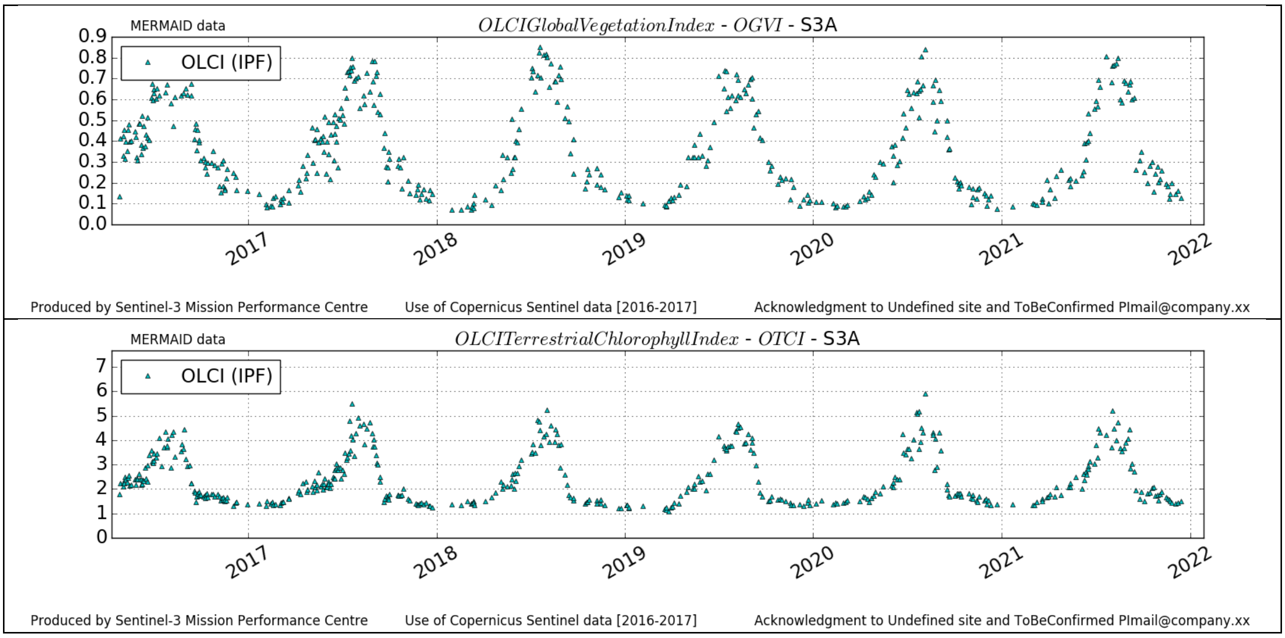

Figure 90: USNe1 time series over current report period

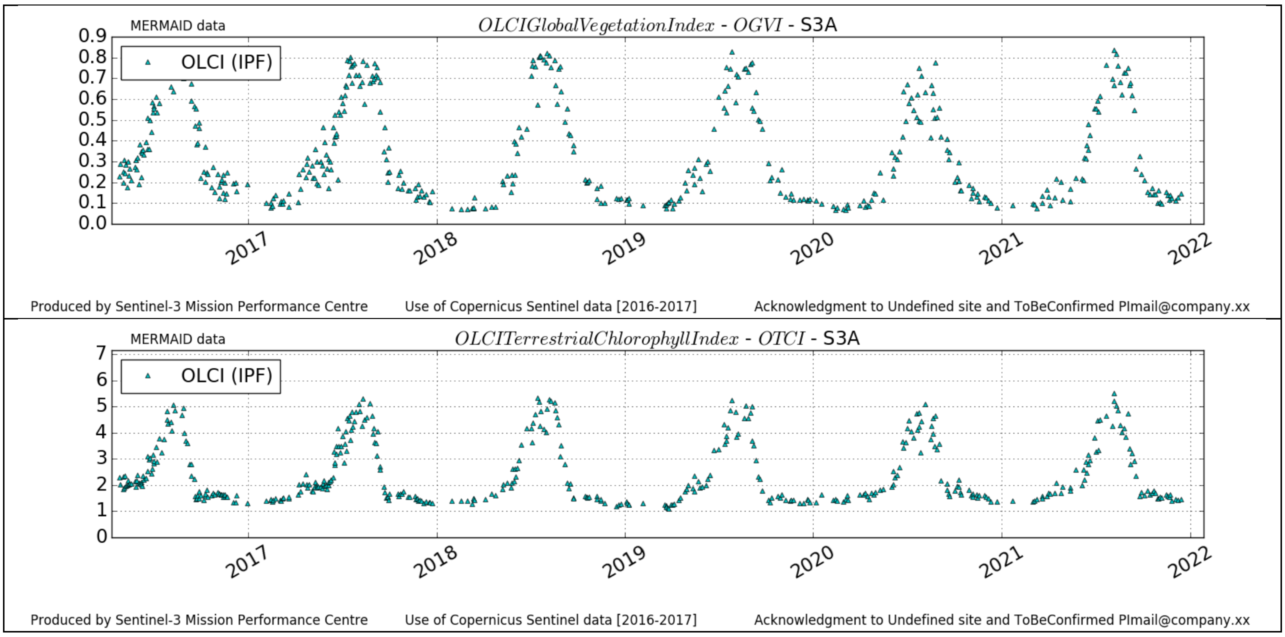

Figure 91: USNe2 time series over current report period

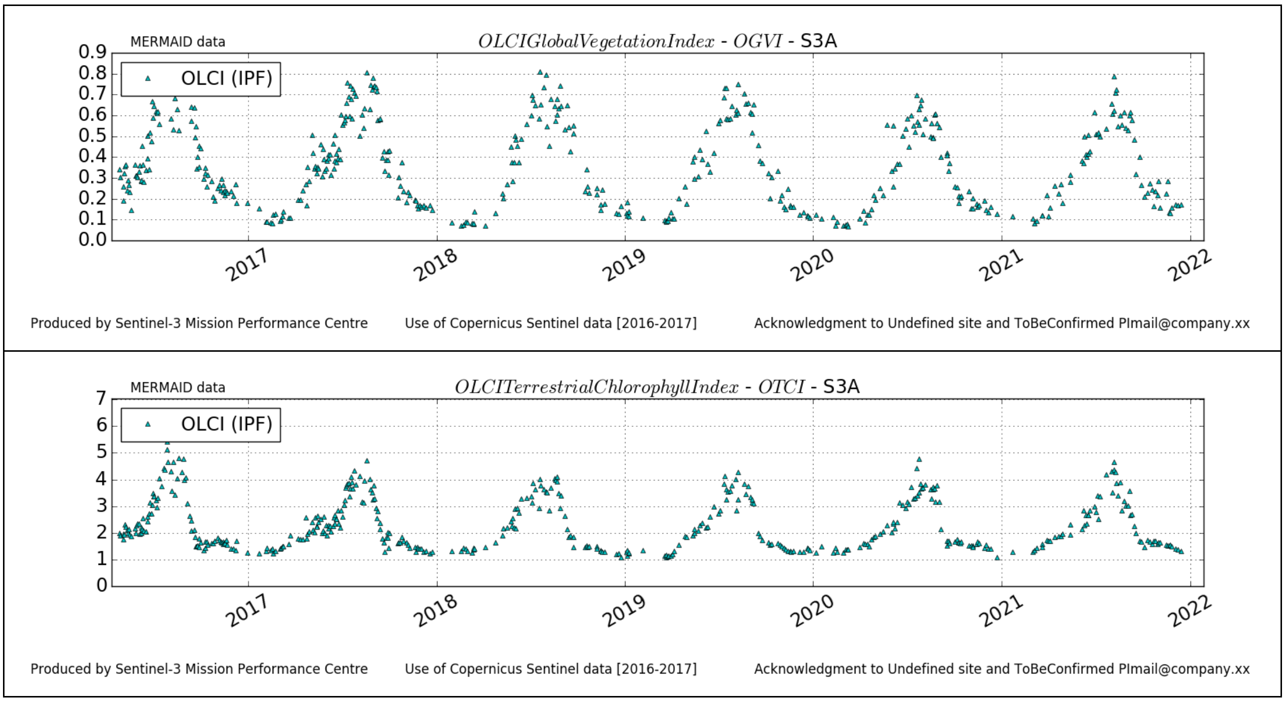

Figure 92: USNe3 time series over current report period

4.1.1.2 OLCI-B

Figure 93 to Figure 102 below present the Core Land Sites OLCI-B time series over the current period.

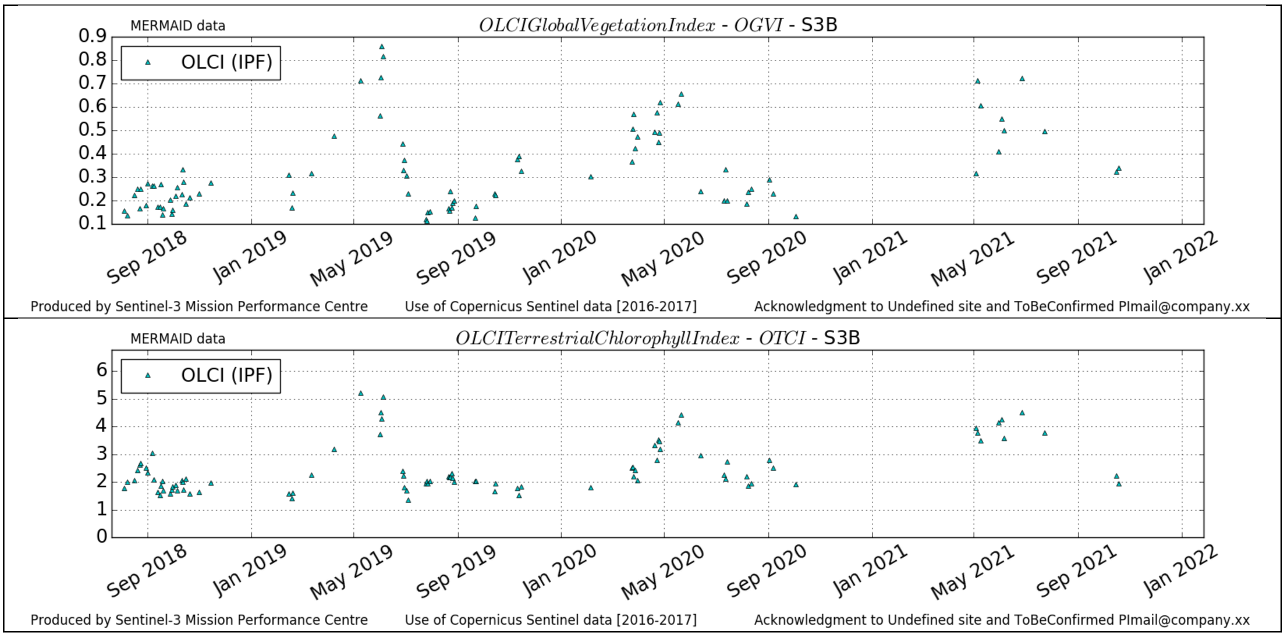

Figure 93: DeGeb time series over current report period

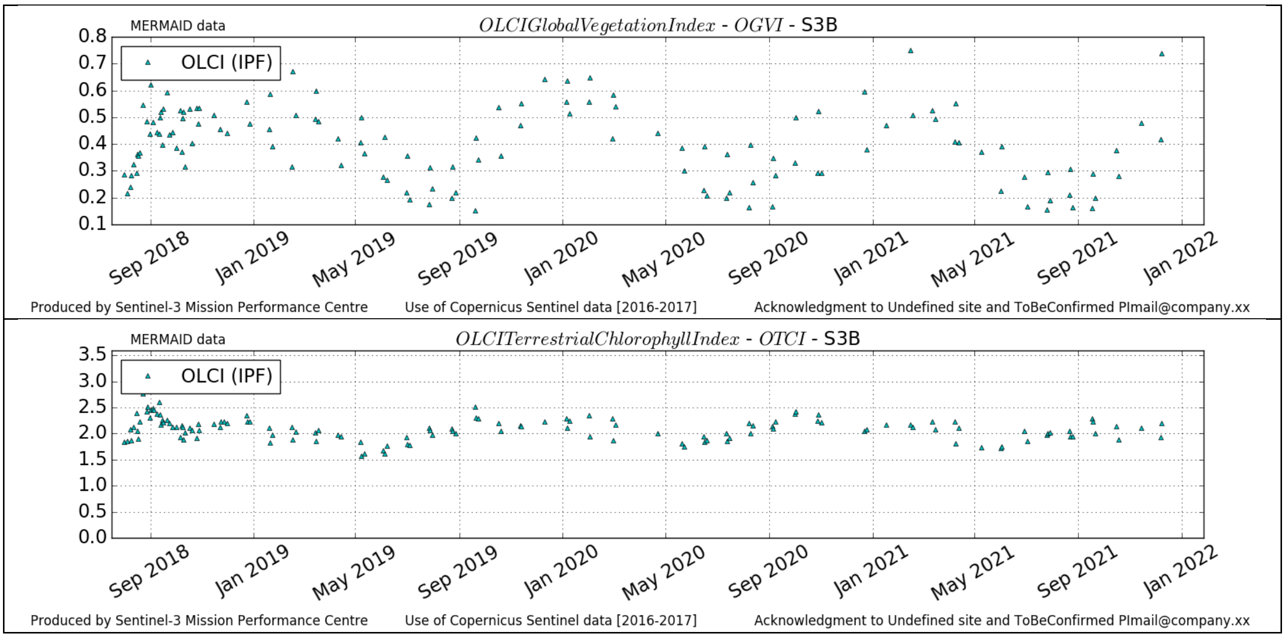

Figure 94: ITCat time series over current report period

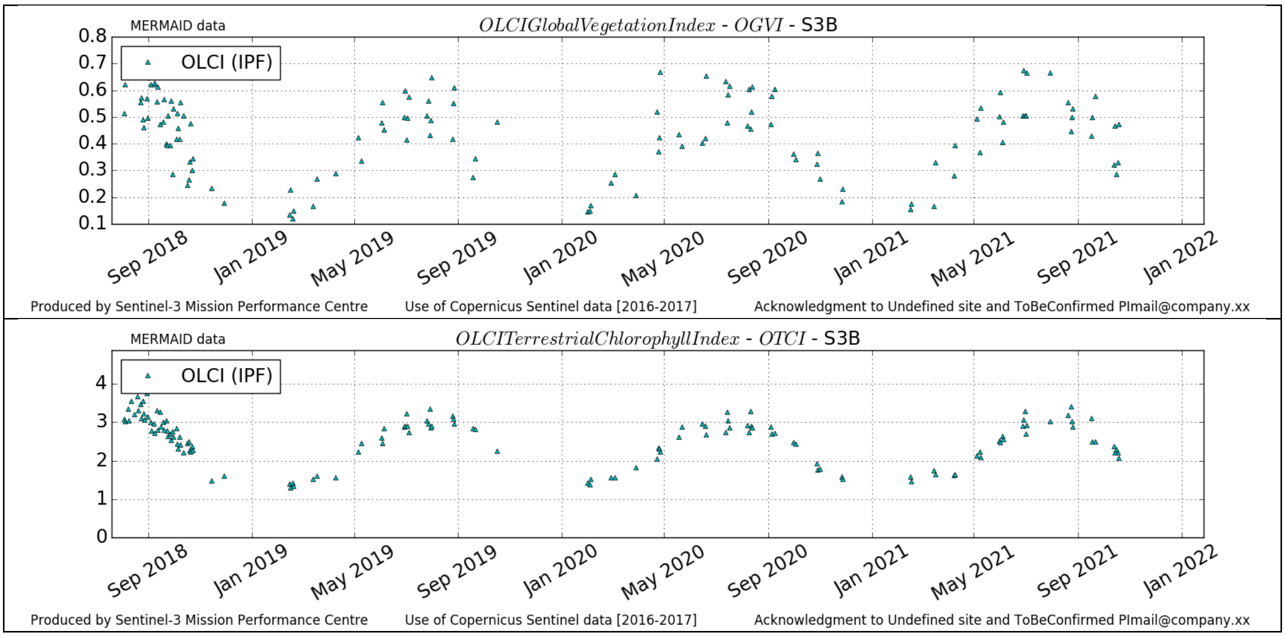

Figure 95: ITIsp time series over current report period

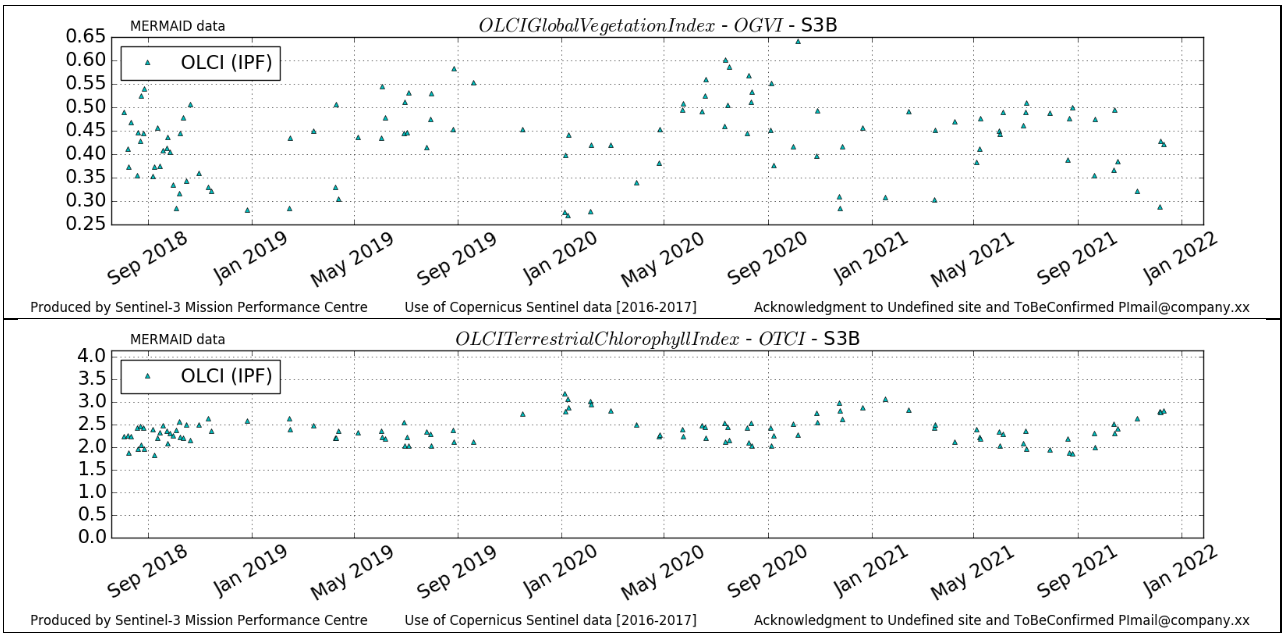

Figure 96: ITSro time series over current report period

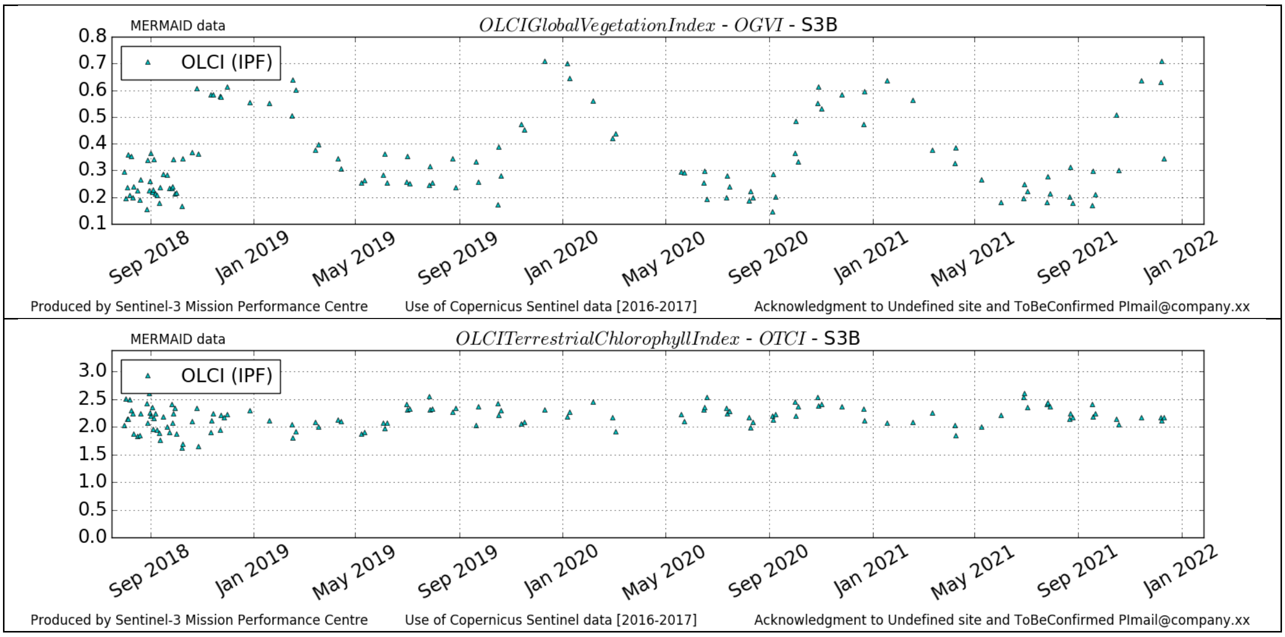

Figure 97: ITTra time series over current report period

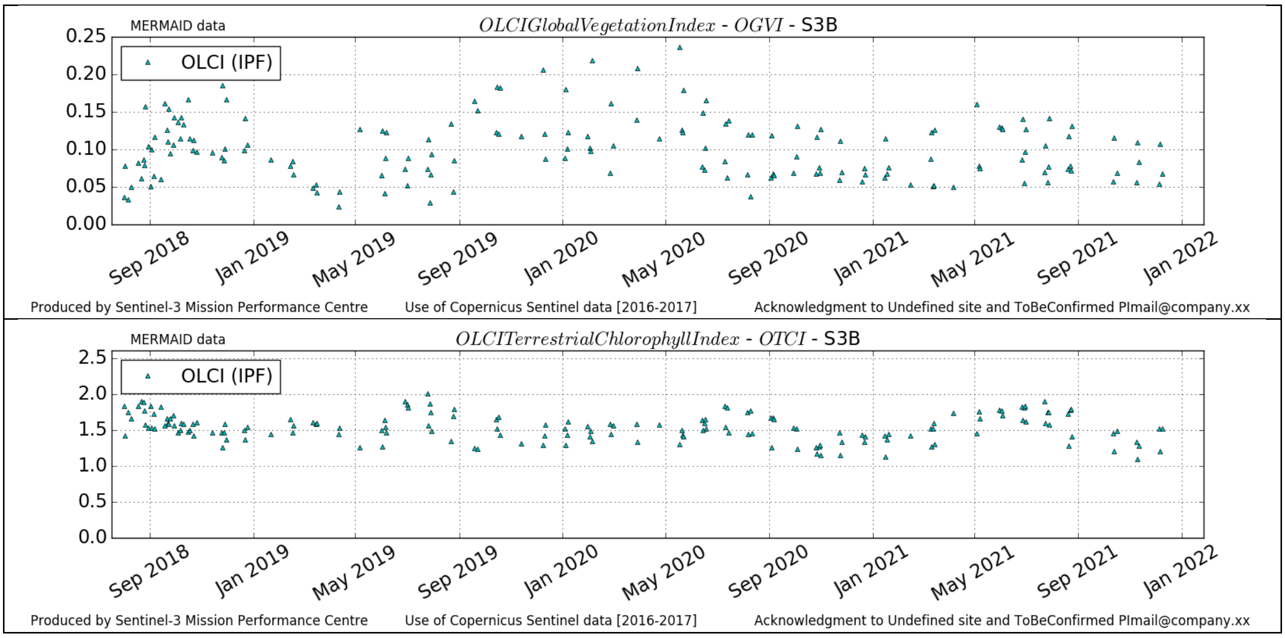

Figure 98: SPAli time series over current report period

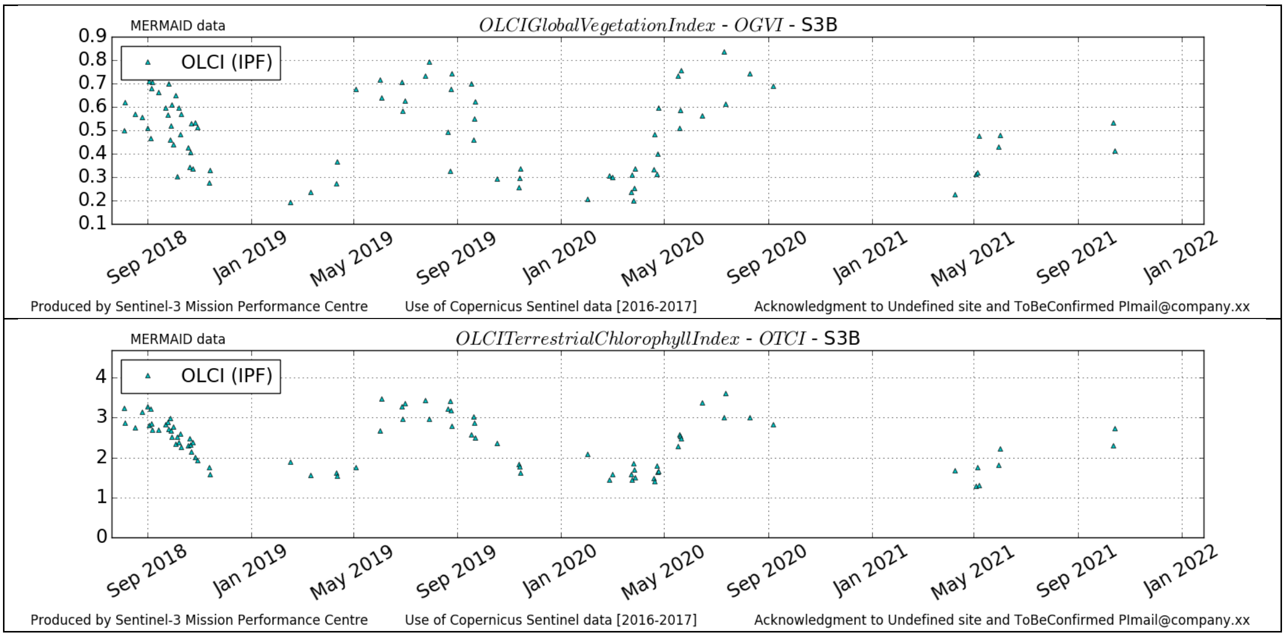

Figure 99: UKNFo time series over current report period

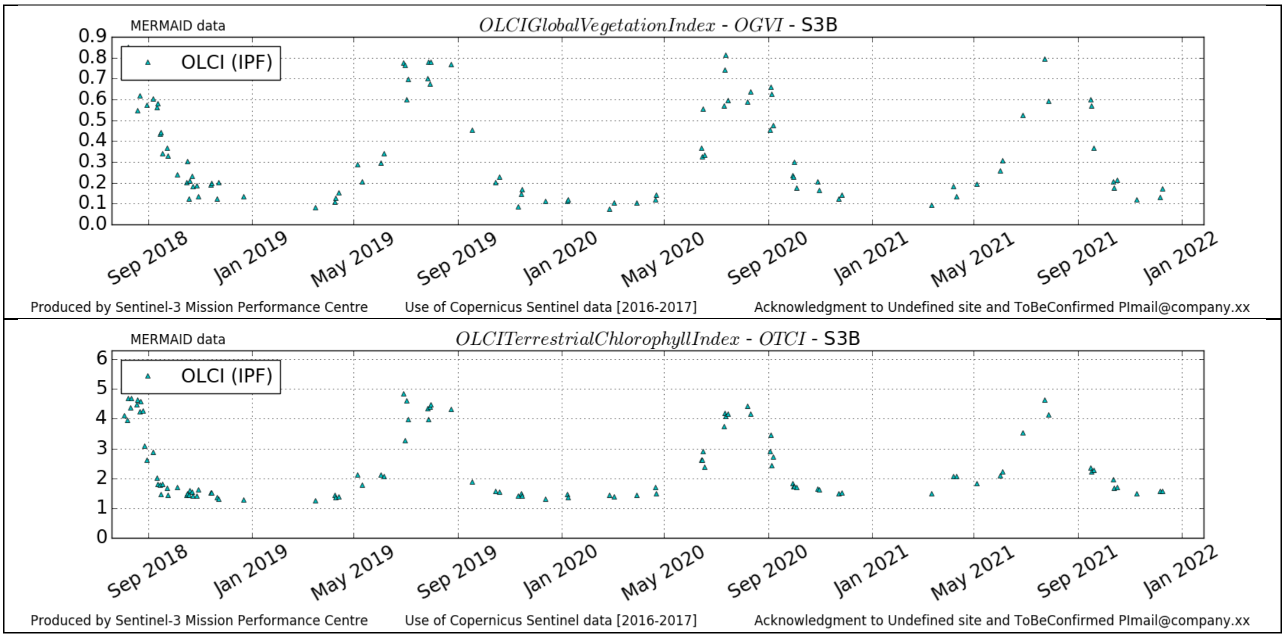

Figure 100: USNe1 time series over current report period

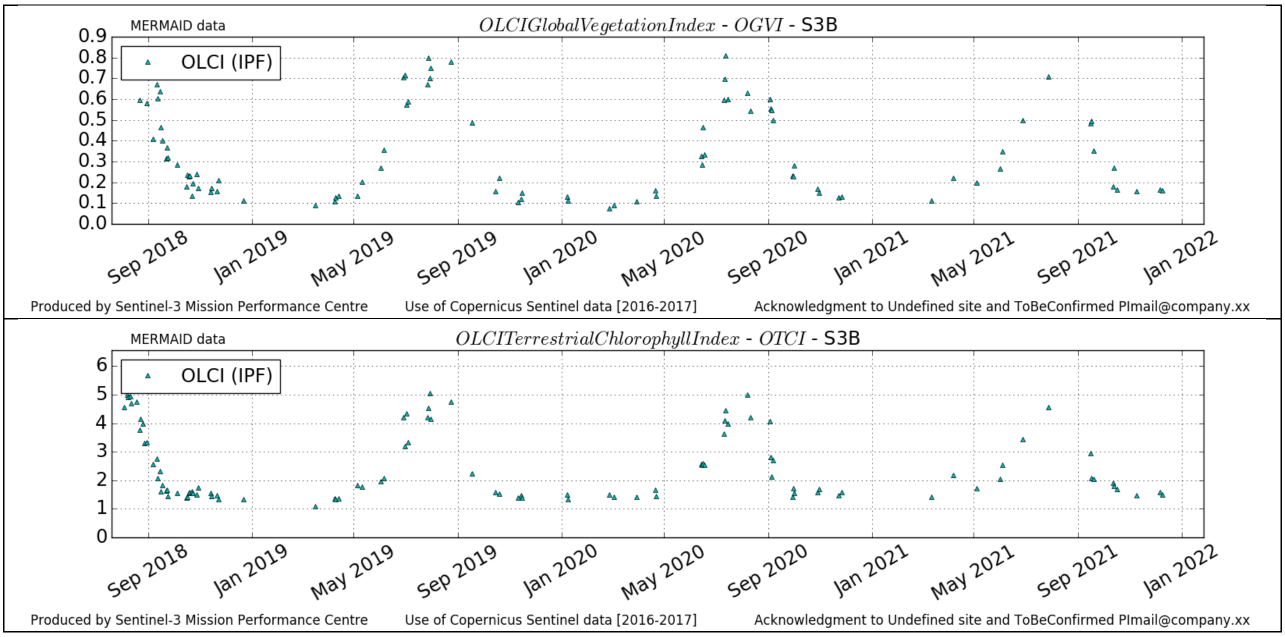

Figure 101: USNe2 time series over current report period

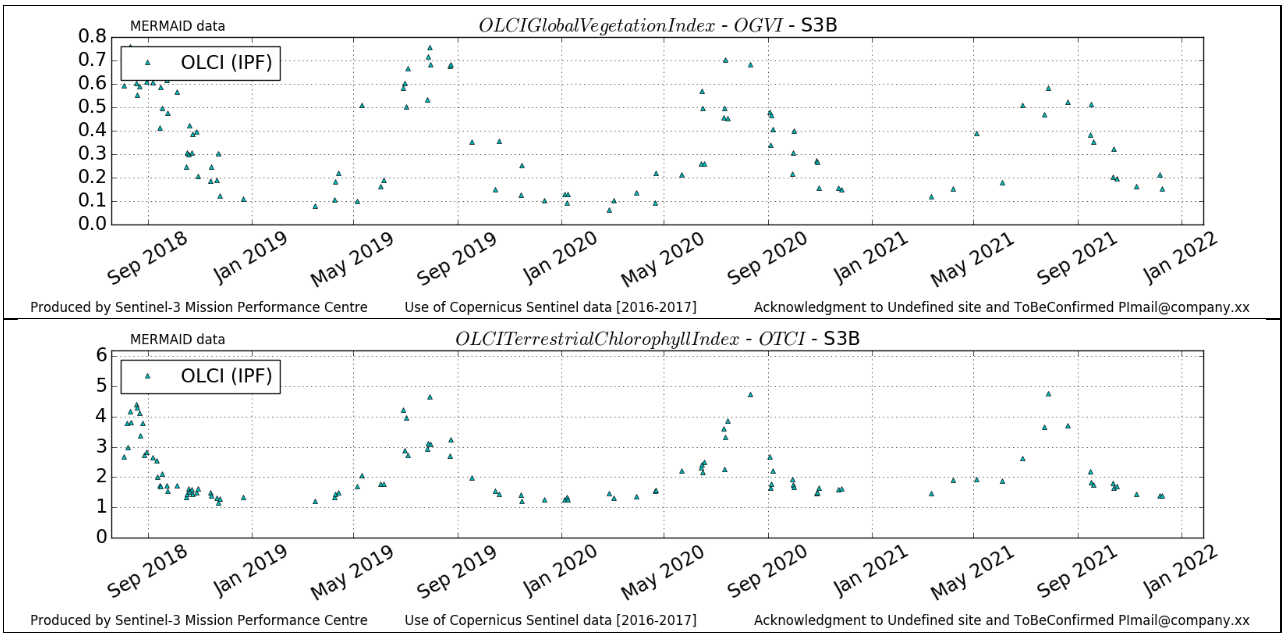

Figure 102: USNe3 time series over current report period

4.1.2 Comparisons with MERIS MGVI and MTCI climatology

This report presents the comparison between MERIS and OLCI land products between the 5th November 2021 and the 3rd December 2021. The comparison is conducted using 3x3 pixel extractions over 42 established validation sites. The sites are distributed across a range of latitudes and include representative land cover types (Table 5). Statistical measures of the comparison between MERIS and OLCI products are presented in Table 6. In general, there is good agreement between the land products with strong R^2 values and biases around 0. There are similar seasonal trajectories and timings shown in the extractions from both products at the following sites reviewed in this monthly report: BE-Brasschaat, DE-Hainich and FR-EstreesMons (Figure 103 to Figure 105). The monthly mean extractions from all sites is shown in Figure 106. OTCI from S3A shows a strong agreement with the MERIS archive, R^2 = 0.93, NRMSD < 0.08 with a low bias, -0.02. OGVI similarly shows a strong agreement with the MERIS archive, R^2 = 0.93, NRMSD < 0.16 with a slightly higher bias of 0.06.

Table 5: Validation sites analysed in report S3A 70/S3B 51. Land cover data from GLC2000 grouped according to the International Geosphere-Biosphere Programme (IGBP) designations.

Acronym	Country	Network	Lat	Lon	Land cover
AU-Cape-Tribulation	Australia	TERN-SuperSites, OzFlux	-16.106	145.378	EBF
AU-Cumberland	Australia	TERN-SuperSites, AusCover/OzFlux	-33.615	150.723	EBF
AU-Great-Western	Australia	TERN-SuperSites, AusCover/OzFlux	-30.192	120.654	DBF
AU-Litchfield	Australia	TERN-SuperSites, AusCover/OzFlux	-13.18	130.79	EBF
AU-Robson-Creek	Australia	TERN-SuperSites, AusCover/OzFlux	-17.117	145.63	EBF
AU-Rushworth	Australia	TERN-AusCover	-36.753	144.966	DBF
AU-Tumbarumba	Australia	TERN-SuperSites, AusCover/OzFlux	-35.657	148.152	EBF
AU-Warra-Tall	Australia	TERN-SuperSites, AusCover/OzFlux	-43.095	146.654	EBF
AU-Watts-Creek	Australia	TERN-AusCover	-37.689	145.685	EBF
AU-Wombat	Australia	TERN-SuperSites, AusCover/OzFlux	-37.422	144.094	EBF
BE-Brasschaat	Belgium	ICOS	51.308	4.52	ENF
BE-Vielsalm	Belgium	ICOS	50.305	5.998	ENF
BR-Mata-Seca	Brazil	ENVIRONET	-14.88	-43.973	non-forest
CA-Mer-Bleue	Canada	National Capitol Comission	45.4	-75.493	non-forest
CR-Santa-Rosa	Costa Rica	ENVIRONET	10.842	-85.616	EBF
CZ-Bili-Kriz	Czechia	ICOS	49.502	18.537	ENF
DE-Haininch	Deutschland	ICOS Associated	51.079	10.453	DBF
DE-Hones-Holz	Deutschland	ICOS	52.085	11.222	DBF
DE-Selhausen	Deutschland	ICOS	50.866	6.447	cultivated
DE-Tharandt	Deutschland	ICOS	50.964	13.567	ENF
FR-Aurade	France	ICOS	43.55	1.106	cultivated
FR-Estrees-Mons	France	ICOS Associated	49.872	3.021	cultivated
FR-Guayaflux	France	ICOS Associated	5.279	-52.925	EBF
FR-Hesse	France	ICOS	48.674	7.065	DBF
FR-Montiers	France	ICOS	48.538	5.312	DBF
FR-Puechabon	France	ICOS	43.741	3.596	ENF
IT-Casterporziano2	Italy	ICOS	41.704267	12.357293	DBF
IT-Collelongo	Italy	EFDC	41.849	13.588	DBF
IT-Lison	Italy	ICOS	45.74	12.75	cultivated
NE-Loobos	Netherlands	ICOS Associated	52.166	5.744	ENF
SE-Dahra	Senegal	KIT / UC	15.4	-15.43	cultivated
UK-Wytham-Woods	United Kingdom	ForestGeo - NPL	51.774	-1.338	DBF
US-Bartlett	United States	NEON, AERONET	44.064	-71.287	DBF
US-Central-Plains	United States	NEON, AERONET	40.816	-104.746	non-forest
US-Harvard	United States	NEON, AERONET	42.537	-72.173	DBF
US-Moab-Site	United States	NEON, AERONET	38.248	-109.388	non-forest
US-Mountain-Lake	United States	NEON, AERONET	37.378	-80.525	DBF
US-Oak-Rige	United States	NEON, AERONET	35.964	-84.283	DBF
US-Ordway-Swisher	United States	NEON, AERONET	29.689	-81.993	ENF
US-Smithsonian	United States	NEON, AERONET	38.893	-78.14	DBF
US-Steigerwarldt	United States	NEON	45.509	-89.586	DBF
US-Talladega	United States	NEON, AERONET	32.95	-87.393	ENF

Table 6: Comparison statistics between monthly S3A/B OLCI land products and MERIS archive data.

Site Acronym	S3A								S3B							
	OTCI vs MTCI				OGVI vs MGVI				OTCI vs MTCI				OGVI vs MGVI			
	n	R2	NRMSD	Bias	n	R2	NRMSD	Bias	n	R2	NRMSD	Bias	n	R2	NRMSD	Bias
AU-Calperum	12	0.45	0.04	0.09	12	0.9	0.08	-0.01	12	0.15	0.05	0.03	12	0.73	0.16	0
AU-Cape-Tribulation	12	0.8	0.04	-0.09	12	0.24	0.04	0.15	12	0.74	0.04	-0.17	12	0.08	0.1	0.16
AU-Cumberland	12	0.57	0.04	-0.05	12	0.55	0.07	0.07	12	0.5	0.04	0.02	12	0.63	0.1	0.08
AU-Great-Western	12	0.97	0.02	0.11	12	0.93	0	0.04	12	0.95	0.02	0.11	12	0.73	0.1	0.02
AU-Robson-Creek	12	0.91	0.03	-0.03	12	0.87	0.07	0.1	12	0.83	0.05	-0.16	12	0.84	0.07	0.12
AU-Rushworth	12	0.84	0.04	0.14	12	0.35	0.08	0.09	12	0.81	0.04	0.02	12	0.39	0.12	0.06
AU-Tumbarumba	12	0.88	0.05	0.31	12	0.62	0.06	0.09	12	0.77	0.04	0.13	12	0.16	0.13	0.01
AU-Warra-Tall	12	0.68	0.06	-0.08	12	0.3	0.21	0.04	9	0.7	0.05	-0.3	9	0.24	0.28	0.01
AU-Watts-Creek	12	0.67	0.05	0.03	12	0.44	0.08	0.09	12	0.72	0.05	-0.02	12	0.23	0.11	0.08
AU-Wombat	12	0.91	0.03	0.11	12	0.34	0.05	0.08	12	0.88	0.03	-0.02	12	0.01	0.08	0.04
BE-Brasschaat	11	0.99	0.03	-0.04	11	0.97	0.08	0.06	10	0.97	0.04	-0.09	10	0.93	0.08	0.02
BE-Vielsalm	11	0.89	0.05	0.06	11	0.98	0.06	0.1	10	0.91	0.04	0.01	10	0.92	0.11	0.12
CA-Mer-Bleue	10	0.97	0.04	0	10	0.97	0.06	0.03	10	0.94	0.05	-0.01	10	0.97	0.08	0.01
CZ-Bili-Kriz	12	0.81	0.05	0.09	12	0.93	0.1	0.07	9	0.91	0.04	-0.1	9	0.82	0.13	0.06
DE-Haininch	10	0.99	0.07	-0.04	10	0.98	0.08	0.05	9	0.97	0.09	-0.04	9	0.97	0.1	0.1
DE-Hones-Holz	10	0.99	0.04	0.1	10	1	0.02	0.05	10	0.97	0.08	-0.11	10	0.94	0.12	0.01
DE-Selhausen	12	0.88	0.09	-0.03	12	0.53	0.18	0.06	12	0.83	0.1	-0.13	12	0.31	0.27	0.02
DE-Tharandt	11	0.97	0.05	-0.02	11	0.97	0.09	0.09	10	0.98	0.04	-0.21	10	0.97	0.09	0.09
FR-Aurade	12	0.83	0.1	0.07	12	0.81	0.19	0.14	11	0.88	0.08	0.03	11	0.86	0.16	0.08
FR-Estrees-Mons	12	0.94	0.07	0.01	12	0.88	0.11	0.06	11	0.87	0.12	0.14	11	0.87	0.11	0.04
FR-Guayaflux	12	0.78	0.03	-0.14	12	0.46	0.07	0.16	12	0.68	0.04	-0.22	12	0.07	0.17	0.19
FR-Hesse	12	0.99	0.04	0.04	12	0.98	0.06	0.06	11	0.96	0.07	0.03	11	0.86	0.17	0.08
FR-Montiers	12	0.99	0.03	-0.13	12	0.99	0.06	0.05	12	0.96	0.08	-0.15	12	0.95	0.13	0.07
FR-Puechabon	12	0.85	0.03	-0.04	12	0.93	0.06	0.09	12	0.89	0.04	0.08	12	0.93	0.06	0.06
IT-Casterporziano2	12	0.95	0.02	-0.13	12	0.88	0.03	0.06	12	0.91	0.04	-0.05	12	0.65	0.05	0.03
IT-Collelongo	12	0.98	0.06	0	12	0.98	0.08	0.02	12	0.94	0.12	0.05	12	0.92	0.16	0.03
IT-Lison	12	0.98	0.03	-0.05	12	0.97	0.07	0.08	12	0.93	0.06	-0.06	12	0.91	0.1	0.08
NE-Loobos	12	0.72	0.07	0.08	12	0.89	0.1	0.05	12	0.61	0.07	0.05	12	0.88	0.1	0.03
UK-Wytham-Woods	12	0.97	0.05	0.07	12	0.96	0.07	0.1	11	0.94	0.07	-0.06	11	0.86	0.16	0.07
US-Bartlett	12	0.98	0.03	-0.03	12	0.98	0.1	0.06	12	0.89	0.08	-0.05	12	0.95	0.12	0.04
US-Central-Plains	12	0.76	0.03	-0.02	12	0.91	0.1	0.01	11	0.74	0.03	-0.03	11	0.8	0.21	0
US-Harvard	12	0.99	0.03	-0.14	12	0.97	0.09	0.04	12	0.97	0.05	-0.24	12	0.93	0.14	0.01
US-Jornada	10	0.77	0.04	0.02	10	0.91	0.2	0.01	8	0.82	0.04	0.07	8	0.35	0.4	0.01
US-Moab-Site	12	0.69	0.03	0.05	12	0.11	0.22	0.01	11	0.88	0.02	0.02	11	0.04	0.43	0.04
US-Mountain-Lake	12	0.99	0.05	-0.21	12	0.99	0.05	0.03	11	0.96	0.07	-0.41	11	1	0.05	0
US-Oak-Rige	12	1	0.03	-0.05	12	0.98	0.07	0.05	12	0.98	0.05	-0.07	12	0.99	0.05	0.05
US-Smithsonian	11	0.98	0.05	-0.16	11	0.99	0.05	0.04	9	0.99	0.06	-0.22	9	0.97	0.09	0.01
US-Steigerwarldt	12	0.95	0.06	-0.02	12	0.99	0.08	0	10	0.95	0.06	-0.06	10	0.99	0.05	0.01
US-Talladega	12	0.98	0.02	-0.13	12	0.98	0.05	0.07	12	0.91	0.05	-0.19	12	0.93	0.1	0.06

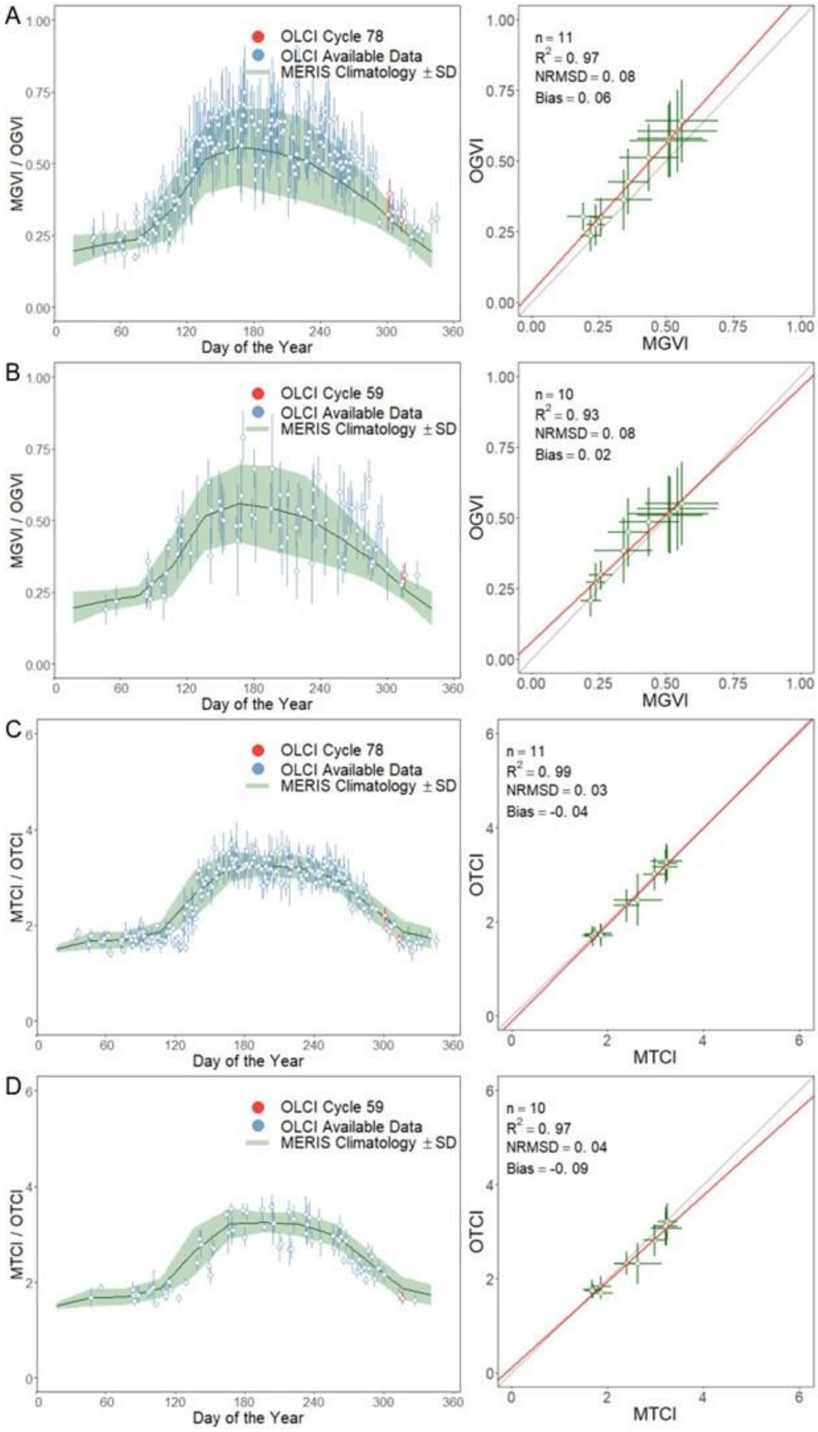

Figure 103: Time-series OGVI and OTCI and corresponding scatterplot of monthly mean for site BE-Brasschaat, Belgium, land cover Needle-leaved, evergreen. A and C represent S3A; B and D represent S3B.

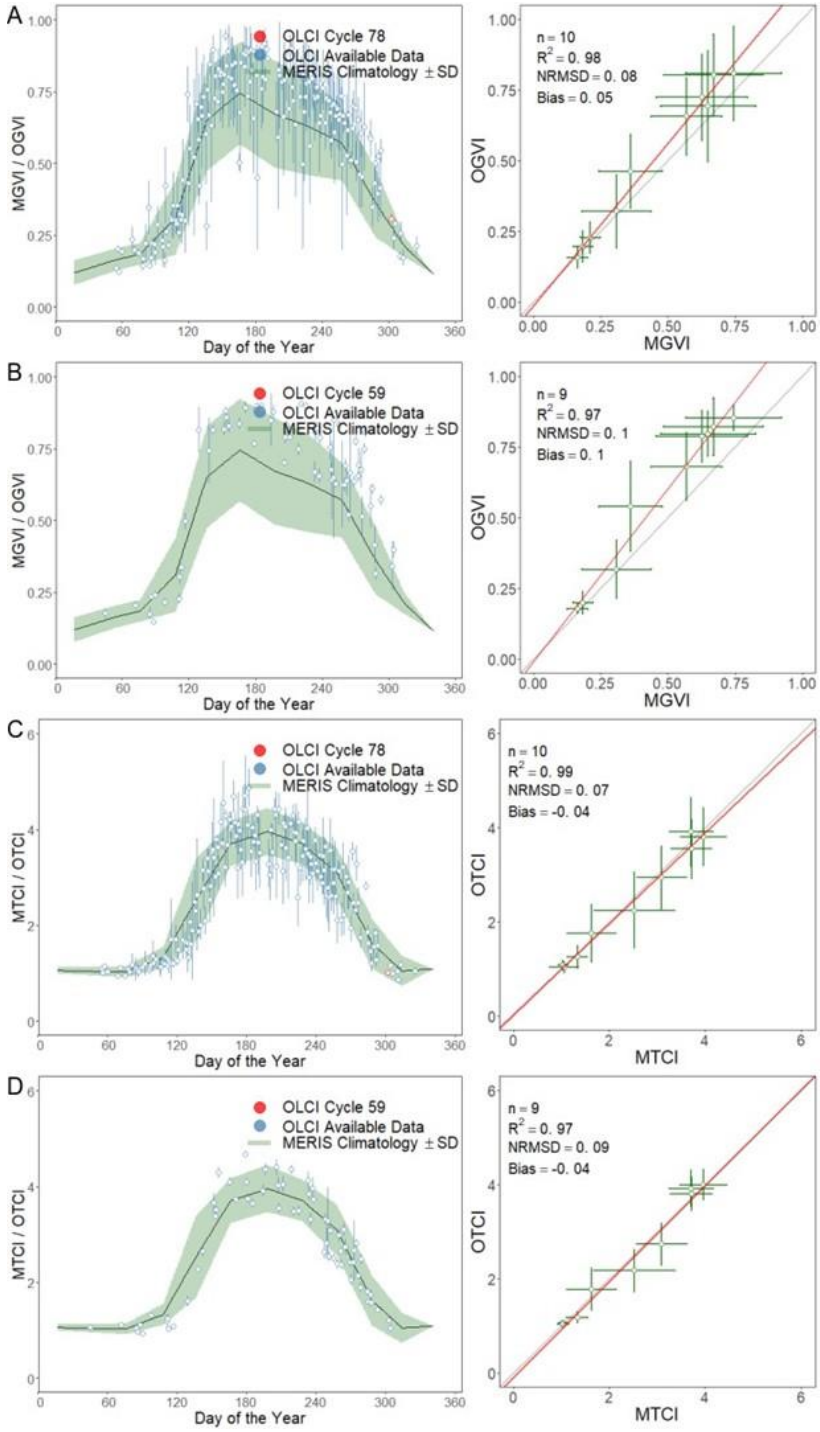

Figure 104: Time-series OGVI and OTCI and corresponding scatterplot of monthly mean for site DE-Haininch, Deutschland, land cover Broadleaved, deciduous, closed. A and C represent S3A; B and D represent S3B.

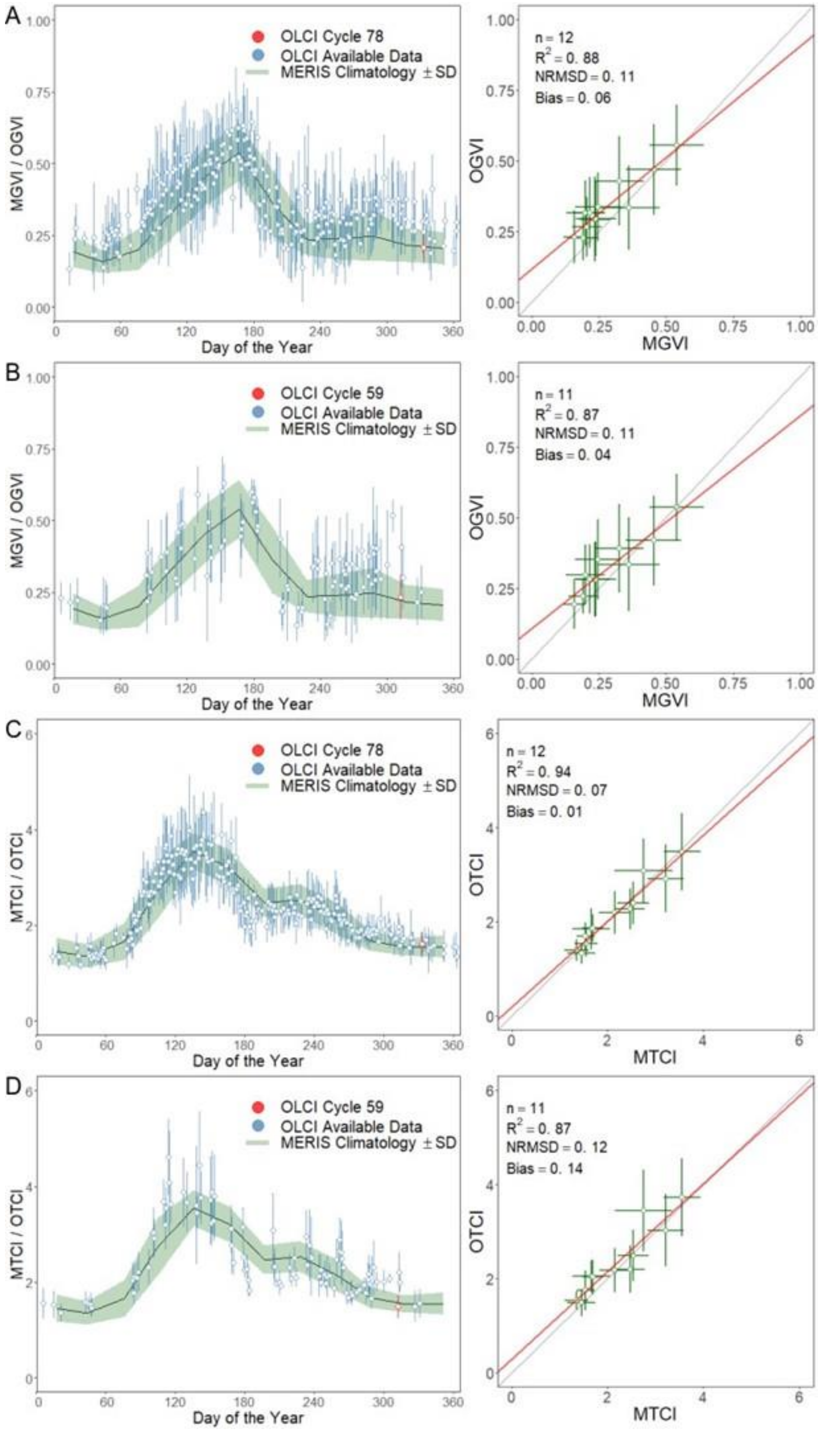

Figure 105: Time-series OGVI and OTCI and corresponding scatterplot of monthly mean for site FR-EstreesMons, France, land cover Cultivated and managed areas. A and C represent S3A; B and D represent S3B.

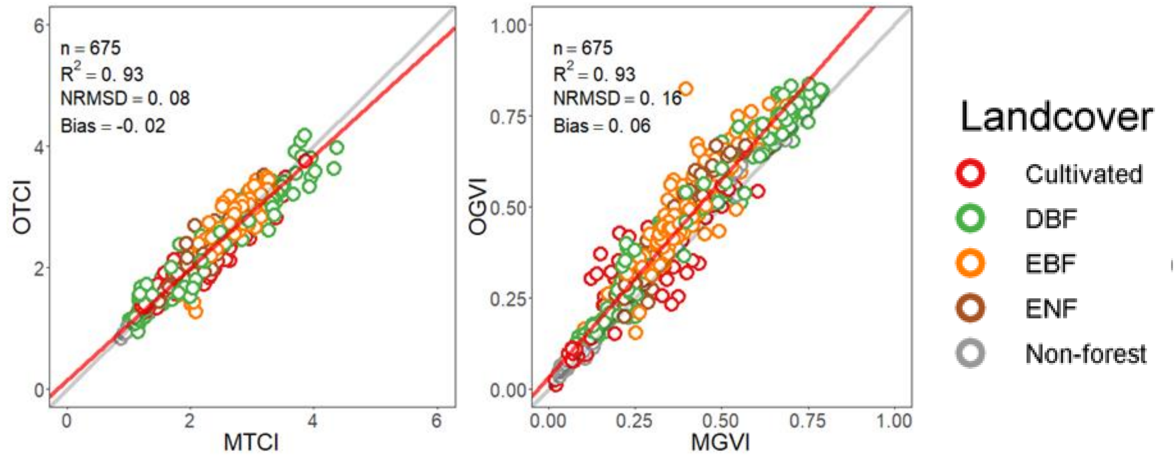

Figure 106: Comparison of OTCI-MTCI (a) and OGVI-MGVI (b). Points in the scatterplot represent the monthly mean of all available S3A and MERIS archive over 42 validation sites. Red and grey lines represent the modelled and 1:1 lines respectively. The scatterplots are updated to include extractions from current S3A cycle.

4.2 [OLCI-L2LRF-CV-410 & OLCI-L2LRF-CV-420] – Cloud Masking & Surface Classification for Land Products

There has been no new result during the cycle. Last figures (reported in OLCI Cyclic Report 074-055) are considered valid.

Routine monitoring activities have been continued.

5 Validation of Integrated Water Vapour over Land & Water

The OLCI L2 IWV processor distinguishes between ocean and land surfaces, and works very differently above the respective surfaces. The algorithm above water shows some serious flaws and is therefore not further investigated. A new version is under development, that will be integrated into an atmospheric branch. However, despite of a small systematic overestimation, the water vapour above land works very well and stable, and it is a good indicator for a system monitoring.
OLCI's IWV above land surface is validated using the following ground truth data:

1. Global GNSS data, with a focus to north America (SUOMI NET, Ware et al. 2000)
2. Microwave radiometer measurements at the *Atmospheric Radiation Measurement* (ARM) *Climate Research Facility* of the US Department of Energy (Turner et al. 2003, Turner et al. 2007).
3. GRUAN radiosonde observations IWV (Immler et al 2010, Bodeker 2015)
4. AERONET (Holben et al 1998), using atmospheric transmission measurements at 0.9µm

All L2 product types have been validated: full resolution and reduced resolution, near real time and non time critical, Ocean Colour (*wrr, wfr*) and Land Colour (*lrr, lfr*). The found results for all product types are identical, as expected, since the used processor is the same. The following quantitative comparisons are hence restricted to *wrr NT* (Ocean Colour Product, reduced resolution, non time critical). Since the ocean colour product and the land colour product provide water vapour above land and water surfaces, the comparison is comprehensive. OLCI A data partly belong to reprocessed data if processed before Nov/2017. The ocean colour products from OLCI A have been taken from Eumetsats rolling archive CODA (Copernicus Online Data Access, https://coda.eumetsat.int/#/home) or reprocessed OLCI A CODAREP (https://codarep.eumetsat.int/#/home) websites. All OLCI B data is from Eumetsats CODA.

5.1 Integrated water vapour above land

5.1.1 Validation of OLCI A IWV using GNSS

576,000 potential matchups within the period of June 2016 to present have been analysed so far. The scenes cover high and low elevations, however, the majority of the used SUOMI-NET ground stations are in North and Central America. Only OLCI measurements are taken for the validation which are above land and are cloud-free in an area of about 10x10 km^2 around the GNSS stations. For the cloud detection, the standard L2 cloud-mask has been applied (including the cloud ambiguous and cloud margin flags). The comparison of OLCI and GNSS shows a very high agreement (Figure 107). The correlation between both quantities is 0.98 The root-mean-squared-difference is 2.1 kg/m^2. The systematic overestimation by OLCI is 12%. The bias corrected *rmsd* is 1.3 kg/m^2. Interesting is the strong seasonal pattern of the bias. It is also partly visible in the systematic overestimation swinging between 7 and 12%. This clearly belongs to the seasonality of water vapour in North Amerika, with lower (better) values during winter. This could be an artefact of the retrieval inherent spectral extrapolation of the surface reflectance from window bands to the absorption band.

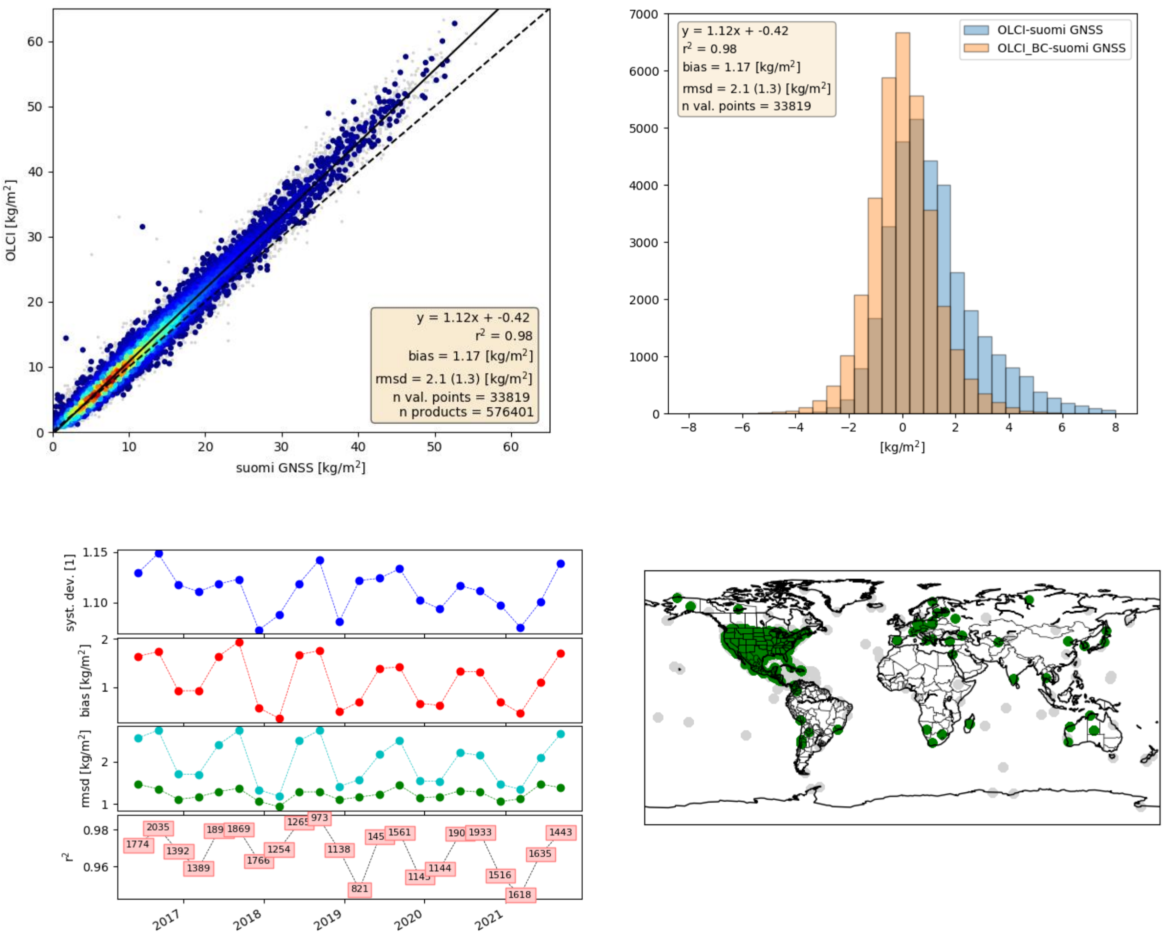

Figure 107: Upper left: Scatter plot of the IWV products, derived from OLCI A above land and from SUOMI NET GNSS measurements. Upper right: Histogram of the difference between OLCI and GNSS (blue: original OLCI, orange: bias corrected OLCI). Lower left: Temporal evolution of different quality measures (from top to bottom: systematic deviation factor, bias, root mean squared difference (with and without bias correction), explained variance (number in boxes are the numbers of matchups)). Lower right: Positions of the GNSS stations (grey: no valid matchup)

5.1.2 Validation of OLCI A IWV using passive microwave radiometer at ARM sites

Microwave radiometer measurements at the *Atmospheric Radiation Measurement* (ARM) *Climate Research Facility* of the US Department of Energy provides the ground truth with the highest accuracy (0.6 kg/m^2). Currently 3 ARM sites are operated continuously, only the SGP (southern great planes) site provided cloud free measurements. 3700 potential matchups within the period of June 2016 to November 2021 have been analysed yet. Only OLCI measurements are taken for the validation which are above land and are cloud-free in an area of about 10x10 km^2 around SGP.

Apparently the dissemination of one file type (*sgpmwrret1liljclouC1.s1*) has been discontinued. Instead we used at beginning of 2001 a precursor product (*sgpmwrret1liljclouC1.c1*), that already contains all necessary data, but not stringently filtered for glitches (e.g. rain on MWR window or thermal anomalies). Unfortunately, this has been discontinued in 2021 too. So, we switched to a different product: *sgpmwrlosC1.b1*. The *mwrret* (*microwave physical retrieval*) and *mwrlos* (*microwave line of sight retrieval*) are based on the same measurements and physical properties of the atmosphere. *Mwrret* uses an variational approach with a full radiative transfer optimization, whereas *mwrlos* is based on seasonally adapted regression parameter. Both retrievals provide ground truth with a high precision (0.6 kg/m^2 and 0.8 kg/m^2). To guarantee temporal stability we reprocessed the full time series of OLCI A and B.

For the cloud detection, the standard L2 cloud-mask has been applied (including the cloud ambiguous and cloud margin flags), resulting in 206 valid matchups. The comparison shows a very high agreement (Figure 108Figure 107). The correlation between both quantities is 0.99. The root-mean-squared-difference is 1.4 kg/m^2. The systematic overestimation by OLCI is 9%. The bias corrected *rmsd* is 0.9 kg/m^2, close to the uncertainty of the MWR. The investigation of the temporal evolution shows the same seasonal pattern as the GNSS comparisons, again belonging to the same seasonality of water vapour in North Amerika.

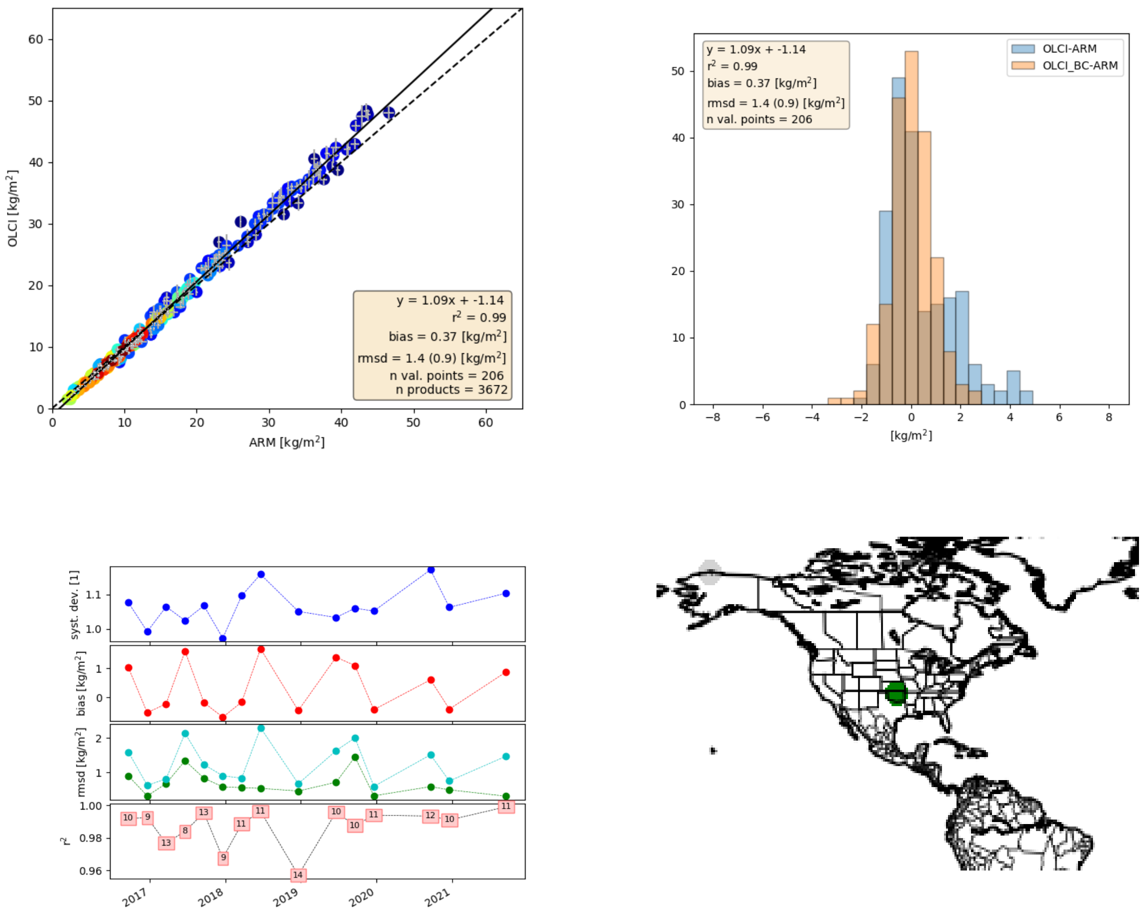

Figure 108: Upper left: Scatter plot of the IWV products, derived from OLCI A above land and from AMR MWR. Upper right: Histogram of the difference between OLCI and ARM (blue: original OLCI, orange: bias corrected OLCI). Lower left: Temporal evolution of different quality measures (from top to bottom: systematic deviation factor, bias, root mean squared difference (with and without bias correction), explained variance (number in boxes are the numbers of matchups)). Lower right: Position of ARM SGP.

5.1.3 Validation of OLCI A IWV using GRUAN radiosonde observations

Radiosonde observations of temperature, humidity and pressure allow a direct integration of water vapour. The emphasis of GRUAN is to provide long-term, highly accurate measurements of the atmospheric profile. This is achieved by a very rigid quality control and uncertainty quantification. From the 3300 potential matchups within the period of June 2016 to January 2021, only OLCI measurements are taken for the validation which are above land and are cloud-free in an area of about 10x10 km^2 around the radiosonde launch place. For the cloud detection, the standard L2 cloud-mask has been applied (including the cloud ambiguous and cloud margin flags). Eventually only 39 valid matchups could be used. This number is less than the number of valid matchups for the ARM site, since radiosondes launches are rare. That is why the time constraints have been relaxed to 6h. Still, the comparison shows a very high agreement (Figure 109). The correlation between both quantities is 0.99. The root-mean-squared-difference is 2.4 kg/m^2. The systematic overestimation by OLCI is 12%. The bias corrected *rmsd* is 1.3 kg/m^2. The number of valid matchups is currently too low to investigate a temporal evolution.

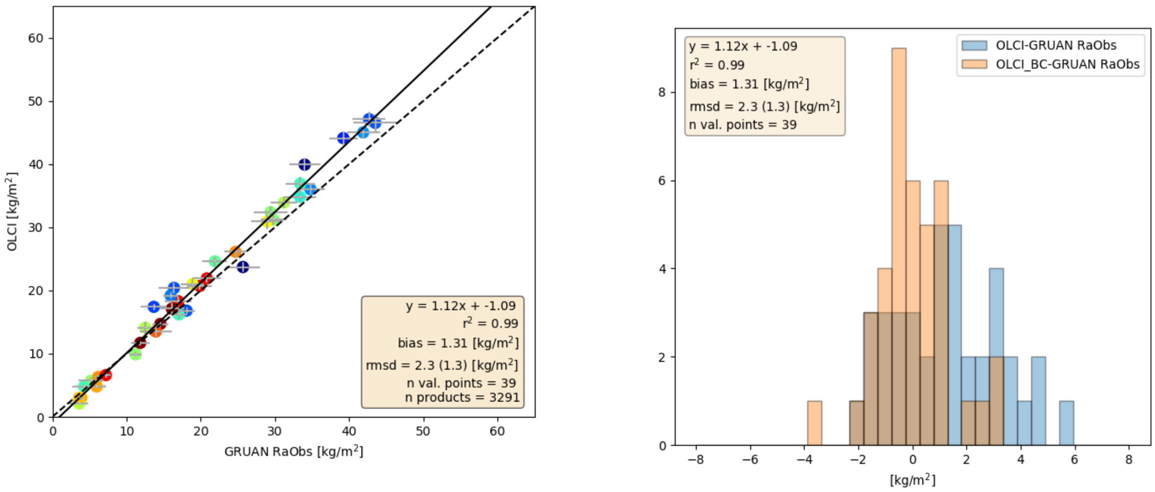

Figure 109: Left: Scatter plot of the IWV products, derived from OLCI A above land and from GRUAN radiosonde measurements. Right: Histogram of the difference between OLCI and GRUAN (blue: original OLCI, orange: bias corrected OLCI).

5.1.4 Validation of OLCI A IWV using AERONET observations

AERONET observations, regardless not primary made for water vapour, allow the direct estimation of the total column of water vapour by measuring the extinction of the direct solar irradiance at 900 nm. The used operational algorithm is quite simple and eventually relies on a logarithmic fit (incl. quadratic corrections). We are using AERONET for the IWV comparison, since AERONET data are better globally distributed, than ARM and SUOMINET, and are more frequent than GRUAN. In contrast to earlier investigations we use AERONET V3 level 1.5. It is not stringently quality controlled, but the retrieval algorithm is exactly the same as for level 2 and it is published without delay. This allows much more matchups with data from the 1 yr. rolling archive CODA.

Only OLCI measurements are used for the validation which are cloud-free (according to the standard cloud flags: *cloud, cloud margin and cloud ambiguous*) in an area of about 10x10 km^2 around the AERONET acquisition. From the 208000 potential matchups within the period of June 2016 to November 2021, 38500 valid matchups could be used. (Figure 110). The correlation between both quantities is 0.96. The root-mean-squared-difference is 3.7 kg/m^2. The systematic overestimation by OLCI is 19%. The bias corrected *rmsd* is 1.8 kg/m^2. The systematic deviation between OLCI and AERONET of 19% is significantly larger than the one found for GNSS, ARM and GRUAN (~10%). We think that this stems from a dry bias of AERONET and accordingly deficits in the operational algorithm, but we have not investigated it deeper.

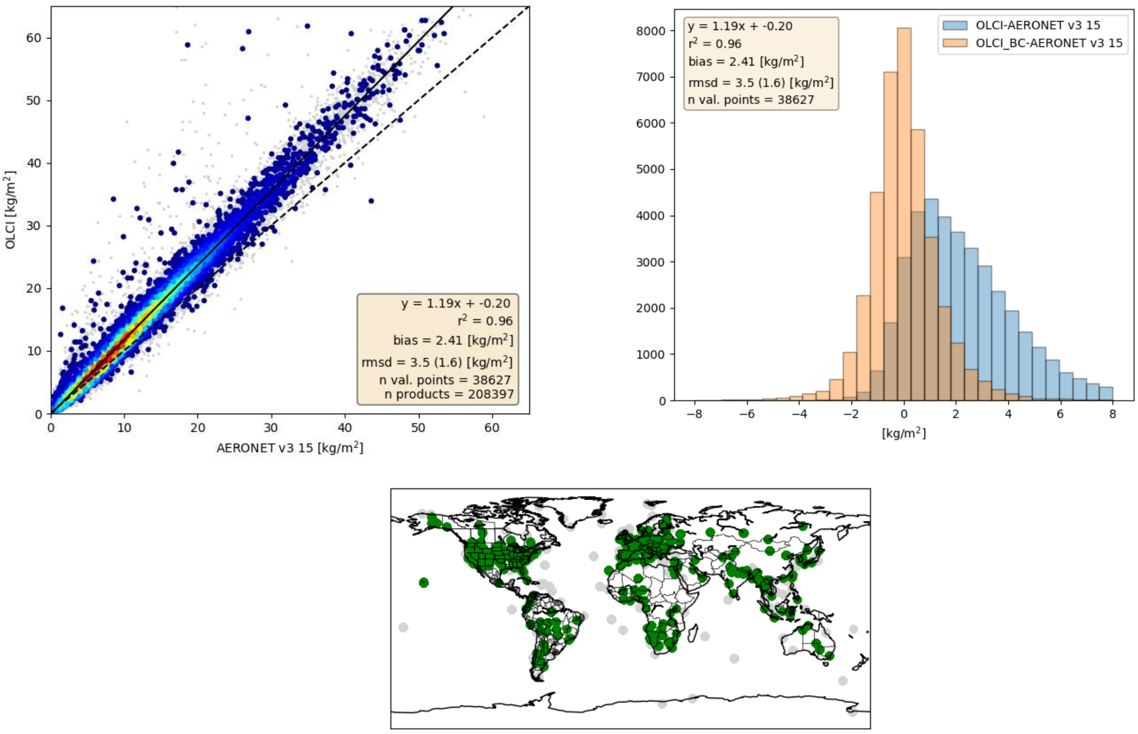

Figure 110: Upper left: Scatter plot of the IWV products, derived from OLCI A above land and from AERONET. Upper right: Histogram of the difference between OLCI and AERONET (blue: original OLCI, orange: bias corrected OLCI). Lower: Positions of the used AERONET stations (grey: no valid matchup).

5.1.5 Validation of OLCI B IWV

Within the period of June 2018 to present, about 100000 scenes have been analysed. 17800 of them are valid for SUOMI-NET CONUS ground stations in North and Central America, 97 for ARM MWR and 20500 for AERONET.

As for OLCI A, only measurements are taken for the validation which are above land and are cloud-free in an area of about 10x10 km^2 around the corresponding stations. For the cloud detection, the standard L2 cloud-mask has been applied (including the cloud ambiguous and cloud margin flags). The comparison of OLCI B shows almost identical results as for OLCI A (Figure 111).

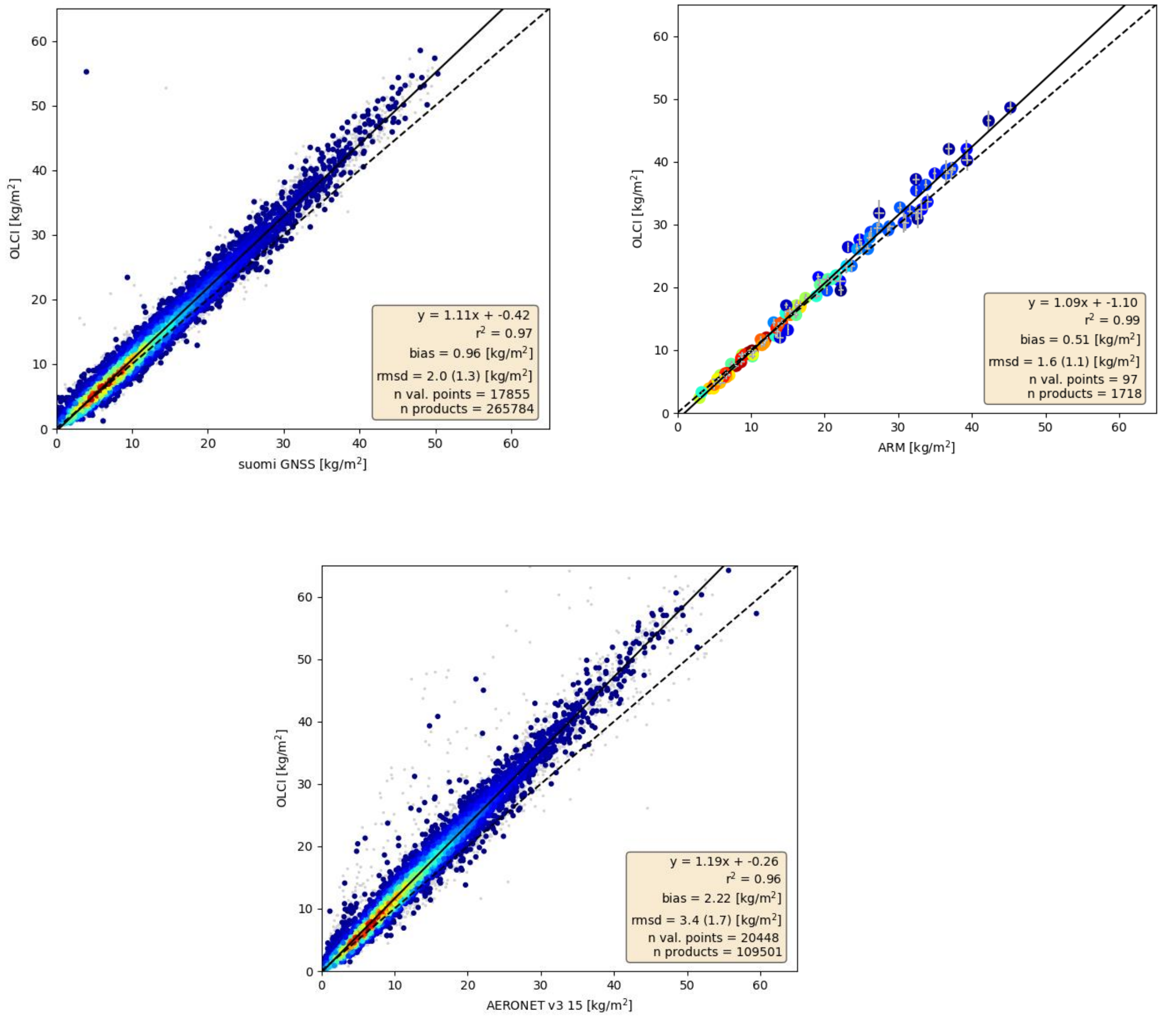

Figure 111: Scatter plot of the IWV products, derived from OLCI B above land and from SUOMI NET GNSS measurements (upper left), from ARM MWR (upper right) and AERONET (lower)

5.2 Integrated water vapour above water

5.2.1 Quantitative validation using GNSS

OLCIs IWV above water surfaces has been quantitatively validated via global GNSS measurements too, however with few additional assumptions:

- Since the GNSS stations are usually not directly above water, the closest water pixel (within 1km) is used for the satellite measurement.
- No height correction has been applied to account for the potentially elevated GNSS station.

For OLCI-A, 70 matchups remain after filtering (Figure 112). They show a large bias 10 kg/m^2 and a large scatter (>6 kg/m^2). For OLCI-B the number of valid matchups is smaller (32), but all indications point to similar systematic deviations and retrieval noise. This is in accordance with the visual inspection.

.

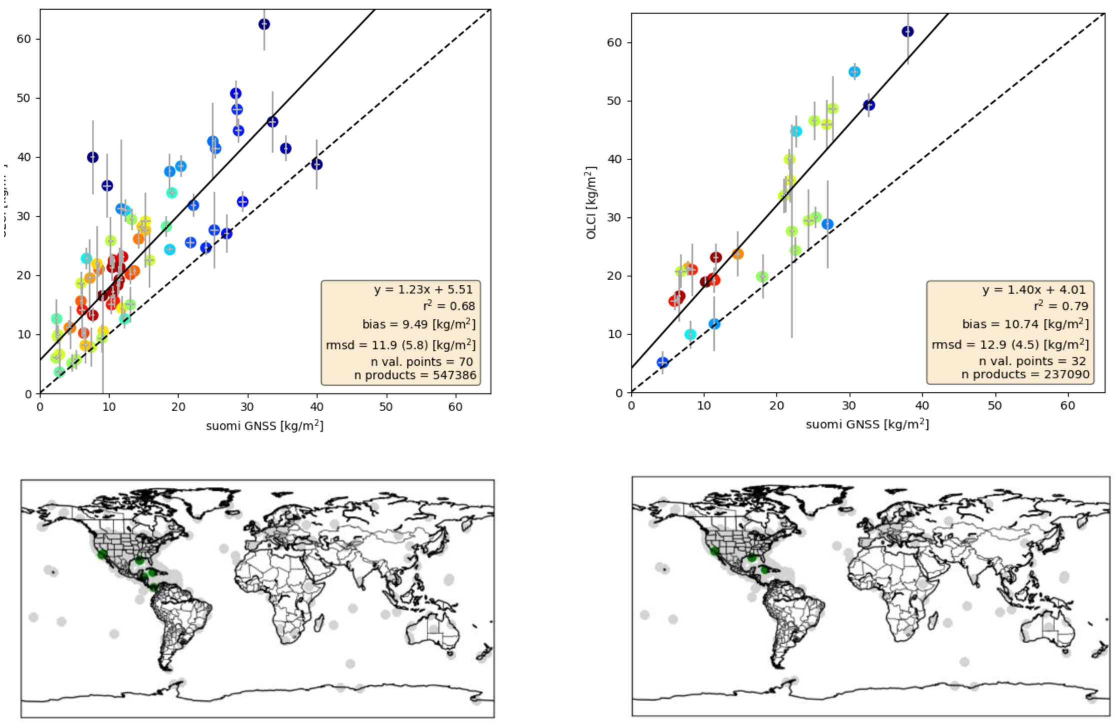

Figure 112: Upper: Scatter plot of the IWV products, derived from OLCI (A left, B right) above ocean and from SUOMI NET GNSS measurements. Lower: Positions of the GNSS (A: left, B: right).

5.2.2 Validation by AERONET IWV Retrievals – Ocean

OLCIs IWV above water surfaces has been quantitatively validated via global AERONET-OC measurements. All filters are as for land matchups. The remaining 2300 (OLCI-A) and 1200 (OLCI-B) matchups show a large bias of about 9 kg/m^2, a large scatter (>6 kg/m^2) and a systematic overestimation of about 20% (Figure 113). This is in accordance with the visual inspection and with the GNNS matchups (Figure 112) over oceans.

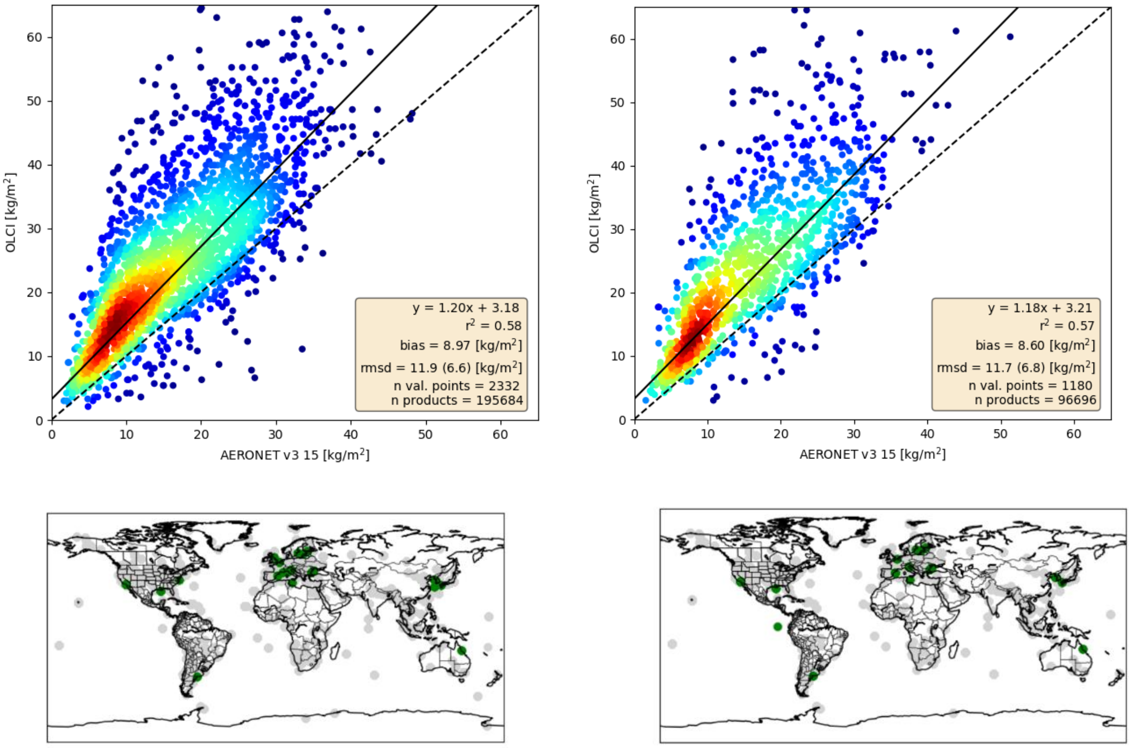

Figure 113: Upper: Scatter plot of the IWV products, derived from OLCI (A left, B right) above ocean and from Aeronet-OC v.3 L1.5 measurements. Lower: Positions of the used Aeronet match ups (A: left, B: right).

5.3 Summary

The validation exercise of the OLCI A IWV over land product using 4 different sources of ground truth showed consistently, that the product is of high quality (bias corrected root mean squared distance of down to 1.5 -0.8 kg/m^2). However, there is a systematic overestimation of 9% to 13%. An equivalent validation of OLCI B shows the same results, no systematic differences between OLCI a and B have been found. The validation with Suominet shows seasonal patterns of the overestimation with better values during winter seasons.

Retrievals above ocean show an overestimation in transition zones between glint and off glint. This is a clear deficit of the description of the scattering-absorption interaction. Further the IWV has a large wet bias over ocean.

5.4 References

- Bodeker, G. E., Bojinski, S., Cimini, D., Dirksen, R. J., Haeffelin, M., Hannigan, J. W., Hurst, D. F., Leblanc, T., Madonna, F., Maturilli, M., Mikalsen, A. C., Philipona, R., Reale, T., Seidel, D. J., Tan, D. G. H., Thorne, P. W., Vömel, H., and Wang, J.: Reference upper-air observations for climate: From concept to reality, B. Am. Meteorol. Soc., doi:10.1175/BAMS-D-14-00072.1, 2015.

- Holben, B. N., et al., AERONET—A federated instrument network and data archive for aerosol characterization, Remote Sens. Environ.,66, 1–16, 1998.)

- Immler, F. J., Dykema, J., Gardiner, T., Whiteman, D. N., Thorne, P.W., and Vömel, H.: Reference Quality Upper-Air Measurements: guidance for developing GRUAN data products, Atmos. Meas.Tech., 2, 1217–1231, doi:10.5194/amt-3-1217-2010, 2010.

- Pérez-Ramírez, D., D. N. Whiteman, A. Smirnov, H. Lyamani, B. N. Holben, R. Pinker, M. Andrade, and L. Alados- Arboledas (2014), Evaluation of AERONET precipitable water vapor versus microwave radiometry, GPS, and radiosondes at ARM sites, J. Geophys. Res. Atmos., 119, 9596–9613, doi:10.1002/2014JD021730

- Smirnov, A., Holben, B.N., Slutsker, I., Giles, D.M., McClain, C.R.,Eck, T.F., Sakerin, S.M., Macke, A., Croot, P., Zibordi, G., Quinn, P.K., Sciare, J., Kinne, S., Harvey, M., Smyth, T.J., Piketh, S.,Zielinski, T., Proshutinsky, A., Goes, J.I., Nelson, N.B., Larouche,P., Radionov, V.F., Goloub, P., Krishna Moorthy, K., Matarrese, R.,Robertson, E.J., Jourdin, F., 2009. Maritime aerosol network as acomponent of aerosol robotic network. J. Geophys. Res. 114, 1—10, http://dx.doi.org/10.1029/2008JD011257.

- Ware, R. H., D. W. Fulker, S. A. Stein, D. N. Anderson, S. K. Avery, R. D. Clark, K. K. Droegemeier, J. P. Kuettner, J. B. Minster, and S. Sorooshian (2000), SuomiNet: A real-time national GPS network for atmospheric research and education, Bull. Am. Meteorol. Soc., 81(4), 677–694.

- Zibordi G., B.Holben, I.Slutsker, D.Giles, D.D'Alimonte, F.Mélin, J.-F. Berthon, D. Vandemark, H.Feng, G.Schuster, B.Fabbri, S.Kaitala, J.Seppälä. AERONET-OC: a network for the validation of Ocean Color primary radiometric products. Journal of Atmospheric and Oceanic Technology, 26, 1634-1651, 2009.

6 Level 2 SYN products validation

There has been no new result during the cycle. Most recent performance figures can be found in the S3MPC OPT Annual Performance Report - Year 2021 (S3MPC.ACR.APR.009, issue 1.0, 08/12/2021), available on-line at:

https://sentinels.copernicus.eu/web/sentinel/user-guides/sentinel-3-olci/document-library.

https://sentinels.copernicus.eu/documents/247904/4744994/S3MPC.ACR.APR.009%20-%20i1r0%20-%20OPT%20Annual%20Performance%20Report%20-%20Year%202021.pdf/c6f22e03-7f9e-b3f2-6f7c-e83d0c53f954

7 Events

For OLCI-A, three Radiometric Calibration sequences have been acquired during the reported period:

- S01 sequence (diffuser 1) on 11/01/2022 12:22 to 12:24 (absolute orbit 30739)
- S01 sequence (diffuser 1) on 27/01/2022 00:19 to 00:21 (absolute orbit 30960)
- S05 sequence (diffuser 2) on 27/01/2022 02:00 to 02:02 (absolute orbit 30961)

For OLCI-B, three Radiometric Calibration sequences have been acquired during the reported period:

- S01 sequence (diffuser 1) on 12/01/2022 07:54 to 07:56 (absolute orbit 18908)
- S01 sequence (diffuser 1) on 28/01/2022 11:00 to 11:08 (absolute orbit 19587)
- S05 sequence (diffuser 2) on 28/01/2022 12:41 to 12:43 (absolute orbit 19588)

As there was no Cyclic Performance Report delivered since Cyclic Performance Report #78/#59 (OLCI-A/OLCI-B), we report hereafter the Radiometric calibration sequences that have been acquired between the release of the last CPR and the beginning of the current reporting period. These acquisitions are taken into account in the current Data Quality report:

For OLCI-A, four Radiometric Calibration sequences have been acquired since the last CPR:

- S01 sequence (diffuser 1) on 23/11/2021 06:48 to 06:50 (absolute orbit 30037)
- S05 sequence (diffuser 2) on 23/11/2021 08:29 to 08:31 (absolute orbit 30038)
- S01 sequence (diffuser 1) on 11/12/2021 00:39 to 00:41 (absolute orbit 30290)
- S01 sequence (diffuser 1) on 26/12/2021 04:12 to 04:14 (absolute orbit 30056)

For OLCI-B, two Radiometric Calibration sequences have been acquired since the last CPR:

- S01 sequence (diffuser 1) on 11/12/2021 20:11 to 20:13 (absolute orbit 18908)
- S01 sequence (diffuser 1) on 26/12/2021 22:04 to 22:06 (absolute orbit 19123)

8 Appendix A

Other reports related to the Optical mission are:

- Data Quality Report – Sentinel-3 SLSTR, January 2022, (ref. OMPC.RAL.DQR.04.01-2022)

All Data Quality Reports, as well as past years Cyclic Performance Reports and Annual Reports, are available on dedicated pages in Sentinel Online website, at:

- https://sentinel.esa.int/web/sentinel/technical-guides/sentinel-3-olci/data-quality-reports
- https://sentinels.copernicus.eu/web/sentinel/technical-guides/sentinel-3-slstr/data-quality-reports
- OPT Annual Performance Report Year 02021 (PDF document)

End of document